EXPERIMENTAL INVESTIGATION OF THE INTERFACIAL FRACTURE TOUGHNESS IN ORGANIC PHOTOVOLTAICS

A Dissertation
Presented to
The Academic Faculty

by

Yongjin Kim

In Partial Fulfillment
of the Requirements for the Degree
Doctor of Philosophy in the
School of Mechanical Engineering

Georgia Institute of Technology
May 2013

EXPERIMENTAL INVESTIGATION OF THE INTERFACIAL FRACTURE TOUGHNESS IN ORGANIC PHOTOVOLTAICS

Approved by:

Dr. Samuel Graham, Advisor
George W. Woodruff School
of Mechanical Engineering
Georgia Institute of Technology

Dr. Seth Marder
School of Chemistry and Biochemistry
Georgia Institute of Technology

Dr. Suresh K. Sitaraman
George W. Woodruff School
of Mechanical Engineering
Georgia Institute of Technology

Dr. Dennis W. Hess
School of Chemical &
Biomolecular Engineering
Georgia Institute of Technology

Dr. Ting Zhu
George W. Woodruff School
of Mechanical Engineering
Georgia Institute of Technology

Date Approved: March 22, 2013

ACKNOWLEDGEMENTS

First of all, I would like to acknowledge my Lord who gave me love and wisdom during my time at Georgia Tech. It was a precious time to meet him and to communicate with him while accomplishing everything that I have done to finish my Ph.D. studies. Without God's unmerited grace, I would never have been able complete my work and move to the next stage. Thus, I specially give thanks to my Lord for everything that he has done for me and my family during my Ph.D. studies and will look forward to having his next plans for my life.

I want to thank my family for their support, love, and prayers during my Ph.D. studies. I would like to acknowledge my wife, Hana Kim, for her sacrifice and support. While pursuing my doctorate degree, we had two children (Dawul Kim and Dasol Kim) who brought a new dimension to our lives. Without my wife's support, I cannot imagine how I could have dealt with the difficulties of a new culture and life in the U.S.A. Thus, I want to give her my special thanks and want to say that the work was not completed only by me, but we finished it together. I also want to acknowledge my parents (Youngsik Kim and Bongnam Kim) and my parents-in-law (Taejoon Kim and Namhee Lee) for their endless love that makes who I am. I am also thankful to my aunt (Kyungsuk Seo), big brother (Yongjoon Kim), sister-in-law (Hun Cho), sister (Youngsin Kim), little nephew (Khanghee Cho), my little niece (Ciyul Kim), sister-in-law (Dana Kim), and brother-in-law (Myungsung Kim) for their untiring support and love. I also want to acknowledge my grandmother (Jungsoon Choi) who passed away in December 2012. However, your special love is still in my heart now and I will remember it forever.

I especially acknowledge Prof. Samuel Graham for giving me a chance to pursue a Ph.D. degree at Georgia Tech in his research group. I really appreciate his open mind for discussions and constructive suggestions that always motivated me to improve myself. During my time at Georgia Tech., I came to respect him with many reasons. He did not only give me research tips, but he also showed me how to communicate with other people and also gave me many other aspects that made me view him as my role model. I feel really lucky to have him as my Ph.D. advisor. I can never express how much I am thankful to him and how much I respect him. In the future, I wish I hope that I can influence other people in the way he influenced me.

I would also like to thank all of my committee members, Prof. Ting Zhu, Prof. Seth Marder, Prof. Suresh Sitaraman, and Prof. Dennis W. Hess for their advice and participation in the review and evaluation of this work.

I acknowledge Prof. Bernard Kippelen for giving me a chance to do Ca testing of my barrier films and for fabricating many OPV devices in support of this research. In particular, I am thankful to Jaewon Shim, Dr. Dokyung Hwang, Dr. Canek Hernandez, and Dr. Yinhua Zhou for their efforts in fabricating samples and taking time to discuss various research topics with me that helped me through this research project.

I want to thank all past and current group members of the Electronics Manufacturing and Reliability Laboratory of which I am a member, who gave me great support. These members include Sukwon Choi, Adam Christensen, Thomas Beechem, Roderick Jackson, Minseok Ha, Mark Gleva, Prem Nagarathnam, Steven Walker, Fernando Reiter, Hyungchul Kim, Haidong Kim, Parisa Pour Shahid Saeed Abadi, Fatma Nazli Donmezer, William James, Yishak Habtemichael, Anne Mallow, Shweta Natarajan,

and David Samet. Especially, I want to say “thank” to Dr. Anuradha Bulusu for her time with advice on various problems that I have faced and her support for my Ph.D. studies.

For my friends in Atlanta, I want to thank to Dr. Yoonjo Kim for his unlimited support that always motivated me. I was really happy to have him for support during my struggles during my Ph.D. studies. I also want to acknowledge my friends from New Church of Atlanta: Taewoo Kim, Sean Park, Teckhan Yoon, Joonghwan Lee, Jaemin Shin, David Jung, Taejoon Lee, Jinho Park, and Taehoon Yeo. I also thank Pastor Bill Sim for his passion and advices that always helped me to find direction while I have been trying to find my vision under God’s authority during my Ph.D. studies.

I also wish to thank other fellows at Georgia Tech: Keunhan Park, Sungchul Joo, Sangil Lee, Myungsub Kim, Chango Lee, Sukhan Kim, Sunghoon Chong, Myungryul Yoon, Junryul Lim, Sungbum Kang, Jinsung Hong, Dukjoon Kim, Namin Jung, Hongchul Son, Sangin Park, Jungwhon Kim, Sukbum Kim, Jane Kang, and Songkil Kim.

I acknowledge financial support from the NSF Science and Technology Center Materials and Devices for Information Technology Research (CMDITR).

TABLE OF CONTENTS

LIST OF TABLES

LIST OF FIGURES

LIST OF SYMBOLS AND ABBREVIATIONS

a	Crack length
ALD	Atomic layer deposition
AFM	Atomic force microscopy
b	Beam width
BCB	Benzochclobuene
BHJ	Bulk heterojunction
Ca	Calcium
C_s	Surface Concentration
D	Diffusion coefficient
DCB	Double cantilever beam
E	Total system energy
E	Young's modulus
E_b	Binding energy
E_k	Kinetic energy of individual electrons
FF	Fill factor
FPB	Four points bending
G	Conductance
G_c	Interfacial fracture toughness
G_o	Near-tip work of fracture
G_{th}	Threshold energy release rate
G_{zone}	Energy dissipation near the crack tip
h	Half thickness of beam
HOMO	Highest occupied molecular orbital

Hv	Energy of X-ray photons
IFFF	Interfacial shear strength
IM	Interface modification
I_c	Second moment of area of the lower beam beneath the crack
I_o	Second moment of area
ITO	Indium tin oxide
I-V	Current-Voltage
J_{sc}	Short circuit current density
K	Stress intensity factor
L	Distance between inner and outer pins in FPB tests
l	Ca length
LEFM	Linear elastic fracture mechanics
LUMO	Lowest unoccupied molecular orbital
M	Bending moment
M	Molar mass
MCBPA	4-Methoxycarbonylbutyl phosphonic acid
OPV	Organic photovoltaic
PA	Phosphonic acid
PAE	Poly(arylene) ether
PBDTTT-C	Poly((4,8-bis-(2-ethylhexyloxy)-benzo(1,2-b:4,5-b')dithiophene)-2,6-diyl-alt(4-(2-ethylhexanoyl)-thieno(3,4-b)thiophene)-2,6-diyl)
P_c	Critical load
PCBM	Phenyl C61-butyric acid methylester
PCE	Power conversion efficiency
PECVD	Plasma enhanced chemical vapor deposition
PEN	Polyethylene naphthalate

PEIE	Polyethylenimine
PEDOT:PSS	Poly(3,4-ethylenedioxythiophene poly(styrenesulfonate))
PET	Polyethylene terephthalate
PFBPA	Pentafluorobenzyl phosphonic acid
P3HT	Poly3-hexylthiophene
P_{max}	Maximum power density
PMMA	Polymethyl methacrylate
PPE	Plasma polymerized polyethylene
ODPA	Octadecyl phosphonic acid
OFFET	Organic Field Effect Transistor
OTR	Oxygen transmission rate
R_q	Surface roughness
r	Radial distance at the crack tip
r_c	Plastic zone size by Dugdale approach
RH	Relative humidity
r_p	Plastic zone size by Irwin approach
SEM	Scanning electron microscopy
T	Temperature
TCOs	Transparent conductive oxides
TEM	Transmission electron microscopy
TMA	Trimethylaluminum
TOF-SIMS	Time-of-flight secondary ion mass spectrometry
U_o	Strain energy per unit area
V_{oc}	Open circuit voltage
w	Ca width

W_s	Work needed to create new surfaces
WVTR	Water vapor transmission rate
XPS	X-ray photoelectron scpectroscopy
γ	Interfacial tension
δ	Resistivity
η	Power conversion efficiency
θ	Contact angle
ν	Poison's ratio
Π	Potential energy
ρ	Density
σ_{ij}	Stress tensor
σ_{ys}	Yield strength
ψ	Phase angle
ψ_∞	Far-field applied phase angle
I	Tensile opening fracture
II	Sliding fracture
III	Tearing fracture
p	Polar component
d	Dispersive component

SUMMARY

The development of organic photovoltaics (OPVs) has attracted a lot of attention due to their potential to create a low cost flexible solar cell platform. In general, an OPV is comprised of a number of layers of thin films that include the electrodes, active layers and barrier films. Thus, with all of the interfaces within OPV devices, the potential for failure exists in numerous locations if adhesion at the interface between layers is inherently low or if a loss of adhesion due to device aging is encountered. To date, few studies have focused on the basic properties of adhesion in organic photovoltaics and its implications on device reliability. In this dissertation, we investigated the adhesion between interfaces for a model multilayer barrier film (SiN_x/PMMA) used to encapsulate OPVs. The barrier films were manufactured using plasma enhanced chemical vapor deposition (PECVD) and the interfacial fracture toughness (G_c, J/m^2) between the SiN_x and PMMA were quantified. The fundamentals of the adhesion at these interfaces and methods to increase the adhesion were investigated. In addition, we investigated the adhesive/cohesive behavior of inverted OPVs with different electrode materials and interface treatments. Inverted OPVs were fabricated incorporating different interface modification techniques to understand their impact on adhesion determined through the interfacial fracture toughness (G_c, J/m^2). Overall, the goal of this study is to quantify the adhesion at typical interfaces used in inverted OPVs and barrier films, to understand methods that influence the adhesion, and to determine methods to improve the adhesion for the long term mechanical reliability of OPV devices.

CHAPTER 1

INTRODUCTION AND MOTIVATION

1.1. Background

Organic electronic devices such as organic light emitting devices (OLEDs), photovoltaics (OPVs), organic field effect transistors (OFETs), and flexible electrochromics are targeted for many promising applications due to their wide range of tunable properties, multi-functional characteristics, intrinsic mechanical flexibility, and amenability to wide-area manufacturing process [1-3], as shown in Fig. 1.1. Large-area manufacturing, specifically roll-to-roll processing, has the potential to lower manufacturing costs and thus the costs of devices [4-6]. However, unlike semiconductor devices that are more environmentally tolerant like Si-based electronics, organic devices are highly susceptible to degradation from exposure to water vapor and oxygen [7-10]. In addition they also have potential mechanical reliability issues due to their multilayer structure consisting of nanoscale thin films that are generally brittle and may crack under flexural deformation [11, 12]. While these issues are general across many organic electronic device platforms, this study focuses on the mechanical reliability OPV devices. While the results will depend on the specific device structures found in this work, the analysis techniques used in this work can be extended to other organic electronic devices which have also received little attention in terms of understanding their mechanical reliability.

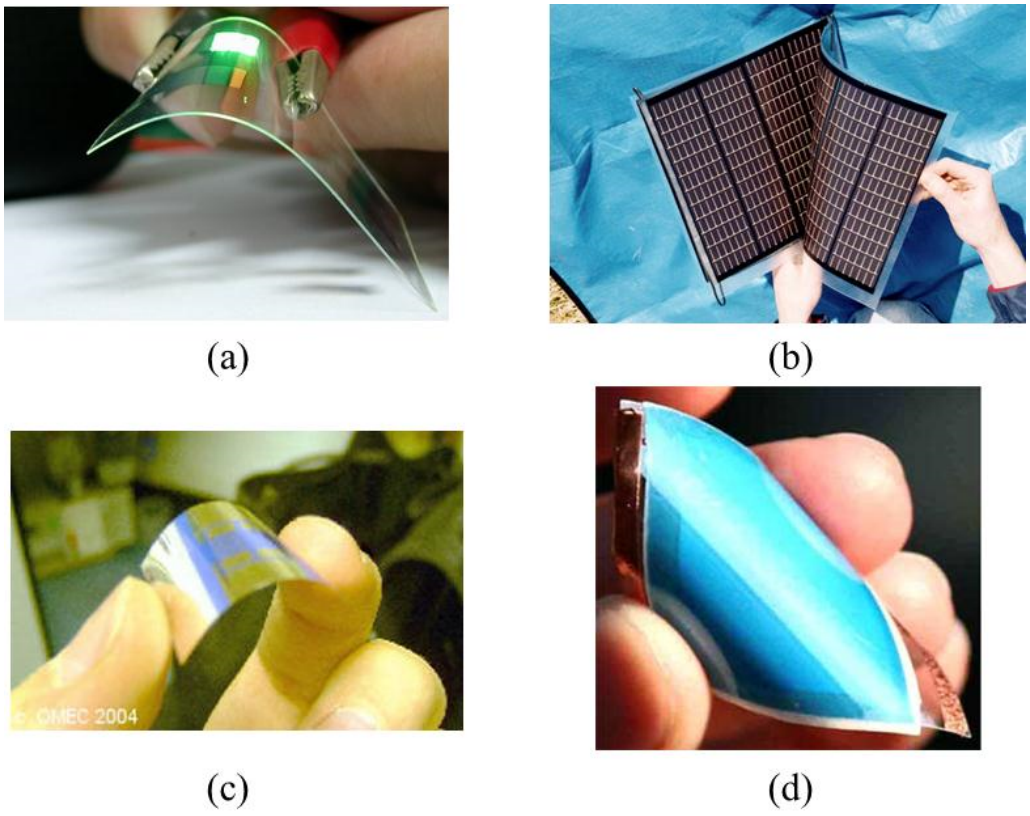

Figure 1.1. (a) Demonstration of flexible OLED device (http://en.wikipedia.org/wiki/File:OLED_EarlyProduct.JPG), (b) flexible OPV device (http://www.solar-green-wind.com/archives/tag/organic-photovoltaics), (c) flexible OFETs (http://www.omec.org.uk/), and (d) flexible electrochromics (http://www.nanowerk.com/spotlight/spotid=572.php).

Since 2001, the efficiency (η) of organic solar cells has increased from 3% to 12.1% [13] as summarized in Fig. 1.2 and the recently reported results by Heliatek (www.heliatek.com). With such trends in the power conversion efficiency (PCE) of OPVs, the potential for low cost using a roll-to-roll processing, their flexibility, and semi-transparency (Figure 1.3), a lot of interest has been placed on the continued development of organic photovoltaics [14-17] as a viable solar power conversion technology. However, much of this development has been focused on improving PCE, lifetime, and developing manufacturing processes to scale the development to large areas. These are all issues that must be addressed prior to wide spread commercialization.

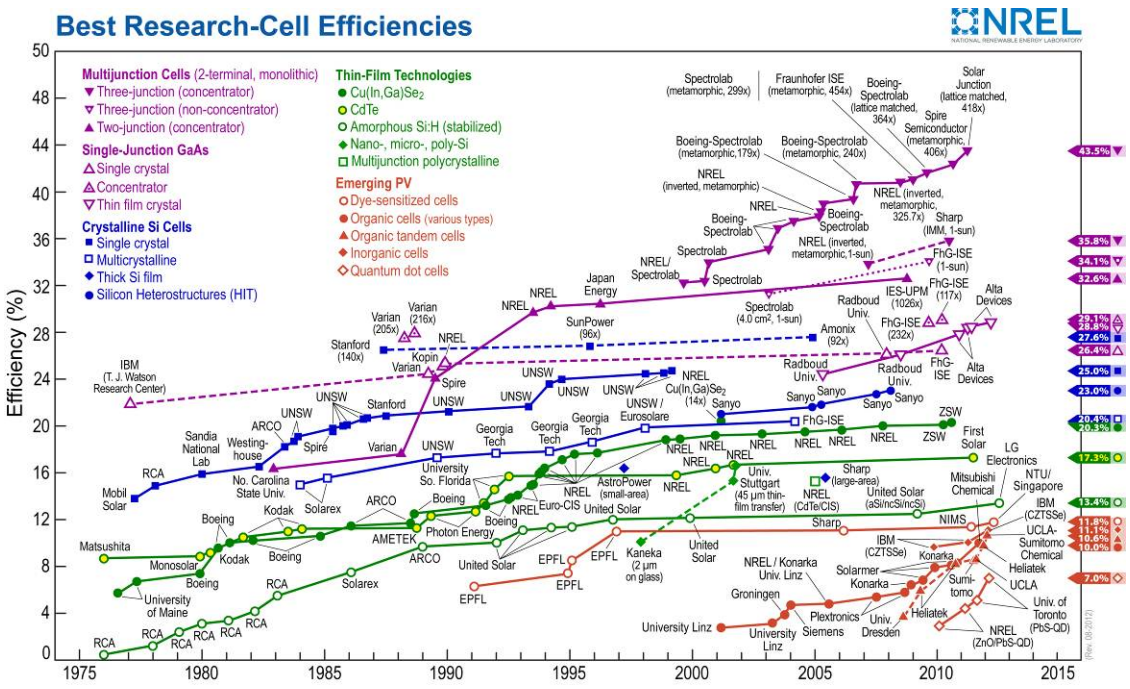

Figure 1.2. Recent report for efficiency of various solar cells by the National Renewable Energy Laboratory [13].

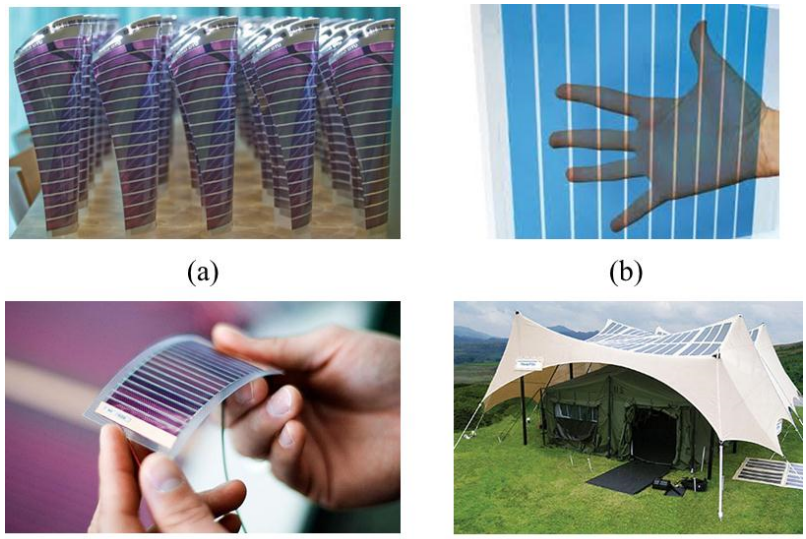

Figure 1.3. (a) Roll-to-roll processed organic photovoltacis (http://spectrum.ieee.org/green-tech/solar/plastic-solar-cells-roll-into-unlit-villages), (b) semi-transparent organic solar cell (http://www.greentechmedia.com), (c) highly flexible solar cell (http://gotpowered.com/2011/rise-of-organic-photovoltaics), and (d) large area organic solar cells (http:// solarpower-mart.com).

To define the performance of organic photovoltaics, several parameters such as power conversion efficiency (η), open-circuit voltage (V_{oc}), short-circuit current density (J_{sc}), and fill-factor (*FF*) are obtained from current density-voltage measurements as shown in Fig. 1.4. The current density, J, is the current divided by device area. Open-circuit voltage (V_{oc}) is the voltage when $J = 0$ and short-circuit current density (J_{sc}) is the current density when $V = 0$. While V_{oc} and J_{sc} set the boundaries of power production in a solar cell, the maximum power density (P_{max}) occurs at the voltage V_{max} and current-density J_{max}, as shown in Fig. 1.4. Fill-factor (*FF*) is defined by Eq. 1-1 which is the ratio of the actual maximum power ($V_{max} \times J_{max}$) to the theoretical maximum power ($V_{oc} \times J_{sc}$). The power conversion efficiency (η) is defined in Eq. 1-2 where P_{in} is the incident light power per unit area.

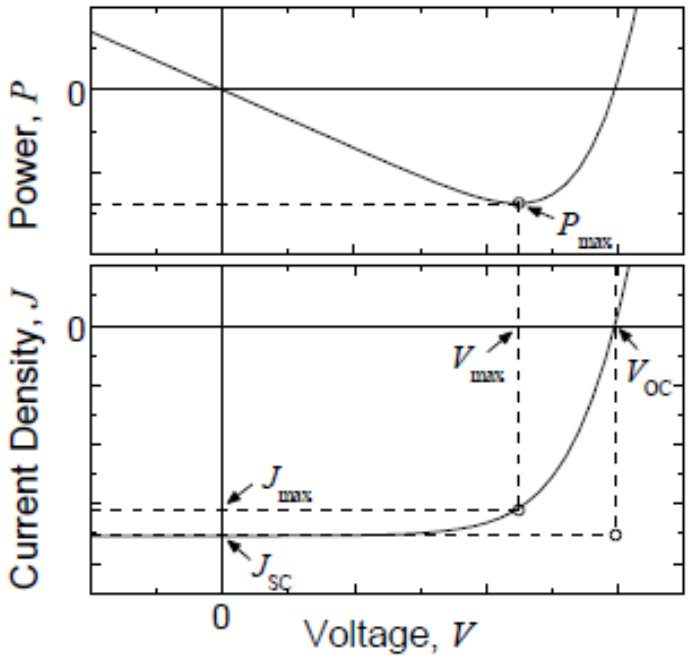

Figure 1.4. Typical graphs of power and current density vs. voltage for a solar cell [18].

$$FF = \frac{V_{\max} \times J_{\max}}{V_{oc} \times J_{sc}} \quad (1 - 1)$$

$$\eta = \frac{V_{oc} \times J_{sc} \times FF}{P_{in}} \times 100\% \quad (1 - 2)$$

Conventional organic photovoltaics, as depicted in Fig. 1.5(a), typically consist of a substrate (glass or plastic), a positive electrode (ITO: indium tin oxide), an interface modifier (e.g., PEDOT:PSS: Poly(3,4-ethylenedioxythiophene Poly(styrenesulfonate)), a phase separated bulk heterojunction (BHJ) active layer (e.g., P3HT:PCBM: poly3-hexylthiophene and phenyl C61-butyric acid methylester), and a negative electrode (Ca, LiF-Al, etc.) [14, 17, 19, 20]. In conventional OPVs, the PEDOT:PSS layer is used to improve interface between the active layer and the electrode [21] and also used as a hole collection layer in OPV devices due to its high work function, high hole affinity, and good transparency [22]. Due to the energy band structure of these conventional devices, they require the use of low work function electrodes such as Ca or LiF-Al in order to have efficient electron collecting contacts. Due to the low ionizing potential of these materials, they are highly reactive and thus are susceptible to degradation when exposed to the environment (e.g., water vapor and oxygen in the atmosphere). Thus, the use of such low work function electrodes in OPVs is one source of their environmental instability and reliability that must be addressed.

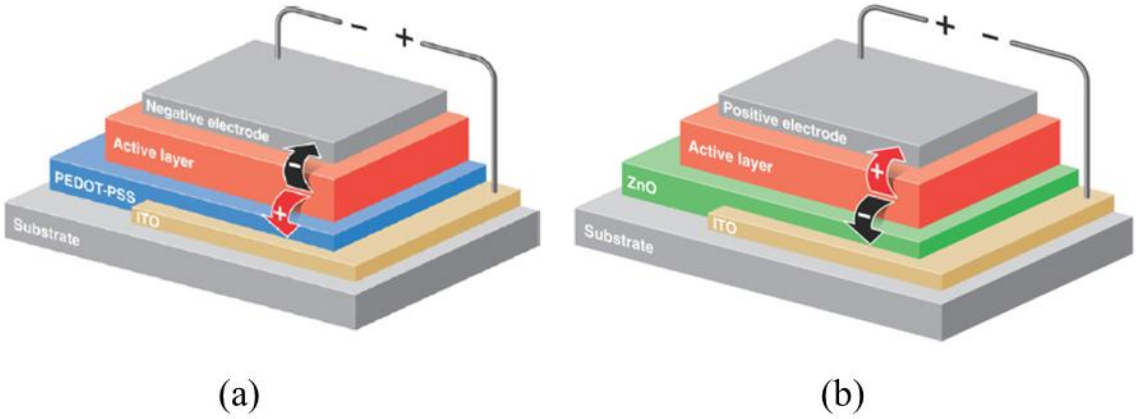

Figure 1.5. OPV architectures: (a) a conventional solar cell and (b) an inverted solar cell [23].

While the operation of organic photovoltaics is complex from a fundamental molecular point of view, there are four general steps that are needed to convert solar energy into electrical energy. First, the donor layer must absorb solar photons and create electron-hole pairs (excitons). The optical properties (absorption spectra and band gap of the donor layer) will ultimately influence the portion of the solar spectrum that is absorbed by the cell. The band gap of the donor material can be changed by the chemical composition of the donor layer [24]. In general, lower band gap donor materials will absorb a greater percentage of the solar spectrum than large band gap materials. However, this absorption also depends on the thickness of the materials which must be limited based on considerations of excition diffusion that governs the operation of an OPV. In the second step, once the light is absorbed in the active region, bound electron-hole pairs, or excitons, are created which must be separated to create free electrons and holes.

Thirdly, the excitons in the absortion layer or donor layer must diffuse to a region that is favorable for separating the exciton into the free carriers. This is facilitated in many OPVs by the use of small molecules such as PCBM that have a high electron affinity as acceptor materials. Since the mobility (typically 2×10^{-3} $cm^2V^{-1}s^{-1}$ for P3HT:PCBM BHJ active layer [25, 26]) and exciton diffusion length are small, this governs the distance of separation between donor and acceptor materials in OPVs before the created charge pair simply recombines, losing the opportunity to collect the created charge from the absorbed photon. The small spacing between the donor and acceptor material is facilitated by blending the donor material (e.g., P3HT) and acceptor material (e.g., PCBM) to form a phase separated film with nanoscale morphology as shown in Fig. 1.6. This is called a bulk heterojunction (BHJ) solar cell since heterojuncions are formed by the nanoscale phase separated material throughout the bulk of the active layer. These phase separated regions form a percolation network that allows the separated charges to travel towards the hole collecting electrode and the electrons towards the electron collecting electrode.

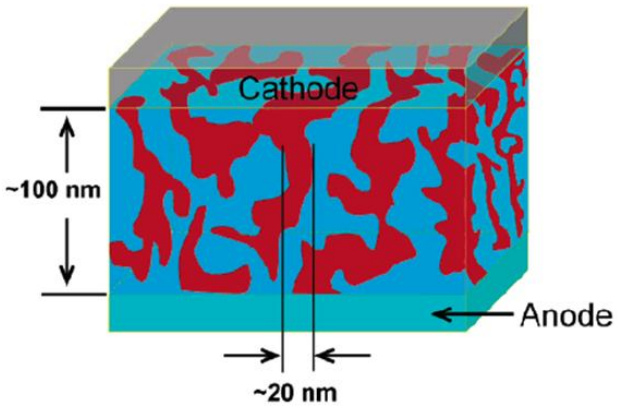

Figure 1.6. Conceptual 3-dimensional morphology of a phase separated bulk heterojunction active layer (electron donor and acceptor in different colors) [27].

Fourth, the electrons and holes must be efficiently collected by their hole selective and electron selective electrodes to provide current flow from the OPV [28, 29]. Critical to the operation of these excitonic solar cells is the alignment of the work function of the anode and cathode with the HOMO (highest occupied molecular orbital) and LUMO (lowest unoccupied molecular orbital) levels of the donor and acceptor layers, respectively, to reduce energy barriers in charge collection from the solar cells (Figure 1.7). Thus, a high work function electrode (e.g., ITO) is necessary for contact to the P3HT layer while a low work function electrode (e.g., Ca, LiF-Al) is used for electron selection from the PCBM layer. The use of these low work function electrodes, however, presents a significant risk to the long term durability of OPVs.

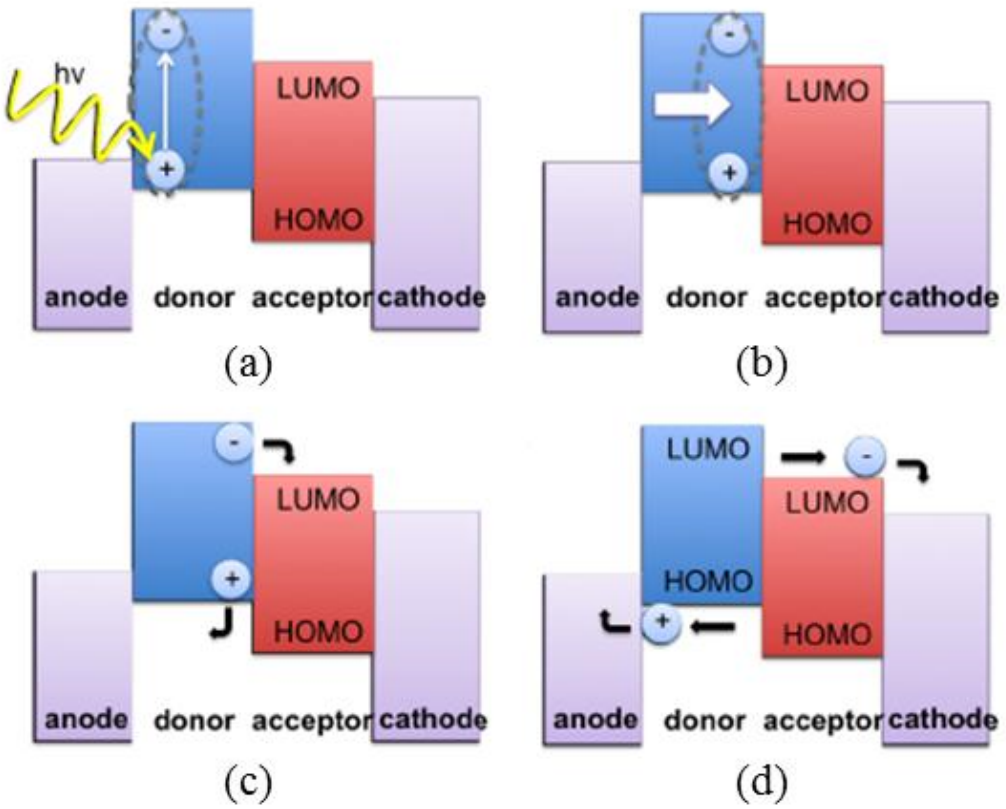

Figure 1.7. Basic operation of organic photovoltaics as viewed through an energy band diagram: (a) light is absorbed by the organic donor layer and electron-hole pairs (exitons) are created, (b) the exitons migrate to the interface of the donor-acceptor region, (c) the electrons and holes are separated, and (d) the separated charges are transported to the anode and cathode [30].

As briefly mentioned, reliability issues (chemical and mechanical degradation) can lead to a device failure. The chemical degradation can potentially give rise to the reliability concerns in OPV devices by degrading electrical contacts as well as the electrical properties of the active layers [28, 31-38]. In order to reduce the susceptibility of the OPV devices to the chemical degradation, two different methods are used to improve device lifetimes. Since the active layer and the low work function electrode are very susceptible to the permeation from water vapor and oxygen through defects (e.g., pinholes) in the electrodes as shown in Fig. 1.8 [9, 34, 39-45], the OPV must be sealed

from the environment. This is often done by using ultralow permeation barrier films to prevent the ingress of water vapor and oxygen into the solar cell [46-50]. These barrier layers can be complex combinations of alternating layers of inorganic and organic layers that can be deposited by vacuum deposition as shown in Fig. 1.9.

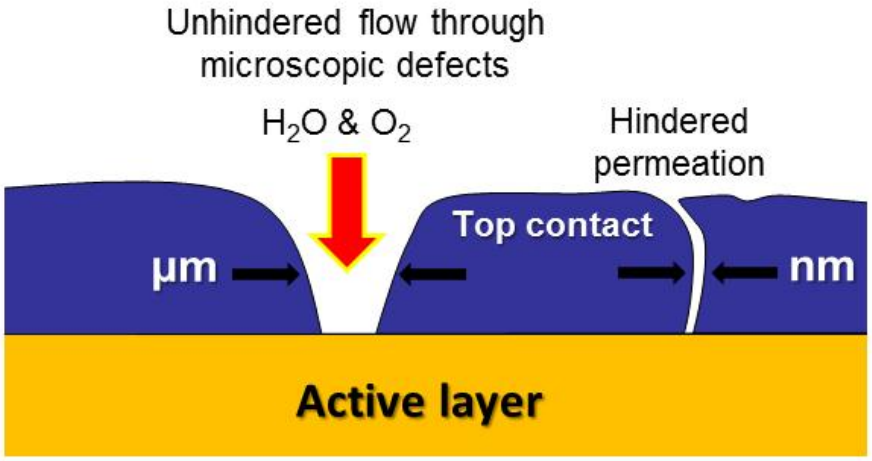

Figure 1.8. Permeation path for H_2O and O_2 through the microscopic pinhole defects in the top contact.

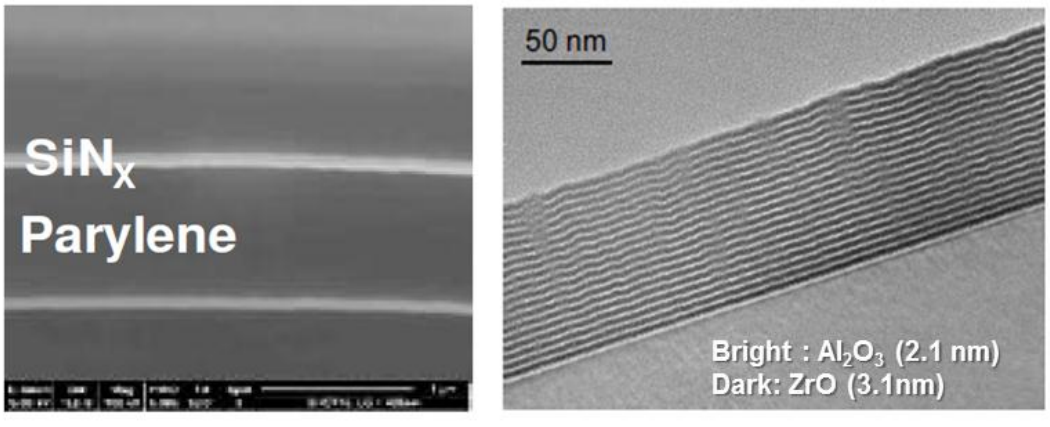

Figure 1.9. (a) SEM image of organic-inorganic (SiN_x/Parylene) combination [50] and (b) TEM image of Al_2O_3/ZrO nanolaminates [51].

While encapsulating the OPV with barrier films is one method to improve the lifetime of the devices, another approach is to reduce the environmental sensitivity of the active layers and electrodes. This can be done, to first order, by removing the low work function electrode from the conventional OPV architecture. By making the ITO an electron selective contact, more stable materials such as Ag can be used as a hole collecting contact, thus eliminating the use of Ca or LiF/Al. In this architecture (Figure 1.5(b)), the order of the film deposition is reversed from that seen in Figure 1.5(a) and is thus called an inverted OPV [16, 23, 36, 52-55]. To make the ITO an electron selective contact, materials such as ZnO are deposited on the ITO to serve as a hole blocking layer as shown in Fig. 1.10. An additional high work function material (PEDOT:PSS, MoO_x, NiO_3, etc.) is placed on the back electrode to collect the positive holes [56-60], as shown in Fig. 1.5(b) and 1.10. By using high work function materials on the top of the inverted OPV structure, these devices become much more air stable as already tested under outdoor conditions for one year by Matthew *et al*. (Fig. 1.10(b)).

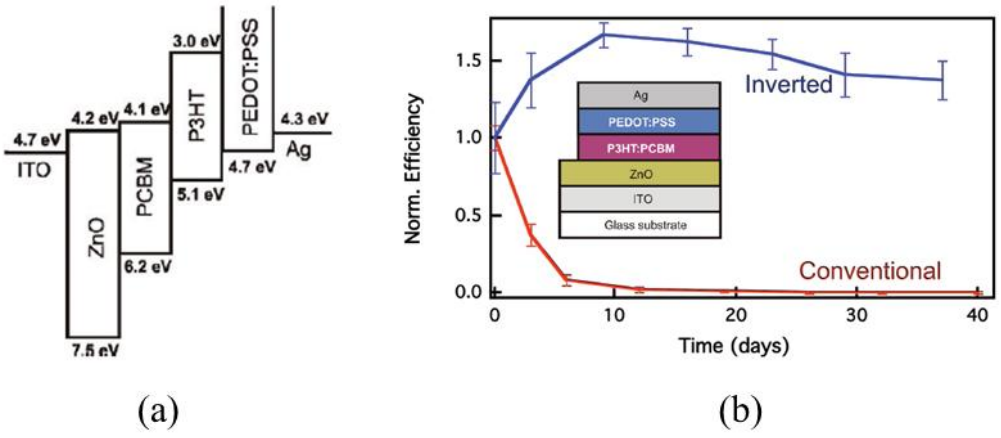

Figure 1.10. (a) Energy level diagram of a typical inverted organic solar cell [52], and (b) the stability of the power conversion efficiencies versus time of conventional and inverted organic photovoltaics exposed to air [61].

For flexible applications or applications subjected to mechanical loading, the mechanical degradation becomes another potential failure source. The mechanical reliability of the barrier films used for packaging devices has been studied primarily by analyzing the strain-to-failure or the critical bending radius that induces cracking of the inorganic layer in the barrier. Once cracks are generated, such damage provides direct pathways for environmental species to permeate through and reach the OPV device [62-66]. While most of the research has focused on strain-to-failure for crack initiation in inorganic barriers on plastic substrates, very little research has focused on the fundamentals of adhesive or cohesive failure within the barrier layers and/or OPV device architecture. To date, only a few studies have focused on the basic mechanical properties in organic photovoltaics and its implications on device reliability [11, 67].

1.2. Objectives of Dissertation

The objective of this dissertation is to provide a fundamental understanding of the adhesive and cohesive failure in inverted bulk heterojunction OPV devices and in barrier films used to protect them. To address the lack of information and understanding on the adhesive and cohesive failure in OPV devices, this work performed fundamental mechanical testing to measure the interfacial fracture toughness of interfaces and active layers in both multilayer barrier films and inverted OPVs. To test inorganic/organic barrier films, a series of four point bending (FPB) tests were performed to measure interfacial fracture toughness data using silicon nitride/polymethyl methacrylate interfaces (SiN_x−PMMA) as a model barrier film. Methods of improving the adhesion

between the organic and inorganic barrier layers were investigated through surface treatments as well as through modifying the geometry of the structure. Testing was also performed to investigate the interfacial fracture toughness of an inverted OPV structure using two different BHJ active layers (P3HT:$PC_{61}BM$ and PBDTTT−C:$PC_{60}BM$). In order to quantify the interfacial fracture toughness defining the weakest interfaces or layers in the inverted OPVs, a standard double cantilever beam (DCB) technique was used. The inverted OPV structure was also modified by changing the electrical contacts from inorganic to organic in a move towards an all polymer OPV. Overall, the goal of this study is to provide the initial quantification of the adhesion/cohesion strength at typical interfaces used in OPVs and barrier films, to understand methods that influence adhesion strength, and to determine methods to improve the adhesion strength for the long term mechanical reliability of OPV devices.

CHAPTER 2

BACKGROUND AND LITERATURE REVIEW ON RELIABILITY ISSUES

2.1. Introduction

This chapter is aimed at providing an overview of chemical and mechanical degradation modes that impact OPVs that have been reported in the literature. As a part of this chapter, encapsulation efforts to protect the OPVs are also briefly introduced as well as the limited studies of the adhesion/cohesion in organic solar cells are covered.

2.2. Reliability Issues of Organic Photovoltaic Devices

2.2.1. Chemical Degradation

As briefly mentioned in chapter 1, when OPV devices are exposed to ambient conditions, they can degrade due to reactions with water vapor and oxygen [4, 8, 68]. The degradation of electrical contacts as well as the electrical properties of the active layers gives rise to the reliability concerns that impact device lifetimes [28, 31-38, 69]. The chemical degradation of the active layer in organic solar cells is a known degradation pathway due to the photo-oxidation of BHJ active materials when exposed to the solar spectrum and water vapor and oxygen simultaneously [4, 34]. Recent studies have shown that the P3HT:PCBM active layer in a PET/ITO/ZnO/P3HT:PCBM/PEDOT/Ag solar cell structure is very susceptible to oxygen when illuminated in ambient air conditions using a AM1.5G solar spectrum (1000 W/m^2) [61, 70]. By using the same

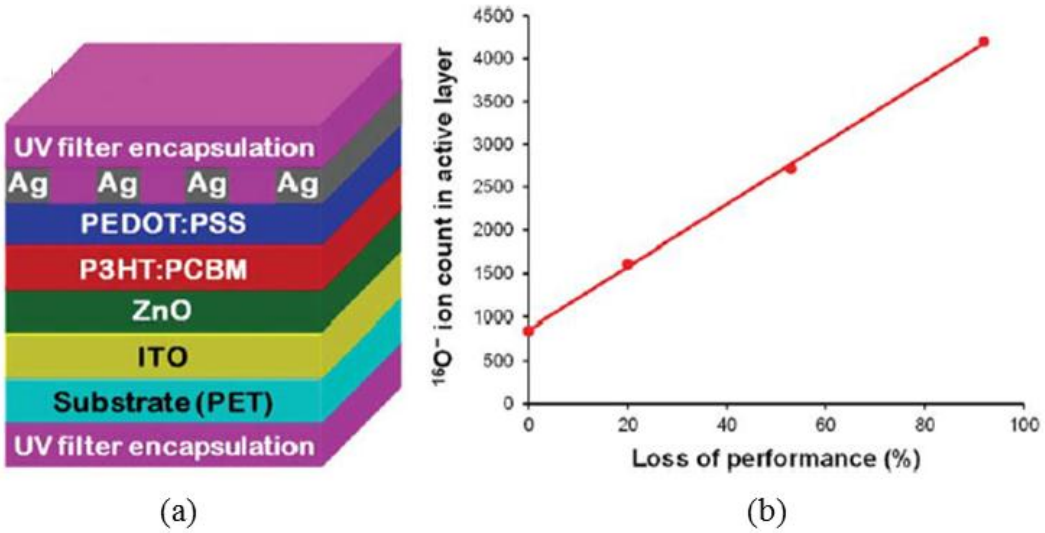

Figure 2.1. (a) Roll-to-roll fabricated OPV consisting of substrate (PET), ITO, ZnO, P3HT:PCBM, PEDOT:PSS, Ag, and encapsulation film and (b) OPV performance loss due to environmental exposure correlating to oxygen intensities of BHJ active layer measured by time-of-flight secondary ion mass spectrometry (TOF-SIMS) [4].

structure, it was also verified that the photo-oxidation process using a roll-to-roll processed polymer solar cell (PET/ITO/ZnO/P3HT:PCBM/PEDOT:PSS/Ag/ encapsulation architecture) illuminated with a AM1.5G solar spectrum (1000 Wm^{-2}) in ambient air (Fig. 2.1(a)) can directly contribute to the solar cell performance loss, as shown in Fig. 2.1(b) [4]. The relative photo-oxidation of the active layer (P3HT:PCBM) was measured by the relative oxygen uptake using a time-of-flight secondary ion mass spectrometry (TOF-SIMS) indicating the roll-to-roll processes solar cell completely loses its performance by having the highest oxygen content in the P3HT:PCBM BHJ active layer, as shown in Fig. 2.1(b) [4].

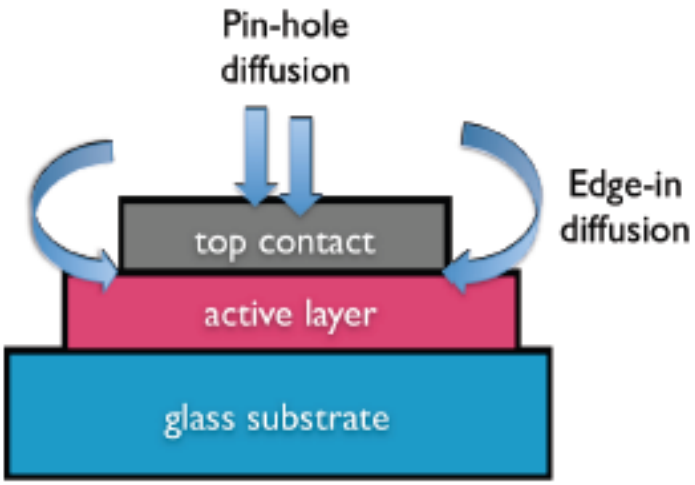

Figure 2.2. Schematic diagram of an organic solar cell with two main diffusion paths (pin-hole and edge-in diffusion) from water vapor and oxygen [61].

Other major chemical degradation mechanisms are the oxidation and loss of electrical contact of the low work function electrode [34, 35, 69, 71, 72]. It was shown with two different diffusion pathways carried out with lifetime measurements concluding that the diffusion effects from edge of the devices and pinhole of the top electrical contact layer are main proponents for the ingress of oxygen and water vapor into the active layer of the device [4, 35, 61, 73, 74], as shown Fig. 2.2. Fig 2.3 shows a lateral process of degradation through the edge-in diffusion using photocurrent density maps in a MDMO−PPV:PCBM based organic solar cell consisting of a glass substrate, ITO, PEDOT:PSS, active layer, and Al top contact [73]. Even though two different diffusion pathways from the edge and the top contact of the device takes place simultaneously, the photocurrent map after the degradation in air in the dark for 2 weeks measured under a calibrated solar simulator ($1000 W/m^2$) (Fig. 2.3(b)) still indicated that the lateral diffusion plays a role in the degradation of the organic solar cell devices.

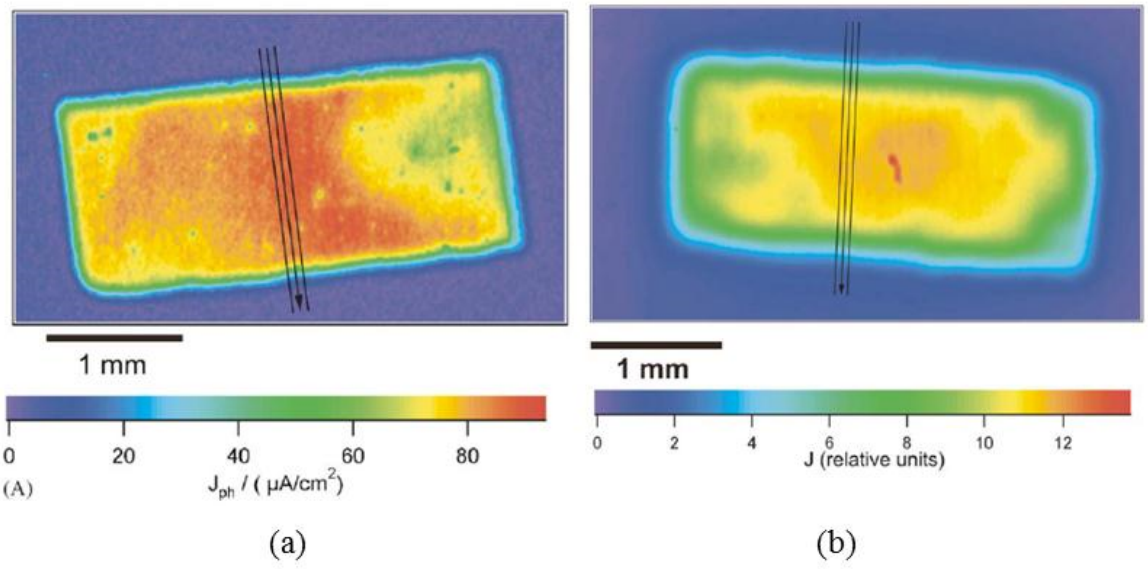

Figure 2.3. Photocurrent density maps in a MDMO−PPV:PCBM based organic solar cell consisting of a glass substrate, ITO, PEDOT:PSS, active layer, and Al top contact: (a) an initial photocurrent density image after the device fabrication and (b) a photocurrent density image after the degradation in air in the dark for 2 weeks [73].

More recently, Lloyd *et al.* clearly observed the effects of simultaneous lateral diffusion and diffusion through the top Al contact using a P3HT:PCBM BHJ based inverted OPV [74], as shown in Fig. 2.4. By comparing the before and after current maps (Fig. 2.4), Lloyd *et al.* defined that significant edge-in diffusion occurs as indicated by the loss of the photocurrent density from the sides of the device, as shown in Fig. 2.4(b). In addition, defects in the device nucleate and grow radially forming dark spots in the photocurrent output [74]. The formation of such dark spots has been also observed in the active layer of unencapsulated organic light emitting devices (OLEDs) where the pinhole defects in the low work function metal contact permits the ingress of water vapor and oxygen. After passing through the pinholes, the permeants diffuse radially which leads to device failure by causing oxidation or delamination of the top metal contact [4, 8, 75], as described in Fig. 2.5.

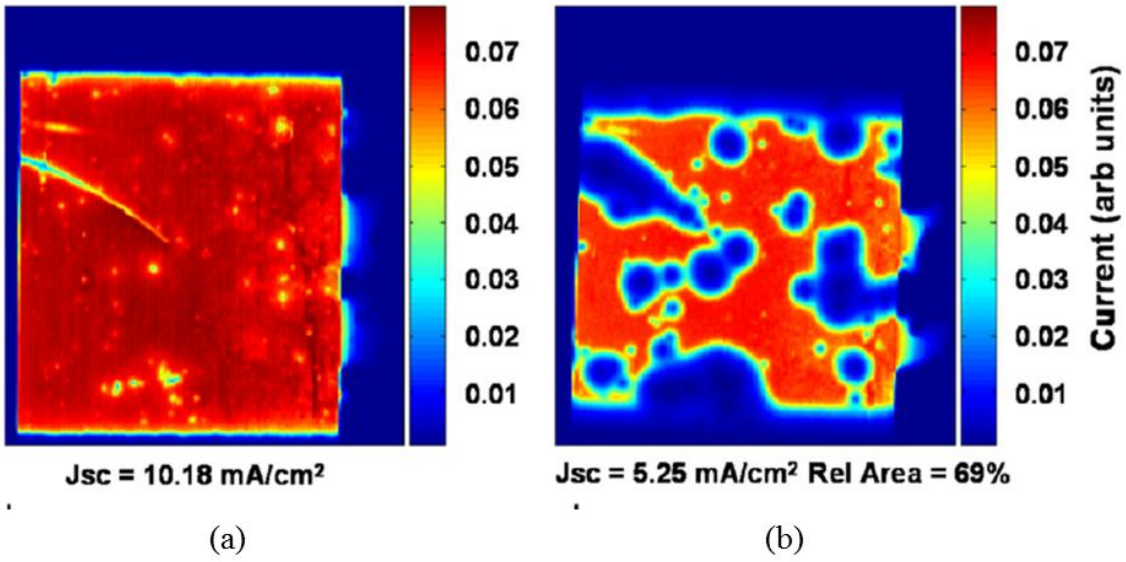

Figure 2.4. Photocurrent density maps in a P3HT:PCBM based inverted organic solar cell consisting of glass substrate, ITO, ZnO, active layer, PEDOT:PSS, and Ag top contact: (a) an initial photocurrent density image right after the device fabrication and (b) a photocurrent density image after 168 hours exposure under 100 mW/cm^2 with a sulfur plasma lamp in air at 37°C [74].

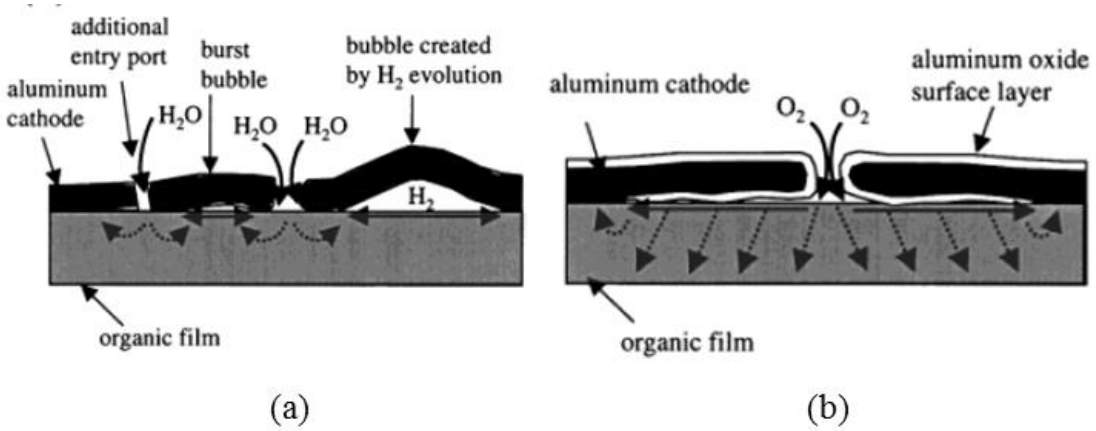

Figure 2.5. (a) Degradation mechanism of polymeric light emitting films in OLEDs by water vapor diffusion through the pinholes and (b) formation of aluminum oxide layer at the cathode/organic light emitting layer interface in OLEDs [8].

Other reports have also verified that oxygen and water diffuse into the OPV devices through microscopic pinholes in the cathode [9, 34, 39-45]. The oxidation that occurs in the organic sub-layers can lead to material expansion in the device that becomes worse when the devices are illuminated simultaneously [34]. It was also found that in addition to the delamination between the active layer and top metal contact (Fig. 2.5), extensive oxidation and void formation at the Ca/Al contact in conventional organic solar cell consisting of ITO, PEDOT:PSS, P3HT:PCBM BHJ active layer, Ca, and Al [35], is possible as shown in Fig. 2.6. Therefore, the void formation and oxidation at the Ca/Al contact reduce the contact area at the interface, reducing the performance of the OPVs causing device failure [35, 76].

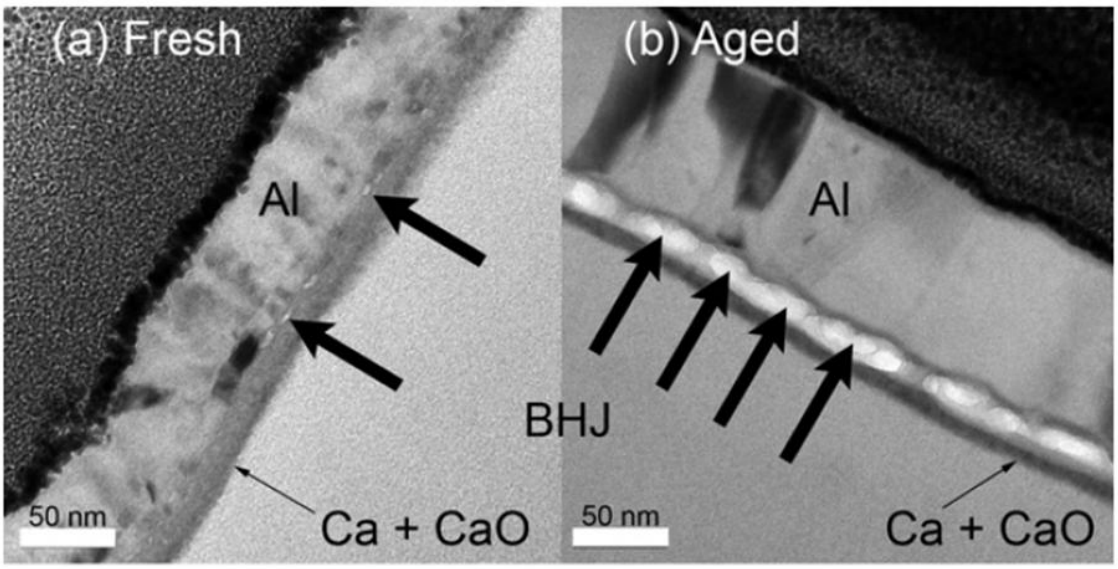

Figure 2.6. TEM images of: (a) conventional solar cell consisting of ITO, PEDOT:PSS, P3HT:PCBM BHJ active layer, Ca, and Al and (b) after the degradation in air for 40 days where arrows indicate the void formation [35].

As an effort to reduce the susceptibility of OPVs to chemical degradation, researchers have developed inverted OPVs where functional oxides and phosphonic acids (Fig. 1.10 (a)) have been used to create electron selective contacts at the ITO interface, allowing high work function electrodes to be used on top of the device [23, 52, 56-60], as shown in Fig. 1.5(b) and 1.9(b). These devices have been shown to be more stable and are the most promising for increasing OPV lifetime [61, 77] as shown in Fig. 1.9(b). By using the inverted OPV structure based on a P3HT:PCBM active layer, a 14 month (≈10,000 hours) outdoor lifetime was reported by Hauch *et al.* with encapsulated solar cells with a flexible gas barrier material (water vapor transmission rate, WVTR, 0.03 g/m^2/day at 38°C/100%RH, Fig. 2.7) tested at Konarka in a roof top testing setup in Lowell, MA (USA) [77], as shown in Fig. 2.8.

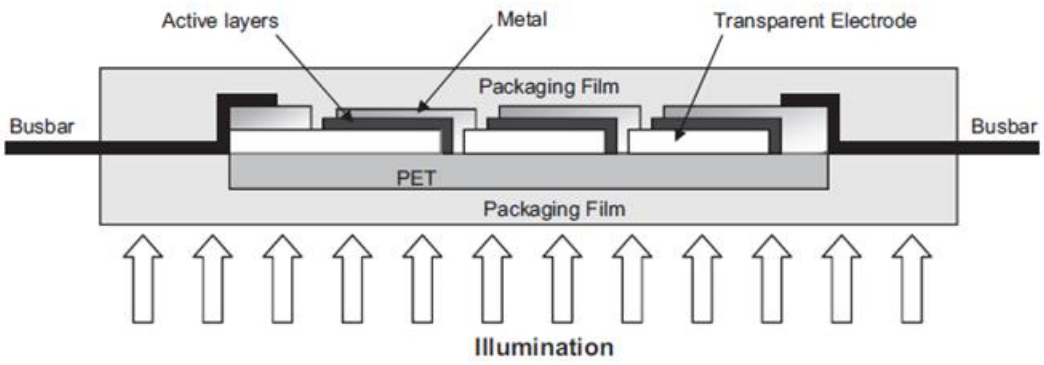

Figure 2.7. Schematic diagram of P3HT:PCBM BHJ active material based inverted solar cell [77].

Figure 2.8. Konarka roof top testing setup in Lowell, MA (USA) when the inverted solar cells are facing up at an angle of 421° from the horizontal [77].

2.2.2. Development of Barrier Films

While there have been tremendous efforts to develop more environmentally stable inverted OPV architectures [23, 52, 56-60], encapsulation barrier films also have been developed to protect the OPV devices from water vapor and oxygen [4, 50, 69, 78-81]. Previously, most of the packaging work on organic electronics has been done with glass substrates where the glass is sealed around the device in an inert atmosphere (nitrogen or argon environment) using UV-cured epoxy and desiccant materials such as calcium oxide and barium oxide [68], as shown in Fig. 2.9(a). However, to achieve high flexibility, flexible substrates and encapsulation approaches such as barrier-coated flexible lids, thin flexible glass, and high quality thin film have been developed as shown in Fig. 2.9(b) and (c) [82, 83]. As shown in Fig. 2.9(b), barrier-coated flexible lids are used to seal the

organic devices using high performance sealing materials which is called indirect encapsulation. Since this method fabricates encapsulation barriers on the flexible substrate, this methodology allows for optimization of the barrier film on a single substrate (e.g., PET and PEN) while the lamination or sealing process is then tailored to the specific device. There is much interest in this process as it presents opportunities for higher manufacturing rates and potential for lower costs especially when applied in a roll-to-roll manufacturing process [84-86]. In addition, the use of higher processing temperatures may enhance the film's structural quality and mechanical properties that improves the overall performance of the barrier film [87].

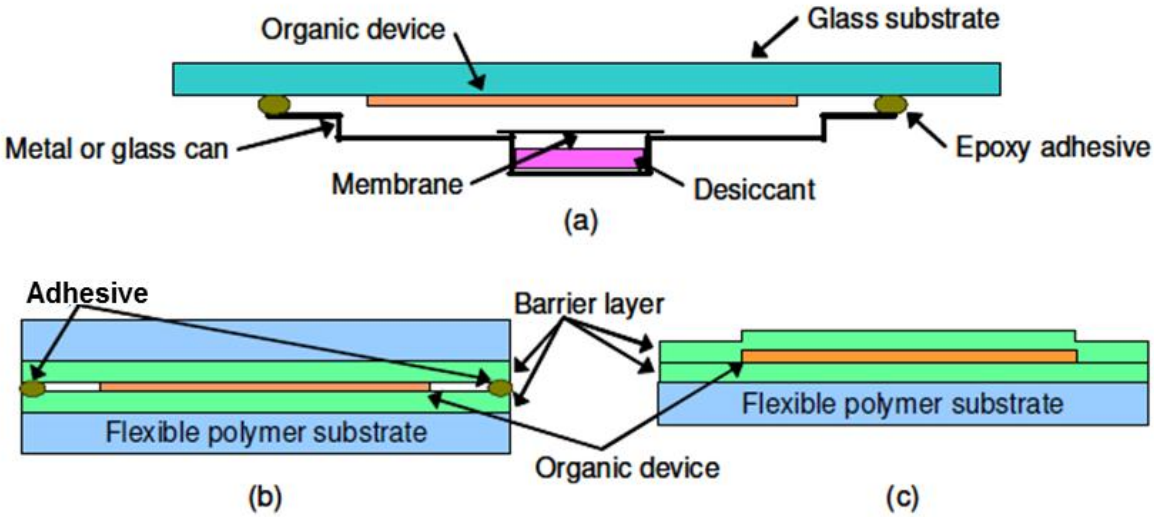

Figure 2.9. Schematic diagram of sealing techniques for organic electronic devices: (a) traditional approach on glass lids using epoxy adhesive and desiccant, (b) indirect sealing method using a high performance sealing material on flexible polymer substrate, and (c) direct sealing method on flexible polymer substrate [50].

While the lamination and sealing method of device encapsulation provides some distinct advantages in device packaging, one of the major weaknesses of this approach lies in the performance of the edge sealant itself. Edge sealants used in packaging of organic electronics typically consists of thermally or UV curable epoxies [68, 88, 89] or other adhesives [84-86, 90], which still provide diffusion pathway for water vapor and oxygen. However, this side permeation issue was resolved by using durable polyisobutylene edge sealants (HelioSealTM PVS 101) that shows a very low water vapor transmission rate (5×10^{-5} g/m^2/day measured at room temperature conditions [83]). Thus, in this dissertation, this indirect method using the durable polyisobutylene edge sealants (HelioSealTM PVS 101) was adopted to measure the barrier performance (WVTR) of the multilayer barriers using the Ca test method which will be explained in detail in chapter 4.

As another method, high quality thin films can also be directly deposited on devices as shown in Fig. 2.9(c). This direct film deposition method removes any side permeation issues which are the main problem of the indirect sealing method. However, special care is needed to check the compatibility of the barrier deposition process with the organic devices which can be damaged during film deposition. Thus, process optimization is a key aspect of this approach.

Regardless of the type of sealing method used in the packaging of OPVs, it is necessary to develop high performance barrier films to reduce the susceptibility of OPVs to the chemical degradation from water vapor and oxygen [4, 50, 69, 78-81]. Amongst various flexible encapsulation methods, nanoscale inorganic thin films have drawn great attention due to their outstanding characteristics such as being light weight, having high

transparency, and a high level of mechanical flexibility [50]. Thus, thin film barrier structures comprised of alternating inorganic/organic multilayers and low defect inorganic layers from atomic layer deposition (ALD) will be briefly reviewed.

Single layer inorganic films are the most desirable for developing ultra-barrier films with water vapor transmission rates (WVTR) less than 10^{-4} g/m^2/day. However, it is hard to achieve the ultra-barrier performance by only using a single inorganic film due to their inherent defects that develop during the deposition process. The presence of the film defects can give pathways for the permeation for water vapor and oxygen contributing to a high WVTR, as shown in Fig. 2.10(a). For these films, the diffusion of water vapor and oxygen is controlled by the presence of these defects and thus poor barrier performance is directly related to the relative number of micro defects in the barrier, as shown in Fig. 1.8 [65, 68]. This is often the case for vacuum deposited barrier films that use deposition techniques like sputtering and plasma enhanced chemical vapor deposition.

As Eq 2-1 shows, the WVTR of a film can be reduced by reducing the diffusion coefficient, D, or increasing the permeation path length l. While the defects in sputtered and PECVD grown films can be reduced by using smooth polymer surfaces for deposition, they will never be defect free. Thus D can only be reduced by a limited amount.

$$WVTR(t) = \frac{DC_s}{l}\left[1 + 2\sum_{n=1}^{\infty}(-1)^n \exp\left(-\frac{Dn^2\pi^2 t}{l^2}\right)\right] \qquad (2 - 1)$$

In Eq. 2-1, C_s is the concentration at the surface of the barrier, l is the film thickness, and t is time. Another option is to increase the diffusion path length in the barrier film (effectively increasing l). This is done by interrupting the growth of the inorganic layer and depositing a polymer film before continuing the inorganic layer growth. This causes the inorganic layer to nucleate again and the defects in this subsequent layer will not line up with the defects in the previously deposited inorganic layer. This alternating structure then causes the pathway through the defects to be interrupted and tortuous, effectively increasing the diffusion path length l and retarding the permeation of the water vapor and oxygen [48], as shown in Fig. 2.10(b) .

With respect to this approach, numerous groups have fabricated multilayer organic/inorganic barrier films. Most notably is the polyacyrlate/Al_2O_3 multilayer system (WVTR $\approx 10^{-6}$ g/m^2/day) developed at Pacific Northwest National Labs and commercialized as the Barrix ultra-barrier coating [1-3, 48, 75]. Namsu Kim *et al.* achieved a very low WVTR using SiN_x and parylene combinations [50], as shown in Fig. 2.11. By having five dyads of SiN_x/parylene (Fig. 2.11(a)), an effective WVTR value of 2.6×10^{-5} g/m^2/day was obtained while additional dyads of SiN_x/parylene beyond four pairs does not show any enhancement in terms of the WVTR. While not exhaustive, additional ultra-barrier films with multilayer architectures have been reported in [48, 68, 82, 91, 92].

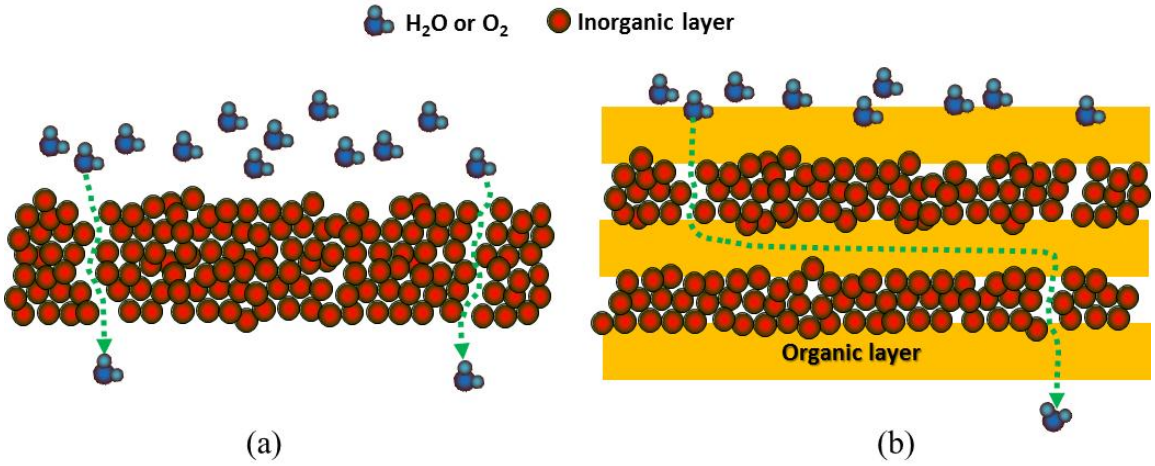

Figure 2.10. Permeation pathways of water vapor and oxygen through barrier film defects: (a) single layer and (b) multilayer structure using organic and inorganic film combination having tortuous pathways for the water vapor and oxygen permeation.

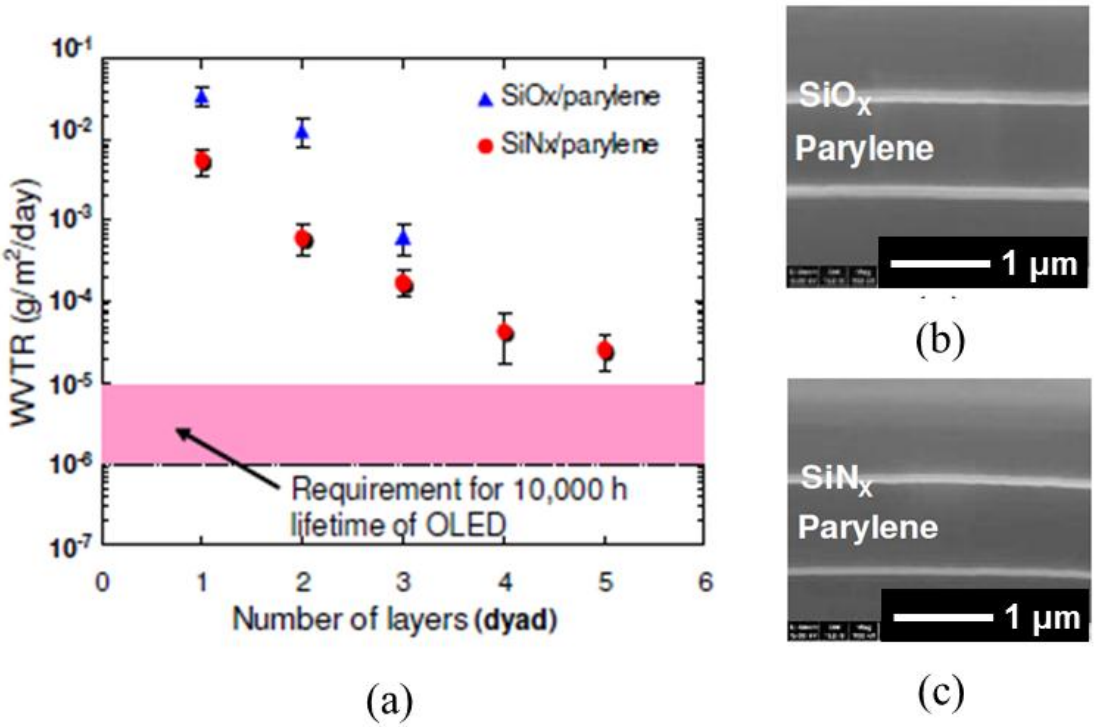

Figure 2.11. (a) Water vapor transmission rate (WVTR) using SiN_x/parylene combination when the WVTR decreases by increasing the number of SiN_x/parylene dyads, (b) cross sectional image of SiO_x/parylene, and (c) cross sectional image of SiN_x/parylene [50].

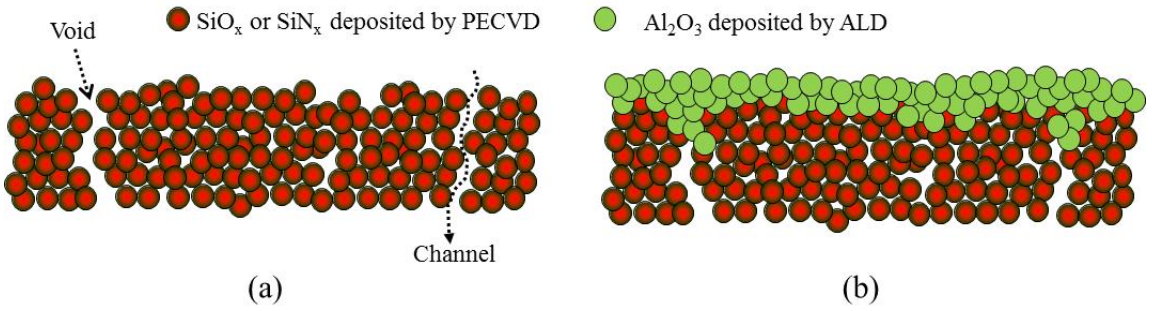

Figure 2.12. (a) SiO_x or SiN_x films with defects deposited by PECVD and (b) a hybrid barrir film architecture consisting of Al_2O_3 (by ALD) passivated SiO_x or SiN_x (by PECVD) which improve the overall barrier performance [50].

A different approach to passivate the defects in barrier structures has been developed that uses solely inorganic films to achieve the ultralow permeation rates. A hybrid encapsulation method using PECVD (SiO_x and SiN_x) and ALD (Al_2O_3) utilizes the low defect and conformal coating characteristics of ALD deposited films to passivate the defects in a PECVD deposited film [47, 49, 93-95]. Fig. 2.12 shows how the ALD deposited film (Al_2O_3) passivates the film defects deposited by PECVD (SiO_x or SiN_x). As the simplest method, single ALD deposited films using an ideal pinhole free film is also used to achieve ultra-barrier performance with WVTR being as low as 10^{-6} g/m^2/day [49, 79, 96]. While such films are very dense, pinhole free, and have a critical thickness on the order of 10 nm, water vapor can still permeate through ALD layers made of Al_2O_3 through hydration reactions forming $Al(OH)_3$ [97] .

In addition to single layer films, some researchers have pursued the development of ALD nanolaminates for their intrinsic characteristics such as high film density, low number of defects, and conformal coating at low temperature (< 110°C) [94, 98]. Al_2O_3 and ZrO nanolamintes structures (Fig. 2.13(a)) show water vapor transmission rate (WVTR) and oxygen transmission rate (OTR) on the order of 10^{-5} g/m^2/day and 10^{-2}

cm^3/m^2/day measured under a controlled environment of 70% humidity and 70°C which corresponds to the WVTR on the order of 10^{-7} g/m^2/day at the room temperature conditions summarized in Table 2.1 [51, 79]. This barrier performance enhancement is believed to be a result of a dense intermixed phase at the interface between Al_2O_3 and ZrO [99]. In addition, various types of ALD nanolamintes using different materials have been developed to improve the film quality which can also lead to high encapsulation barrier performance such as Al_2O_3 and ZnO (Fig. 2.13(b)) [100, 101], HfO_2 and ZrO_2 [102], Al_2O_3 and TiO_2 [103], etc.

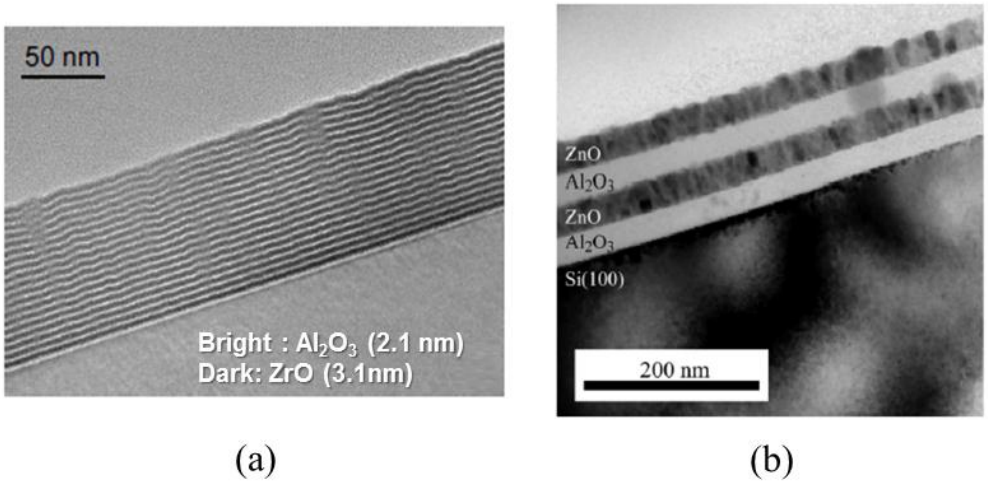

Figure 2.13. (a) TEM image of Al_2O_3/ZrO nanolaminates [51] and (b) TEM image of Al_2O_3/ZnO nanolamintes [101].

Table 2.1. WVTR and OTR of Al_2O_3 and Al_2O_3/ZrO_2 [79].

Barrier layer (thickness [nm])		Permeation rate for water [$g\,m^{-2}\,day^{-1}$]	Permeation rate for oxygen [$cm^3\,m^{-2}\,day^{-1}$]
Al_2O_3	(100)	3.5×10^{-4}	1.2×10^{-1}
$Al_2O_3 + ZrO_2$	(100)	6.4×10^{-5}	2.1×10^{-2}
Al_2O_3	(130)	9.9×10^{-5}	3.3×10^{-2}
$Al_2O_3 + ZrO_2$	(130)	4.7×10^{-5}	1.6×10^{-2}

2.2.3. Mechanical Degradation

To date, much effort has gone into understanding the chemical basis for the degradation of materials in OPV devices. However, in addition to the chemical degradation of solar cells, there is also high possibility for mechanical degradation which can lead to the failure of organic solar cell devices. In a review of the literature, very little focus has been placed on the measurement and understanding of the mechanical reliability. While flexural testing and cracking of transparent conductive electrodes has been widely studied [62, 63, 65, 66, 104, 105], the issue of adhesion at interfaces in OPV devices has not received significant attention.

In studies of transparent electrodes, Lewis *et al.* performed experiments to correlate the normalized electrical resistance of ITO with the bending radius of the ITO, as shown in Fig. 2.14 [65, 105]. Leterrier *et al*. also provided a comprehensive review for thin film properties on flexible substrates (coating defects, cohesive strength, and internal stress state) by using indentation and scratch tests, bending test, and fragmentation test [63, 64, 104]. As shown in Fig 2.15, Leterrier defined three

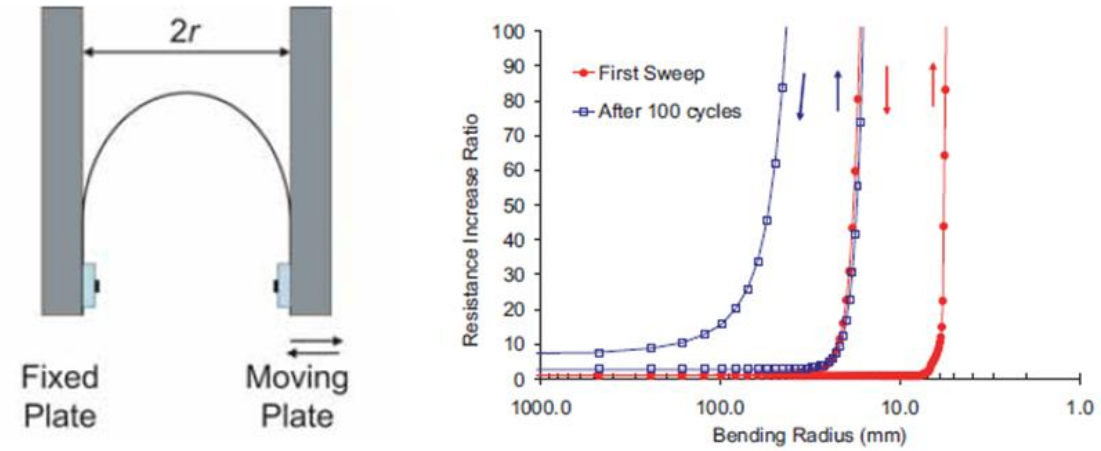

Figure 2.14. (a) Schematic diagram of a two-point bending test method for evaluating mechanical failure in thin films on flexible substrates and (b) resistance change of ITO on a polyethylene naphthalate (PEN) substrate as a function of bending radius (before and after 100 cycles to 5 mm) [65].

primary stages of cracking using the fragmentation test method. These were random cracking, mid-point cracking and initiation of transverse buckling, and delamination which can also be roughly predicted by mechanistic models [63, 106, 107]. Fig 2.15(c) shows the gradual fragmentation process of a SiO_x coating on a PET substrate [108]. However, most of the work focused strictly on transparent conductive oxides (TCOs) or the adhesion of oxides to polymers substrate. Thus, other critical layers such as the adhesion within a multilayer barrier film or the adhesion of active layers to their electrodes in OPV devices have yet to be investigated.

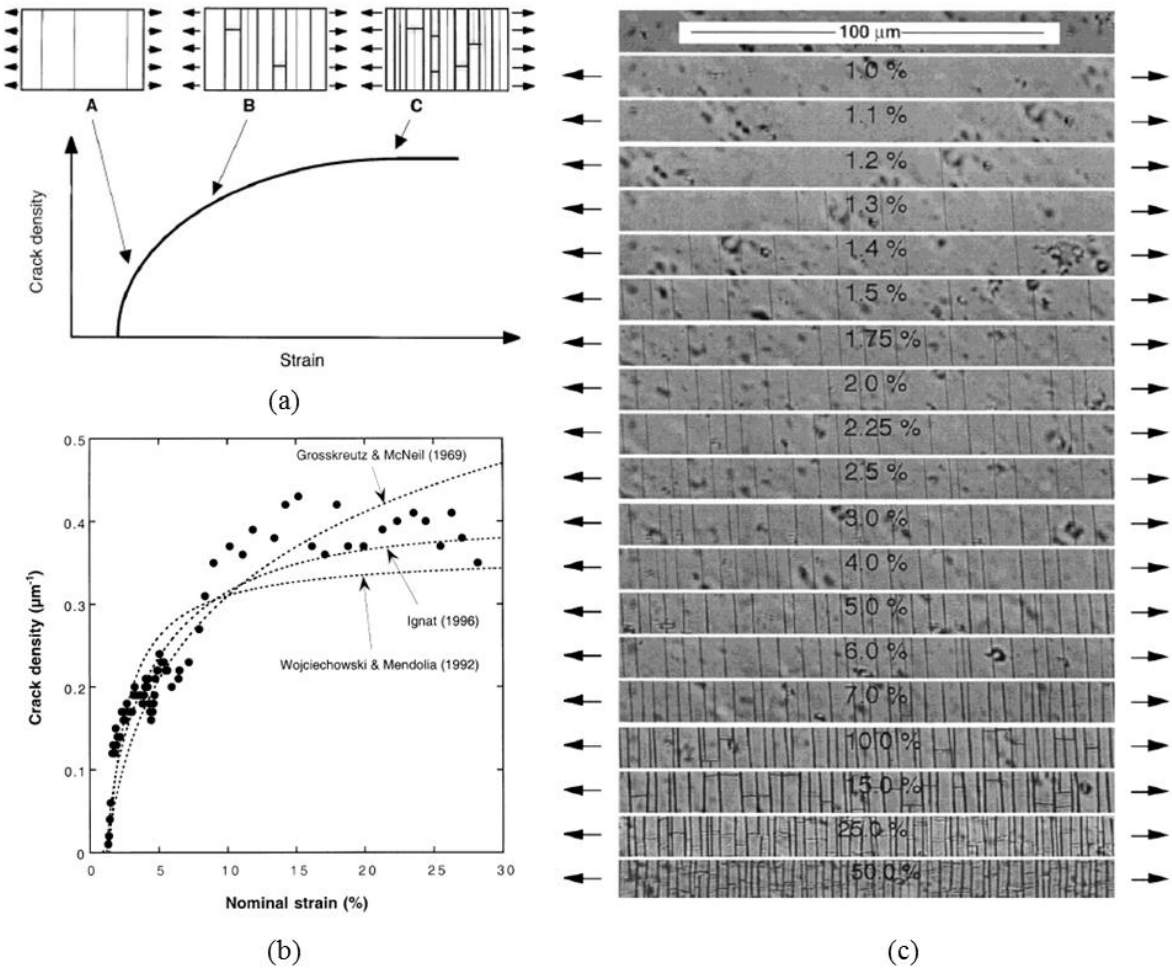

Figure 2.15. (a) Three main stages of coating fragmentation where A, B, and C represent random cracking, mid-point cracking and initiation of transverse buckling, and delamination [63], (b) crack density vs. normal strain (%) for the fragmentation process of a 100 nm thick SiO_x coating [63], and (c) fragmentation morphology of SiO_x coated PET substrate with different strains (arrows indicate loading directions) [108].

Overall, when there is chemical and mechanical degradation at interfaces and heterogeneous materials in organic solar cell devices, this can promote further loss of adhesion during device operation [109]. The loss of adhesion, especially at electrical contacts, can aid in the exciton recombination rate as well as series resistance leading to a reduction in solar cell fill factor [110-112]. In terms of other thin film solar cell architectures, it has been shown that the adhesion of the active semiconductor layer (e.g., CuInAlSe, $CuInS_2$, $CuInSe_2$, and CIGS) to the molybdenum oxide back contact is critical in improving and maintaining device efficiency [113-119]. However, much of the adhesion studies were performed using a simple "Scotch Tape Test" where a simple pass/fail criterion was used to show improvements in adhesion with changes in processing conditions. The inter-diffusion of CdS and the transparent conductive contact has also been accredited with the improvement of adhesion at TCO contacts in CdS solar cells that is critical for device efficiency [117]. It was also found that the low interfacial adhesion strength between Ag grid and Si_3N_4 moisture barrier poses a threat to the integrity of CIGS solar cells which provides channels for moisture ingress causing further decrease of adhesion strength and developing further cracks and delamination verified by a model structure (glass/Al/ITO/Ag grid/Si_3N_4 moisture barrier) [109], as shown in Fig. 2.16.

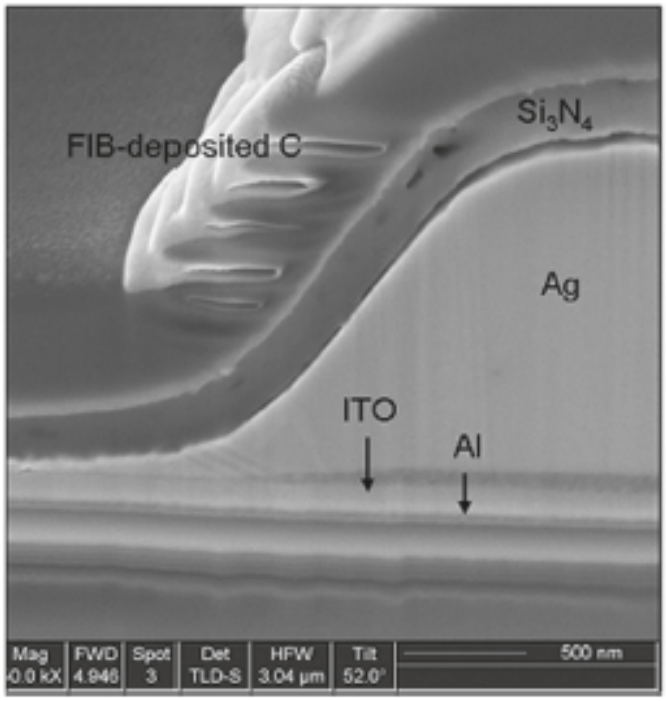

Figure 2.16. Cross sectional SEM image of a model substrate consisting of glass, Al, ITO, Ag grid, Si_3N_4 moisture barrier where there is interfacial failure between Ag grid and Si_3N_4 moisture barrier [109].

However, when investigating OPVs, very few studies exists which concern adhesion in the devices. An Al layer has been shown to be effective in increasing the adhesion between Ag grids and substrates in OPVs [120, 121]. It has also been stated that better wettability and adhesion of the photoactive layer to the electrodes is necessary for solution deposited OPVs [122]. While there are many nanoscale thin films in typical OPVs (Fig. 2.17), Dauskard *et al*. recently provided the interfacial fracture energy where they measured the fracture toughness of P3HT/PCBM solar cells with differing compositions ranging between 0.5-2.5 J/m^2. This value is actually lower than bulk glass (10 J/m^2, Fig. 2.18) showing the fragility of the system. They also found that the cohesive strength increases by having a higher weight percentage of P3HT due to the low affinity of interaction of PCBM fullerene within BHJ active layer using a

glass/ITO/PEDOT:PSS/P3HT:PCBM/Ca/Al/epoxy/glass structure [11, 67], as shown in Fig. 2.19.

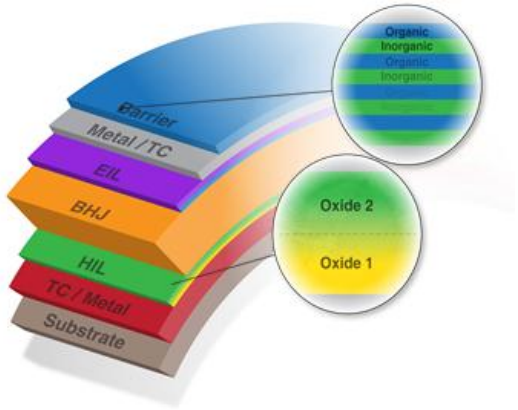

Figure 2.17. An example of a flexible organic solar cell showing the types of layers that can be used and revealing the types of interfaces that can be encountered.

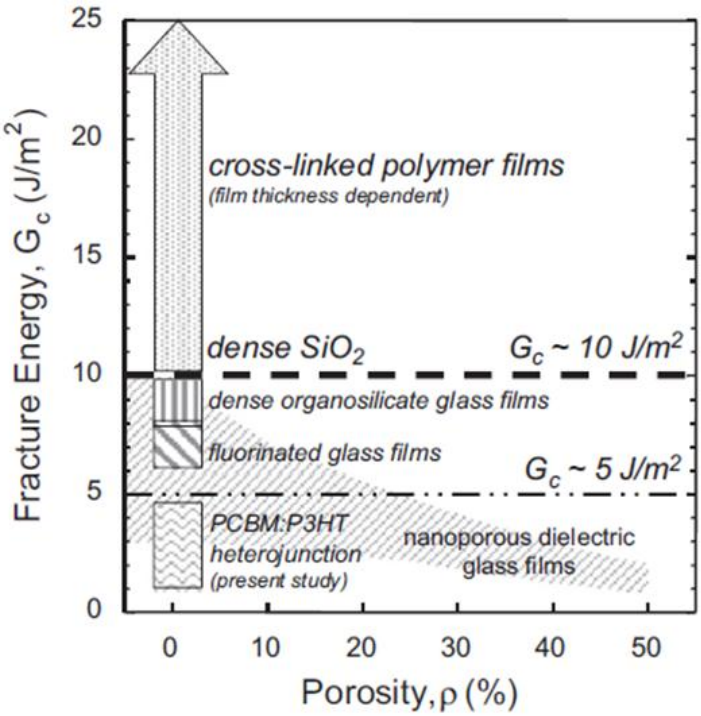

Figure 2.18. Reference values of cohesive fracture energy for commonly used dielectric materials in microelectronic devices compared with a bulk heterojunction P3HT:PCBM layer [67].

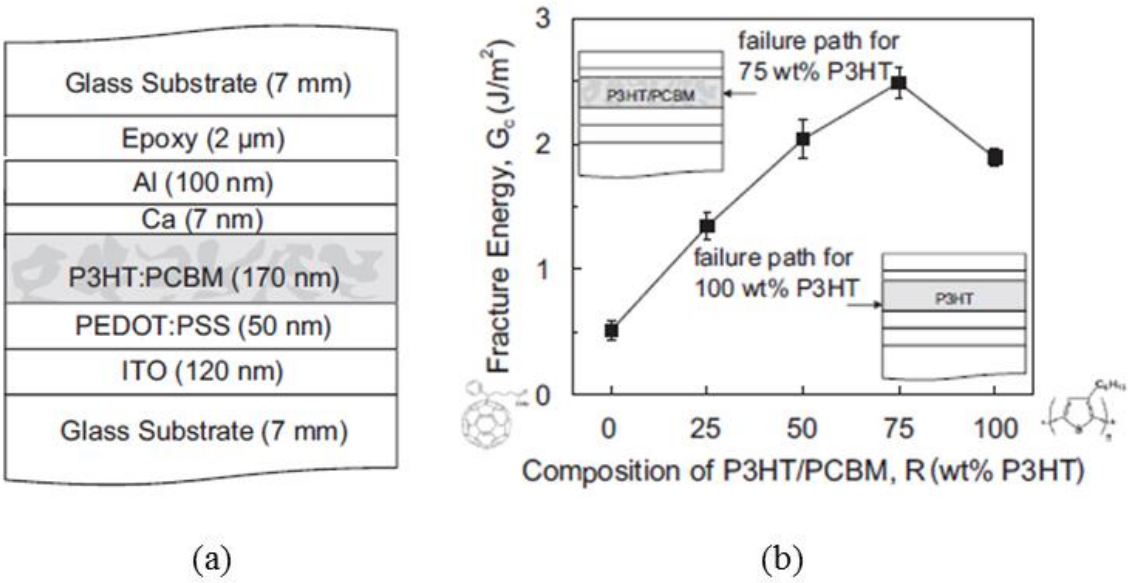

Figure 2.19. (a) Organic BHJ solar cell consisting of glass/ITO/PEDOT:PSS/P3HT:PCBM/Ca/Al/epoxy/glass and (b) cohesion strength values as a function of the weight percentage of P3HT and PCBM where insets indicate failure locations at 75 wt% and 100 wt% P3HT [67].

As shown in Fig. 2.19(b), there is a drop in the cohesion strength of BHJ active layer after the P3HT:PCBM mixture reached 75 wt% P3HT. This caused the failure mode to shift from the bulk of the active layer (cohesive) to the P3HT:PCBM – PEDOT:PSS interface (adhesive failure). This shift from cohesive to adhesive failure occurs because the relatively hydrophobic P3HT film forms a weak interface with the negatively charged hydrophilic PEDOT:PSS layer [11, 67]. Moreover, Dauskard *et al.* also measured the adhesion strength between P3HT:PCBM active layer and Ag top electrode with two different types of interface modifiers (PEDOT:PSS and V_2O_5), as shown in Fig. 2.20 [11]. In this study, they showed very low interfacial adhesion strength (G_c = 0.1-1.6 J/m^2) when PEDOT:PSS was used which can be enhanced by changing the composition ratio of P3HT and PCBM (Fig. 2.20(a)), annealing polymer solar cells as function of time, and replacing PEDOT:PSS with V_2O_5 (Fig. 2.20(b)). They demonstrated that V_2O_5 gives the

highest adhesion strength with G_c ranging from 75- 150 J/m^2) by forming a strong intermixed layer (≈ 10 nm) between P3HT:PCBM and V_2O_5 as shown in Fig. 2.20(b) [11]. While it is clear that the interfacial adhesion strength increased, no measurements of the power conversion efficiency were made with these devices. Thus, it is unclear what impact these changes will have on the operation of the devices and the viability of this method for use in OPVs.

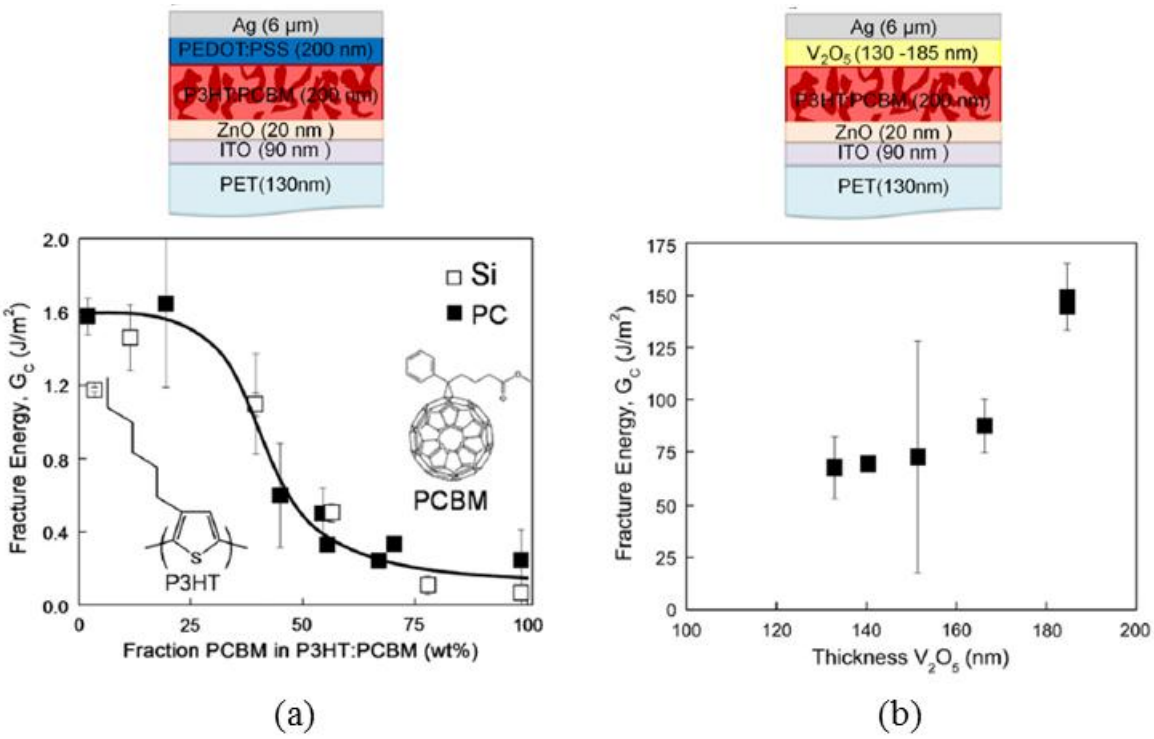

Figure 2.20. Fracture toughness at interfaces between P3HT:PCBM and: (a) PEDOT:PSS and (b) V_2O_5 [11].

By considering the currently available adhesion/cohesion data in the literature, it is concluded that the fracture toughness of the bulk heterojunction active layer is very low in terms of mechanical reliability. For roll-to-roll printed OPVs, it has also been shown that the adhesion of screen printed Ag contacts can vary with drying time [123, 124]. Also, the adhesion enhancement of Al contacts to the active polymer layers by annealing the organic solar cell was determined through the use of tape testing and AFM analysis proposing that the formation of C-Al and C-O-Al bonds were responsible for the improvement of the interface with annealing [125].

In addition to the interfacial adhesion strength within the solar cell layers, other concerns also have been raised regarding the need for mechanically reliable adhesion in barrier films for meeting 20 year lifetime requirements with acceptable levels of barrier performance [126-128]. However, no such studies have been reported in the literature, only the failure strength of adhesives used for barriers[129]. As stated in the objectives of this dissertation, it is a goal of this work to provide the initial measurements of the adhesion in these barrier films to address issues of mechanical adhesion.

CHAPTER 3

FUNDAMENTALS OF ADHESION

3.1. Introduction

This chapter provides a literature overview for the fundamentals of fracture mechanics, the mechanisms of adhesion, current adhesion studies, and general adhesion testing methods. We first introduce basic and fundamental linear elastic fracture mechanics (LEFM) that governs adhesive and cohesive failure. Next, we define how the interfaces are formed and various adhesion measurement techniques are introduced. Amongst the various techniques, FPB and DCB methods are explained in detail since these techniques are extensively used to determine the adhesion strength for inverted OPVs and barrier films in this dissertation.

3.2. Fundamental Concept of Fracture Mechanics

3.2.1. Linear Elastic Fracture Mechanics (LEFM)

Fracture mechanics governs the failure of materials due to the propagation defects that result from the breaking of atomic bonds in materials. Due to this localized damage process, the stresses around these discontinuities should be taken into consideration to elucidate the material failure. There are two methods to analyze the fracture of materials which includes the energy criterion and the stress intensity approaches. As a simple approach, linear elastic fracture mechanics (LEFM) is often applied to the analysis of

fracture. LEFM first assumes that the materials are isotropic and linearly elastic. There is only small scale yield of the material in the plastic zone around the tip of a crack and that all loading and unloading results in elastic deformation upon loading and recovery of deformation upon unloading. These assumptions allow the calculation the stress field near the crack tip using the linear elastic theory that will covered in more detail in this section.

3.2.2. Energy Balance Criterion

In 1920, Griffith suggested that a crack can only grow when the applied energy is sufficient to overcome the resistance of the material to form new surfaces. The resistance of the material includes surface energy effects, elastic strain energy, and plastic work that dissipates energy by inelastically deforming the materials near the crack tip. He defined that the total system energy (E, Eq. 3-1) is the sum of work (W_s) needed to create new surfaces and potential energy (Π) including strain energy and external work (W_s) done by the boundary loading [130].

$$E = W_s + \Pi \tag{3 - 1}$$

Since the crack extension for fracture occurs under equilibrium conditions with no net change in total energy, Eq. 3-1 can be modified as Eq. 3-2 for an incremental increase in the crack area (dA).

$$\frac{dE}{dA} = \frac{dW_s}{dA} + \frac{d\Pi}{dA} = 0 \tag{3 - 2}$$

After Griffith's approach defining the critical conditions for the fracture, Irwin proposed an energy approach that is equivalent to Griffith model [131, 132]. In this work, Irwin defined the energy release rate (G) that is the amount of the available energy required to cause the further crack extension (Eq. 3-3).

$$-\frac{d\Pi}{dA} = \frac{dW_s}{dA} = G \tag{3 - 3}$$

Thus, from this crack extension model, the fracture can be considered in an energy approach because the fracture is initiated when the crack driving force (G) is greater than the critical energy release rate (G_c) which is also a measure of fracture toughness as described in Eq. (3-4).

$$G \geq G_c \tag{3 - 4}$$

3.2.3. Stress Intensity Approach

As another way to look at the fracture, Irwin [133] and William [134] described the stress field surrounding a crack using a polar coordinate axis at near the crack tip (Fig. 3-1) by assuming isotropic linear elastic materials behavior (Eq. 3-5).

$$\sigma_{ij} = \left(\frac{k}{\sqrt{r}}\right) f_{ij}(\theta) + \sum_{m=0}^{\infty} A_m r^{\frac{m}{2}} g_{ij}^{(m)}(\theta) \tag{3 - 5}$$

where σ_{ij} and k indicate stress tensor and constant, respectively, while f_{ij} is dimensionless function of θ. A_m and $g_{ij}^{(m)}$ are the amplitude and a dimensionless function of θ for the mth term which depend on geometry. However, in any given geometries, the stress field

at the crack tip ($r = 0$) contains a stress singularity with the term ($1/\sqrt{r}$) in a crack body, as shown in Fig. 3.1. In contrast to the energy balance criterion that does not differentiate the loading direction, the stress intensity approach using the stress field (Eq. 3-5) describes three different modes of a crack depending on the symmetry of the field around the crack tip such as Mode I, II, and III as shown in Fig. 3.2.

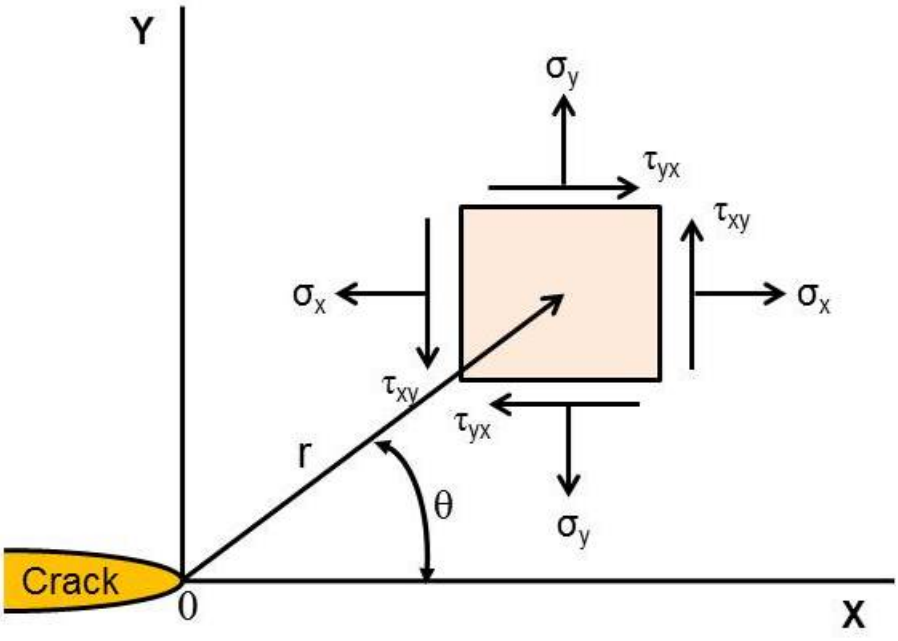

Figure 3.1. Coordinate axis for describing the stress field at the crack tip while z indicates the normal direction to the page.

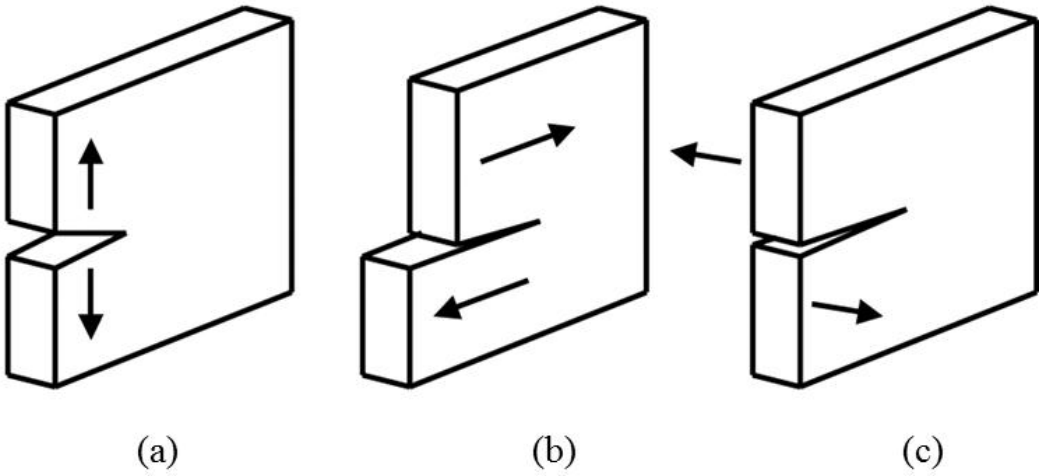

Figure 3.2. Modes of a fracture: (a) mode I (tensile opening mode), (b) mode II (in-plain sliding mode), and (c) mode III (out of plane tearing mode) (http://jeb.biologists.org/content/210/13/2213/F3.expansion.html).

While each stress component has the stress singularity, the stress components also have the proportionality constants (k and f_{ij}) which are combined to define the stress intensity factor (K). By having the definition of the stress intensity factor (K), it becomes possible to describe all components of stress, strain and displacement as a function of r and θ in the crack body under different fracture modes while the stress intensity factor defines the amplitude of the crack tip singularity that is proportional to the stresses near the crack tip. Therefore, if there is a local failure at the crack tip when the stress intensity factor known, it is possible to determine the critical stress intensity (K_c) at which failure will occur which is an alternate measure for the fracture toughness similar to G_c. In addition, G_c and K_c can be related through Eq. 3-6 in linear elastic materials [133]. Thus, if one parameter (G_c or K_c) is known, another fracture parameter can be calculated from Eq. 3-6 [133].

$$G = \frac{K^2}{E} \tag{3 - 6}$$

If the system undergoes mixed loading mode, the individual stress contributions are added to given the stress component using the principle of linear superposition (Eq. 3-7).

$$\sigma_{ij}^{total} = \sigma_{ij}^{(I)} + \sigma_{ij}^{(II)} + \sigma_{ij}^{(III)} \tag{3 - 7}$$

3.2.4. Crack Tip Plasticity

Linear elastic fracture mechanics (LEFM) predicts an infinite stress at the sharp crack tip (r = 0, Eq. 3-5) since materials cannot support an infinite stress. In real materials, stress relaxation occurs near the crack tip. In order to modify the stress behavior at the elastic region, two approaches are developed to account for moderate crack tip yielding by Irwin (Eq. 3-8) [135, 136] and Dugdale (Eq. 3-9) [137] while Irwin uses the elastic stress analysis to estimate the size of the plasticity effect and Dugdale uses the strip yield model.

$$r_p = \frac{1}{2\pi}\left(\frac{K_c}{\sigma_{ys}}\right)^2 \tag{3 - 8}$$

$$r_c = \frac{1}{8}\left(\frac{K_c}{\sigma_{ys}}\right)^2 \tag{3 - 9}$$

In Eq. 3-8 and Eq. 3-9 r_p and r_c are the plastic zone sizes calculated by Irwin's and Dugdale's approach and σ_{ys} indicates the yield strength of the material. However, if the inelastic material deformation is extensive yielding at the crack tip, elastic plastic fracture mechanics must be considered. Overall, the larger plastic zone size predicted by Eq. 3-8 and 3-9 will eventually play a role to increase the fracture toughness by relaxing the crack tip stress and dissipating energy that otherwise would be available for fracturing the interface.

3.2.5. Interfacial Fracture

Until now, crack tip behavior in homogeneous bulk materials was only discussed which is slightly different from a crack on an interface when two thin films are in contact as shown in Fig. 3.3. The interface composed of two different materials can encounter mix mode loading [138], as shown in Fig. 3.2. In the bulk materials, when the driving force (G) is greater than the critical value (G_c) at the crack tip, the crack can select its propagation path along the interface or out of the plane of the interface [137]. However, the interface between dissimilar materials subject to loading conditions mode I, mode II, and mode I+II only allows the interfacial failure due to the weak strength of the interface [139]. Thus, we can still apply the failure criterion that was discussed for bulk materials in previous section. Therefore, the energy release rate approach is still used to predict the interfacial failure at the contact, as shown in Fig. 3.3.

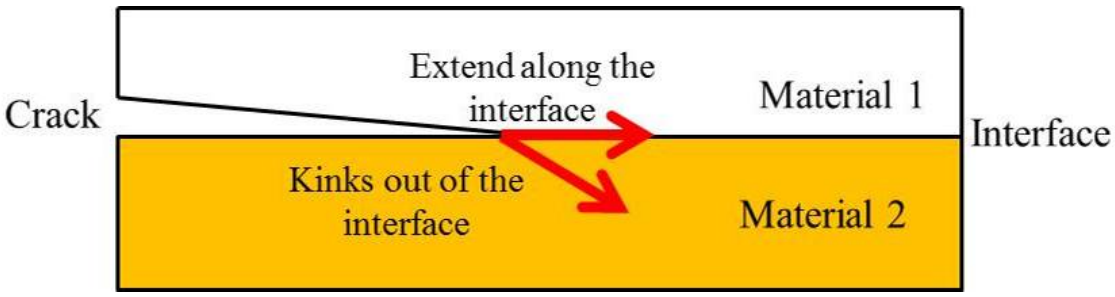

Figure 3.3. Crack path selection at the interface when dissimilar materials are in contact.

When the energy balance criterion with G_c is used to analyze the failure mode at the interface under the mixed loading conditions, the phase angle (ψ), which is the relative amount of mode II to mode I, should be considered due to the dependency of the fracture energy on the phase angle (ψ) [140]. The elastic mismatch in two different thin films creates this strong dependence as already shown by Snodgrass *et al.* [141], (Fig. 3.4). The increase in G_c at a higher phase angle (ψ) results from the plastic energy dissipation in the polymer layer that is more sensitive to mode II (shearing) and the frictional effect of fracture surface asperities [140-142].

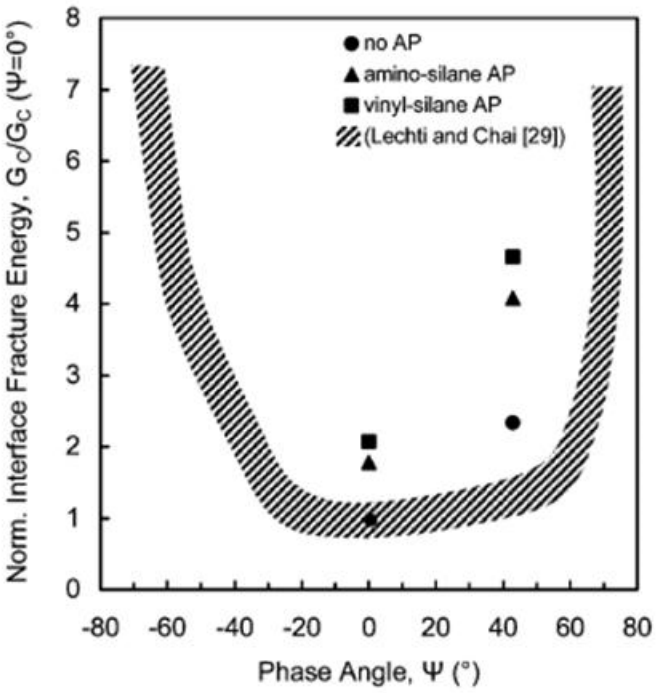

Figure 3.4. Example of fracture energy dependence on the mode mixity on a polymer material (benzocyclobuene: BCB)/SiO_x interface using adhesion promoters while hatched region show previous mode mixity from Lechi and Chai [140] with glass/epoxy interface [141].

3.3. Definition of Adhesive and Cohesive Strength

The interfacial fracture toughness (critical strain energy release rate: G_c, J/m^2) is the energy required to create new surfaces [143]. The interfacial fracture toughness is considered the macroscopic work of fracture per unit area [G_c, J/m^2] which is different from the work of adhesion [138, 144]. This separation work is determined by two different energy absorbing processes such as the near-tip work of fracture (G_o) and energy dissipation (G_{zone}) in a zone surrounding the crack, as shown in Fig. 3.5. Since G_c depends on the interface chemistry, adjacent material, its elastic-plastic constitutive behavior, loading mode mixity, interface morphology (roughness), and film thickness

[144-147], special care is needed to determine the interfacial adhesion strength. The cohesive fracture energy strength is the energy needed to cause fracture within the bulk layer [148, 149] while the adhesive fracture energy strength is the maximum energy required to cause failure at the interface.

From the measured interfacial adhesion or cohesive strengths (G_c), the failure criteria for the interface or bulk can be provided for modeling the mechanical response of the device. In addition to measuring the baseline strength values, understanding of environmental effects on the adhesion is also important because chemical modification of the interface can easily change the deformation process. Due to the early failure from mechanical stress, temperature, environmental species, and photochemical reactions [141, 147, 150-153], the subcritical crack growth is also an important quantity that must be understood in order to predict the mechanical reliability of devices susceptible to failure by fracture.

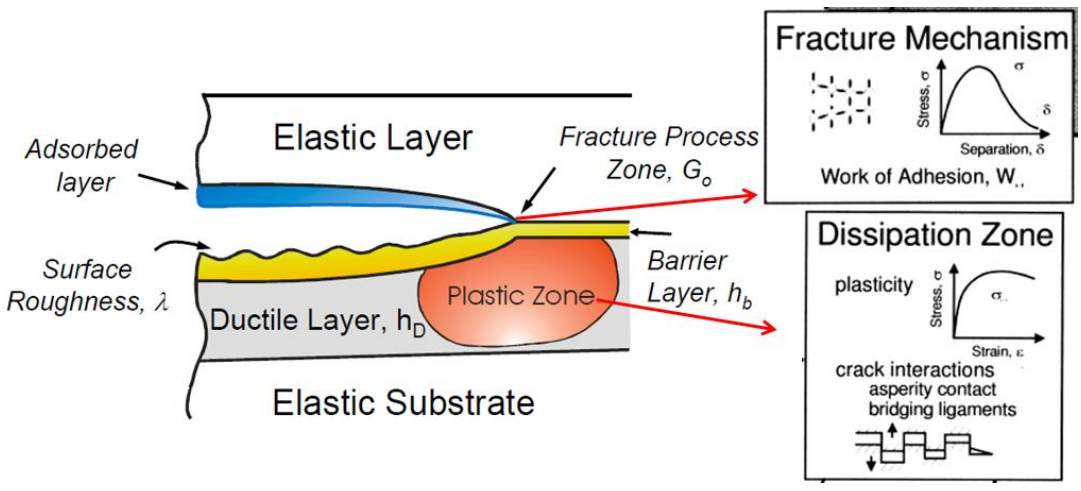

Figure 3.5. Schematic representation for near-tip fracture mechanisms and the wake dissipation zone behind the crack tip [138, 154].

3.4. Mechanism of Adhesion

When two different materials are in contact, the mechanism of the adhesion can be explained by five categories which include mechanical bonding (interlocking), primary bonding (chemisorption), secondary bonding (physisorption), electrostatic bonding and diffusive bonding [155, 156]. Firstly, the mechanical adhesion is a key intrinsic adhesion while the adhesive penetrates into the holes, crevices, pore, and other irregularities of the surface on the substrate that mechanically lock the adhesive to the substrate. By holding two different materials using mechanical interlocking, as shown in Fig. 3.6, the interfacial friction at the contact area causes a higher interfacial energy dissipation effect which greatly enhances the total adhesion strength by requiring higher interfacial shear stress to break the interface [157]. In addition, the localized deformation of asperities also introduces more wake dissipation energy effect behind the crack tip that also improves the adhesion strength [152]. Since the mechanical adhesion can be significantly affected by the contact area between two materials, properties such as surface roughness play an important role in the adhesion strength [138, 152].

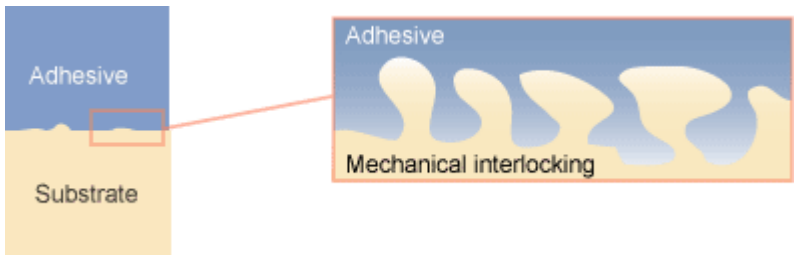

Figure 3.6. Representation of interface formed by mechanical interlocking (http://www.specialchem4adhesives.com/resources/adhesionguide/index.aspx?id=theory4).

The next adhesion mechanism is through primary interatomic bonds which occur when atoms of two different materials undergo ionic bonding, covalent bonding, and metallic bonding [158]. Ionic bonding is normally found where the materials are composed of both metallic and nonmetallic element. In general, valence electrons are provided from the atoms of a metallic element to the nonmetallic atoms which make all atoms ions [159]. As a typical example of the ionic bonding, Fig. 3.7(a) shows how sodium (Na) and chlorine (Cl) become ions by transferring its electron from Na to a Cl atom that starts from sodium chloride (NaCl). Covalent bonding is the chemical bond that is formed by sharing pairs of electrons between any atoms. Unlike the ionic boning case that is created by transferring electrons, the covalent bond leads to a stable electronic configuration through the electron sharing mechanism. This mechanism can be easily explained using a molecule of methane (CH_4), as shown in Fig. 3.7(b), where the carbon and the hydrogen share its electrons. Lastly, metallic bonding is created through the electrostatic attractive forces in metals when free electrons form a sea of electrons, as shown in Fig. 3.7(c), while ion cores show positively charged characteristic. In the metal, the free electrons non-directionally hold the positively charged ion cores by preventing the ion cores from repulsing each other. More importantly, ionic, covalent, metallic bonds do not only exist in a pure mode, but they can exist in a mixed mode [159]. Overall, such primary bonding shows higher adhesion strength compared to the secondary bonding which is only formed by weak van der Waals forces which create the secondary boding.

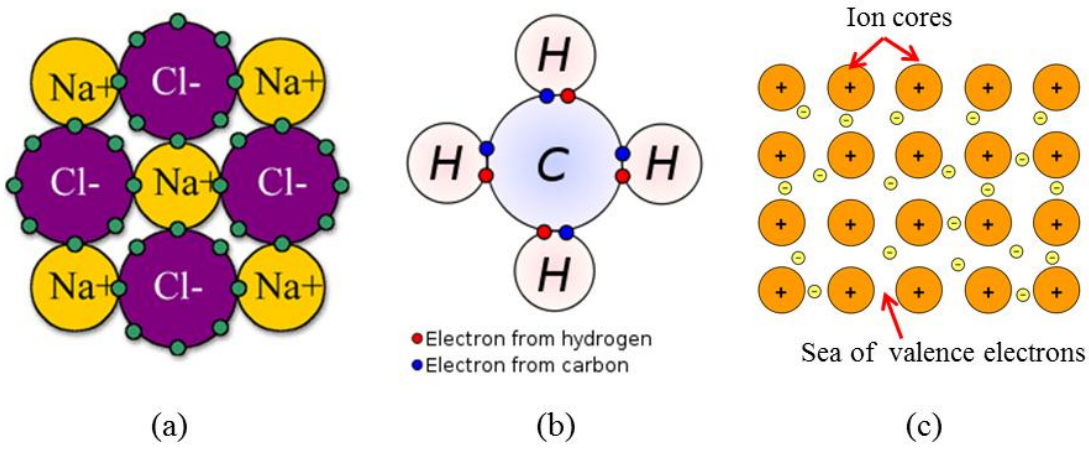

Figure 3.7. Typical examples of primary interaction bonds for: (a) ionic bonding using sodium chloride (NaCl) (http://textbooks.elsevier.com/manualsprotectedtextbooks/9780750663809/Static/bonding/bonding2c.htm), (b) covalent bonding using a molecule of methane (CH_4) (http://www.answers.com/topic/covalent-bond), and (c) metallic boning using sea of valence electrons and positively charged ion cores (http://commons.wikimedia.org/wiki/File:Metallic_bonding.svg).

Secondary bonding is primarily due to van der Waals forces which are the sum of attractive and repulsive forces between molecules [156, 160]. The secondary bonds by the van der Waals forces are divided into three components including Keesom force (force between two permanent dipoles), Debye force (force between a permanent dipole and a corresponding induced dipole), and London dispersion force (force between two instantaneously induced dipoles) [156]. Keesom interactions are electrostatic interactions between permanent dipoles in molecules which are shown in Fig. 3.8(a) with hydrogen chloride (HCl) where the positive end of HCl attract the negative end of HCl and Debye interactions are attractive interactions between a permanent dipole molecule (Ar in Fig. 3.8(b)) and a induced dipole (HCl in Fig. 3.8(b)) while Debye interactions are expected between any polar and nonpolar molecules [156, 160]. In addition, London dispersion interactions exist between any possible molecules which are caused by an instantaneous

dipole moment as its electrons fluctuate instantaneously [156], as shown in Fig. 3.8(c). In this dissertation, three intermolecular forces were evaluated by measuring the contact angles on surfaces that are transformed into surface energy with polar and dispersive components. Thus, the permanent dipole-dipole interactions (Keesom and Debye forces) are accessed by the polar component of the surface energy and the instantaneously induced dipole-dipole interaction (London dispersion force) is interpreted by the dispersive component of the surface energy.

As the fourth mechanism, electrostatic adhesion can also be formed in conducting materials when there is electron transfer across the interface creating an attractive force that imposes the resistance to separation at the interface. Lastly, when two different materials are brought into contact, as shown in Fig. 3.9, diffusion theory attributes the bonding mechanism of the polymers to the inter-diffusion at the interface while contact time, contact temperature, polarity of adhesive, phase state of the polymeric materials, and molecular weight of materials, etc. significantly affect the diffusion process[161, 162].

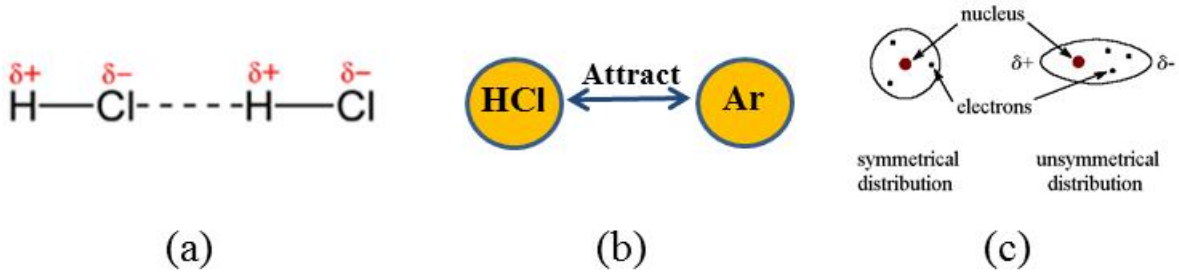

Figure 3.8. Typical examples of intermolecular interactions by: (a) Keesom force, (b) Debye force, and (c) London dispersion force.

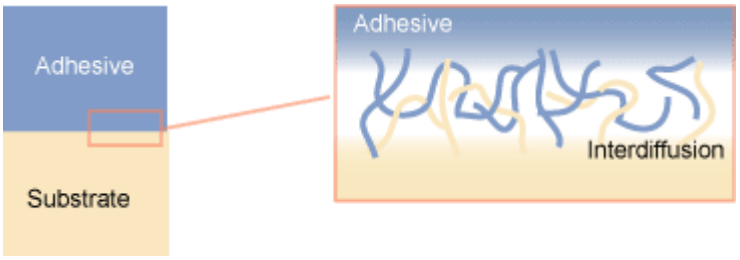

Figure 3.9. Schematic diagram of diffusion bonding through the interdiffusion when one material is brought into contact to the substrate (http://www.specialchem4adhesives.com/resources/adhesionguide/index.aspx?id=theory5).

3.5. Adhesion Promotion at the Interface

In order to modify the adhesion strength at the interface using chemical treatments, silane coupling agents have been as a molecular bonding agent to promote secondary and primary bonding at interfaces [152, 163]. In a general sense, silane promoters consist of an organo functional tail group and hydrolyzable group, as shown in Fig. 3.10. When the silane promoters are applied on the substrate, the silane is first hydrolyzed to form a silanol and it condenses and polymerizes with itself to create its network while the functional tail groups can be chosen for the specific applications [164], as shown in Fig. 3.10. Thus, by choosing the specific tail groups of the silane coupling agents, the adhesion strength can be chemically modified. In addition to selecting the proper tail group, it is also very important to check the effectiveness of the silane coupling agents which depend on the substrate while smooth and hydrophilic surfaces are better than hydrophobic and discontinuous substrate [164]. Since silane coupling agents are commercially available, it has been already shown to improve the adhesion strength by

forming strong bonds at the interfaces between oxides and PMMA by forming metal/silane and silane/PMMA covalent bonds [152].

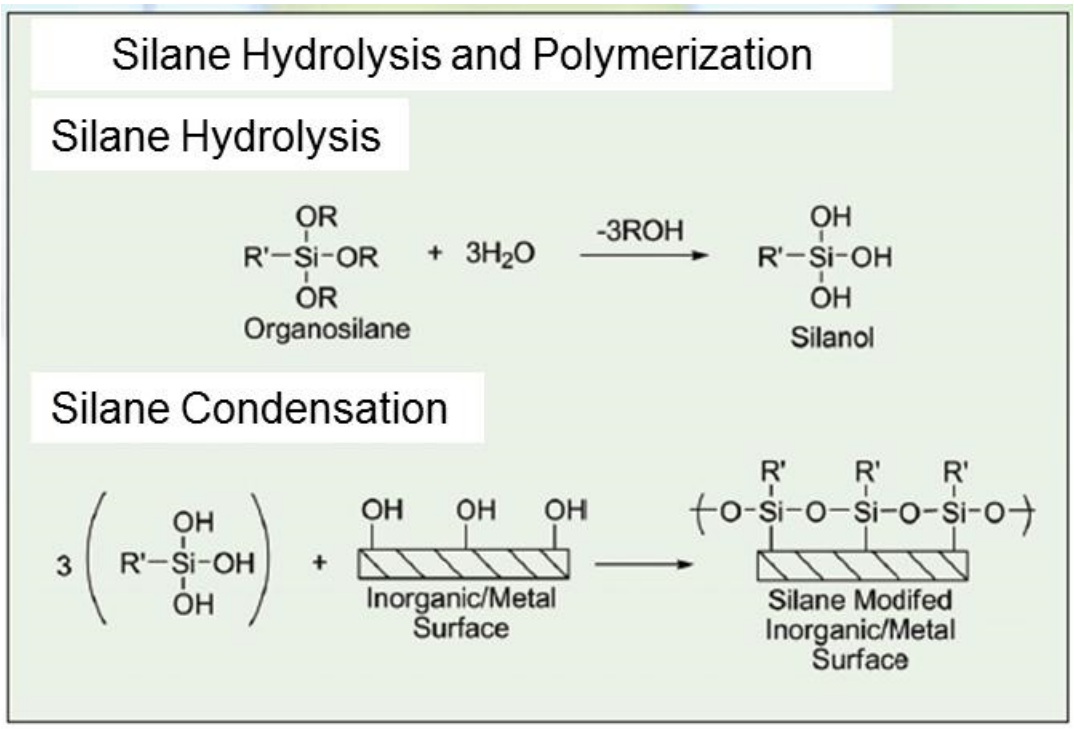

Figure 3.10. Descriptions for silane hydrolysis and silanol condensation [164].

However, silanes have several disadvantages that need to be overcome such as difficulty of forming a monolayer due to homocondensation [165] and low air stability (need to store in anhydrous conditions during deposition) [165, 166]. Another adhesion promotion method which addresses these issues is the use of phosphonic acids (PAs) as adhesion promoters. PAs share similar advantages with the silane modification, but unlike silanes, PAs have up to three covalent bonds that can form when bonding to an inorganic surface providing a very robust and thermally stable bond (Fig. 3.11). Phosphonic acids also form a monolayer coating much easier because the bonding reactions do not occur so rapidly under mild conditions [167]. The PAs are also

independent of the amount of water during the reactions indicating less stringent processing conditions compared to the sliane modification process [166] and it is air-stable. Therefore, PA solutions can be stored in normal laboratory conditions without rapid degradation. Additionally, PA also provides more robust and stable bonds compared to organosilanes [152, 167, 168]. Finally, the functional tail group on the PA can also be tailored to react with the polymer layer in order to provide covalent or not covalent bonding, as desired. While PAs present some distinct features that can improve the adhesion strength at the interface of inorganic and polymer surfaces, very little has been done to investigate and exploit these properties for improving adhesion in OPV devices.

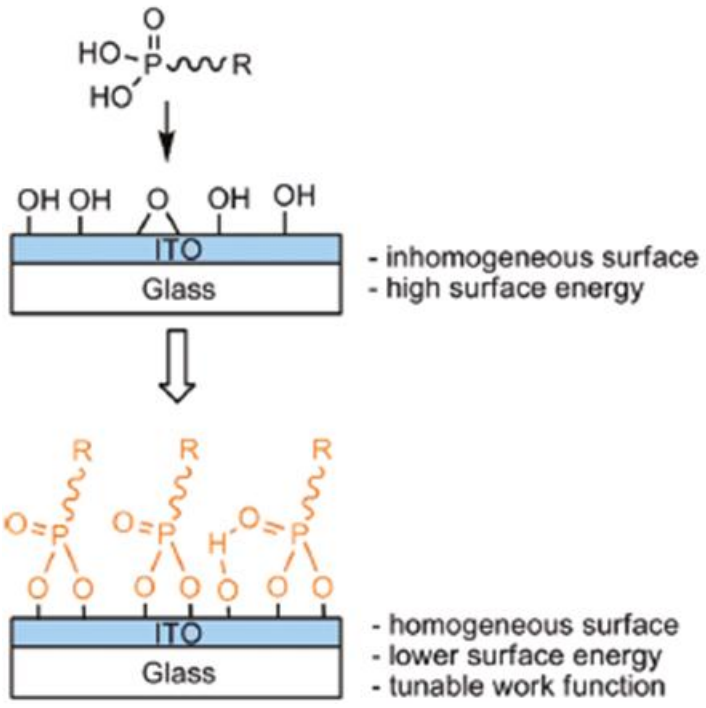

Figure 3.11. Description for phosphonic acid attachment on ITO film [169].

For the organic/organic interface, strong intermixing at the interface between the layers promoted by thermal annealing can result in improved adhesion. It was shown for a P3HT:PCBM BHJ and PEDOT:PSS interface, annealing created the formation of a $P3HT^{+}$:PSS^{-} interface layer which ultimately enhanced the adhesion strength from 1.5 J/m^2 to 5 J/m^2 [67]. Without thermally annealing the structure, it is also possible to enhance the adhesion strength by replacing the contact material, as already shown in Fig. 2.20(b). In this study, the weak adhesion between the BHJ and PEDOT:PSS was improved by replacing the conductive polymer PEDOT:PSS with a metal oxide V_2O_5 which forms an intermixed layer from the formation of chemical bonds including covalent, ionic and bipolar interactions [11]. In addition, the adhesion enhancement at the interface can also be improved by having more contact area between two materials resulted from the mechanical interlocking effect, as already explained in section 3.4 [152].

Van der Waals forces are another key factor that needs to be understood when two materials are in contact. As previously mentioned, it has two different energy components which are polar and dispersive components of the surface energy. While most of the studies showed that the polar component in van der Waals forces greatly increases the interfacial adhesion strength, Aradhya *et al.* recently reported that the contribution from the dispersion force can also increases the interfacial breaking force for the high conductance configuration between organic and inorganic materials where the high conductance configuration indicates that the electrode separation is smaller than the length of the molecule [170]. However, since it was done in a single molecular level, it is necessary to match the theoretical treatment of van der Waals interactions at organic/inorganic interface with the region in a comparable high magnitude.

As a more common method to enhance the interfacial adhesion strength, an O_2 plasma treatment technique is most widely used to maximize and to optimize the polar component of van der Waals force on the surface [169, 171-176]. The O_2 plasma treatment is useful to make the inorganic surface hydrophilic without changing the bulk material properties [172]. The changing surface property from hydrophobic to hydrophilic conditions results from removing organic surface contamination and chemically modifying the surface to oxygen rich states while it can also physically etch the surface to make the surface rougher [174, 175]. The carbon contamination reduction can be explained from the model of an oxide covered metal, as proposed by McCafferty *et al.* using variable-angle XPS study [173], as shown in Fig. 3.12. In his approach, the oxide metal model consists of organic carbon overlayer (t_c) and oxide film (d) which includes chemisorbed water (t_{H2O}), hydroxylated region (t_{hydrox}), and the inner most portion of the oxide film (t_{MO}) (Fig. 3.12) [173]. Thus, when the metal surface is O_2 plasma treated causing the complex reactions of free radicals [177], the top most organic carbon layer is removed which will eventually make the surface very hydrophilic and this hydrophilic condition corresponds to high polar component of the surface energy. Thus, while it has been just suggested to use the O_2 plasma cleaning process to enhance the adhesion strength by making the surface very hydrophilic [169, 171-176], this study will provide a comprehensive quantitative data with and without the O_2 plasma treatment relating to the polar component of the surface energy.

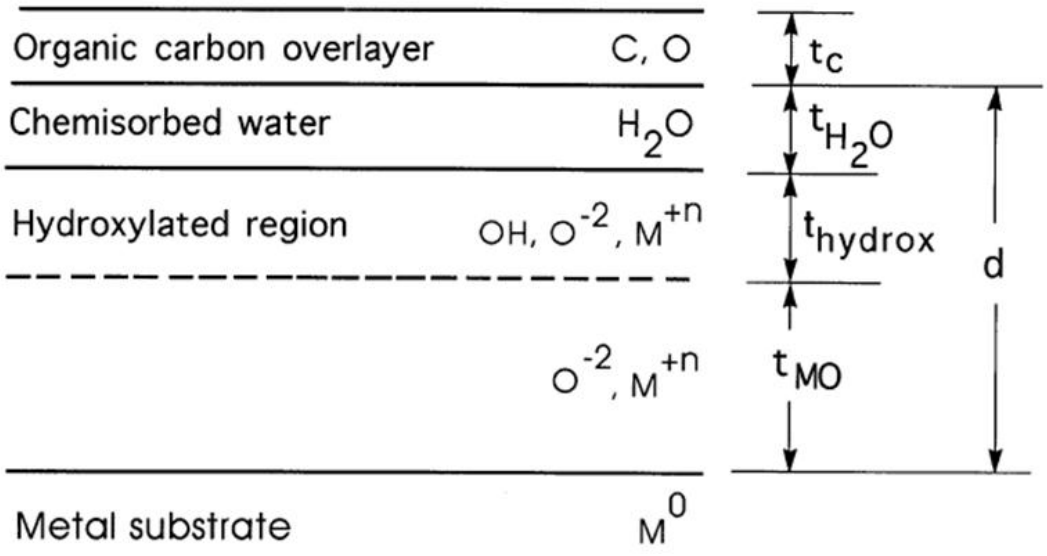

Figure 3.12. Proposed model for an oxide covered metal with possible layer and compositions [173].

In addition to O_2 plasma treatment, Terriza *et al.* suggested that the oxide surface (TiO_x) can be exposed under UV illumination which will also remove the carbon contaminations (Fig. 3.13) to make the surface super hydrophilic giving a potential for enhancing the adhesion strength with other contact materials [178].

3.6. Adhesion Strength Measurement Techniques

3.6.1. Common Adhesion Testing Methods

Over the years, many techniques have been developed to measure the interfacial fracture toughness with indentation method, peeling test, blistering method, and fragmentation method. While more measurement techniques exist with various approaches and assumptions, those widely used methods are briefly reviewed in this

dissertation. The indentation technique simply requires a bilayer sample deposited on a flat planar sample. This method does not require any additional sample preparation that allows for measuring the initial interfacial fracture toughness of virgin samples after the film fabrication [138, 179], as shown in Fig. 3.13(a), and a typical load vs. displacement response is indicated in Fig. 3.13(b). However, since this technique requires three parameters that can cause uncertainty such as residual stress of films, indentation depth for calculating the indentation stress, and diameter of the resultant delamination, it usually leads to qualitative results due to its complicated behavior [138, 144]. To modify this technique for measuring the adhesion strength of the nanoscale films, a very sharp (nanoscale) indenter tip was developed to create radial cracks to avoid overloading issues from the blunt indenting tip (microscale tip) during the tests [179-182]. Fig. 3.14(a) shows typical radial cracks of bulk films created by the sharp nanoscale indenter tip and Fig. 3.14 (b) indicates fracture toughness values of bulk SiC at various loading conditions. However, when the films are thinner than 100 nm, this technique cannot be applied to measure mechanical properties. This is because before creating the radial cracks on the top surface, the nanoscale indenting tip touches the bottom substrate which makes it impossible to remove substrate effects when calculating the fracture toughness of the thin films.

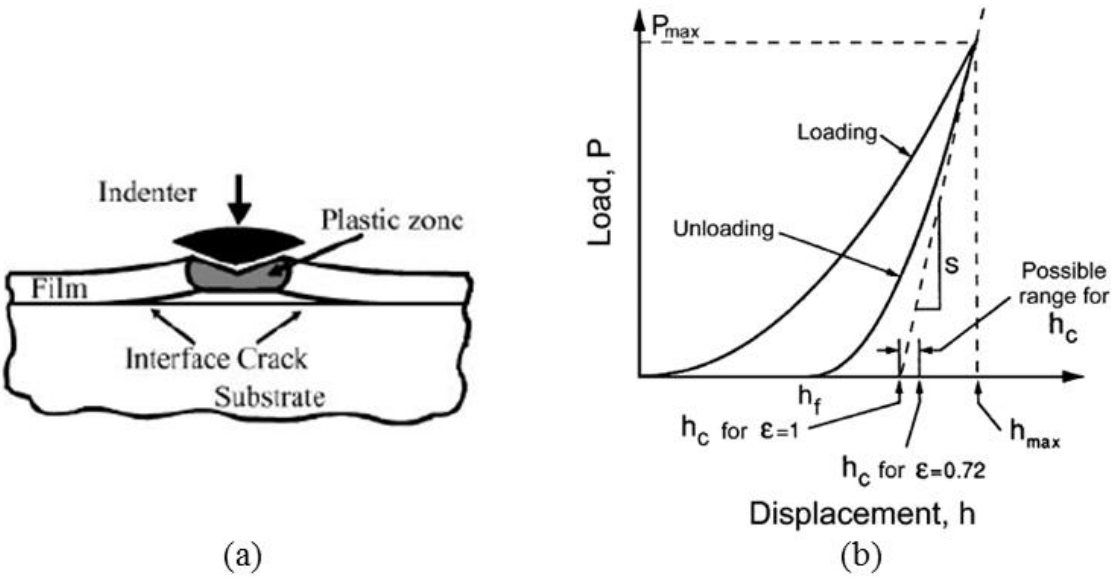

Figure 3.13. (a) Schematic representation of the indentation test [138] and (b) typical load vs. displacement response after the indentation test (P_{max} is the peak load; h_{max} is the displacement at the peak load: h_c is the contact depth; h_f: is the final displacement; S is the contact stiffness) [183].

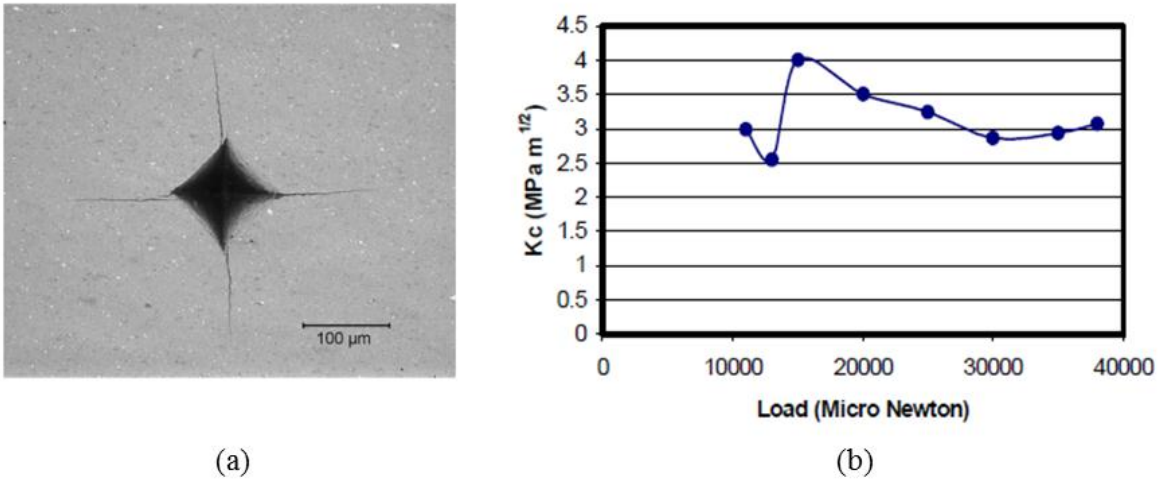

Figure 3.14. (a) Radical cracks of a NIST Standard Reference Material 2100 test piece created by a 98 N Vickers indentation [184] and (b) fracture toughness of the bulk SiC as a function of indentation load [185].

The peeling test is also a well-known technique to measure the adhesion strength of thin films as shown in Fig. 3.15(a). However, the measured G_c from the peeling test includes the forces and moments transmitted to the thin films during the test that are also difficult to separate [144, 186, 187]. So, this test also provides only qualitative results. In order to improve the measurement system of the peeling tests, Bagchi *et al.* first suggested a utilization of a highly stressed super-layer to apply the driving energy for the delamination propagation [138, 144] and it was again modified by Sitaraman *et al*. with a fixtureless super-layer-driven delamination test [188-190], as shown in Fig. 3.15(b). The blistering method [191, 192] has been very successful to measure the adhesion strength, as shown in Fig. 3.16. However, this technique requires many complicated sample preparation steps to create the cavity impacts data measurements in most of the cases.

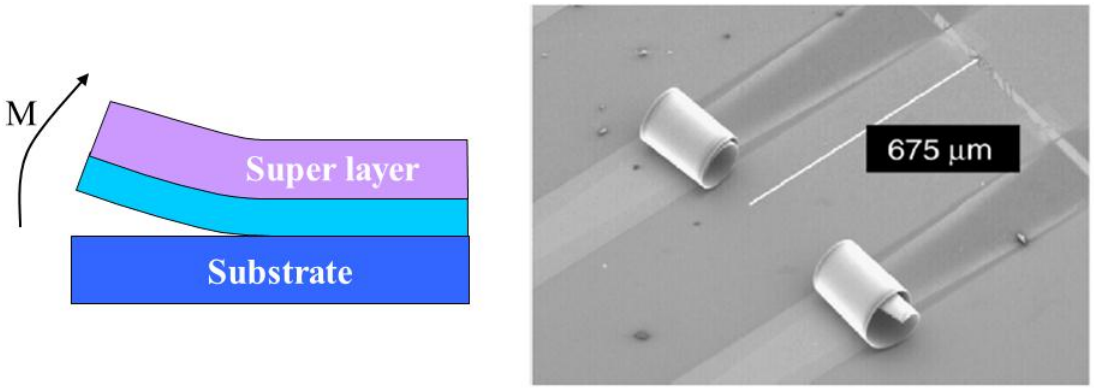

Figure 3.15. (a) Delamination of the thin-film (peeling test) and (b) SEM image of delaminated strips using a fixtureless super-layer-driven delamination test method [188].

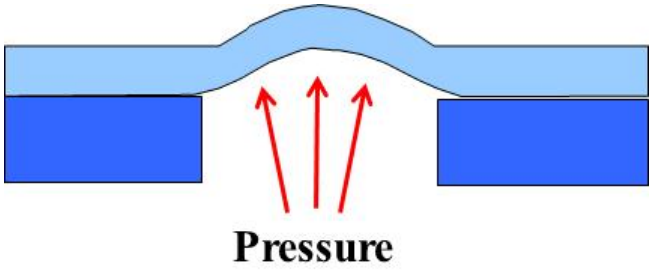

Figure 3.16. Blister method for measuring thin film adhesion strength.

Overall, the indentation, peeling, and blistering methods show fairly good performance to determine the adhesion strength in some applications with mostly providing the qualitative results. However, those techniques do not have a capability to separate the residual stress level whose effect can be very large [192].

The fragmentation method has been widely used to predict constant interfacial shear strength (IFSS) at the interface between the polymeric substrate and ITO (Fig. 2.15) while the experimental geometry of the fragmentation test allows for the control of the stress state during tension test due to the absence of the third body interactions [63, 106, 107]. By defining three crack stages (random cracking, mid-point cracking and initiation of transverse buckling, Fig. 2.15(a)), the expression for the constant interfacial shear strength (IFSS) under uniaxial tension is calculated using Eq. 3-10 from the fragmentation [63].

$$\tau = 2h_c\sigma_{\max}(l_c)/l_c \qquad (3 - 10)$$

where τ and σ_{max} represent the constant IFSS and the size dependent tensile strength related to the failure stain, respectively, and h_c and l_c indicate coating thickness and the critical stress transfer length which is defined when the maximum coating stress (σ_{max}) is

achieved, respectively [64, 108]. The tensile strength (σ_{max}) is defined using Weibull weakest-link model which can account for the internal stress of the brittle materials [108]. However, it is hard to derive the reasonable internal stress for the nano-size films due to limited experimental data available in the required strain range.

Accordingly, a standard adhesion strength measurement technique is needed to evaluate the interfacial fracture toughness of thin films in the OPV devices including the barriers. As a result, in this study, we will utilize a four point bending (FPB) and double cantilever beam (BCD) techniques, as standard methods, to provide the quantitative adhesive/cohesive strength in the OPV devices.

3.6.2. Four Point Bending (FPB) Technique

As already pointed out, since the indentation, peeling, and blistering methods have limited capability to measure the interfacial fracture toughness of thin films, the four point bending (FPB) and double cantilever beam (DCB) techniques are adopted in this dissertation while those methods are also accepted as standard adhesion testing methods in many fields [11, 67, 138, 141, 144, 193, 194].

In order to come up with an analytical solution for calculating the interfacial fracture toughness (G_c) using the four point bending (FPB) technique, Charalambides's approach was utilized in this study [195] while this approach has been widely used for the interfaces involving nanoscale thin films [138, 144, 193, 194].

From beam theory, the cracked ligament in the four point bending samples should be subject to constant moment conditions when an interfacial crack exists between the inner loading lines, as shown in Fig. 3.17(a). As also previously stated by Drory *et al.* and Thouless *et al*., when the length of the interfacial crack during the FPB tests is significantly longer than the thickness of the upper layer of the substrate, the interfacial fracture toughness exhibits steady-state characteristics [196, 197]. Therefore, the G_c can be analytically calculated by taking the difference in the strain energy between the uncracked and cracked FPB beam [195, 198]. However, the strain energy in the beam above the crack can be negligible, the G_c can be finally formed by only considering the strain energies in the uncraked beam and of the lower beam under the interfacial crack [195, 198]. From elastic beam theory and plane strain conditions, the strain energy takes the form in Eq.3-11,

$$U_o = (1-\upsilon^2)\frac{M_o^2}{2EI_o} \tag{3 - 11}$$

where U_o is the strain energy per unit cross section and I is the second moment of area per unit width. Therefore, G_c takes the form in Eq. 3-12,

$$G_c = \frac{M_o^2(1-\upsilon^2)}{E}(\frac{1}{I}-\frac{1}{I_c}) \tag{3 - 12}$$

where c refers to the section of the lower beam beneath the crack. From the beam theory and Charalambides's approach, I and I_c become:

$$I_c = \frac{2}{3}h^3 \tag{3 - 13}$$

$$I = \frac{1}{12}h^3 \tag{3 - 14}$$

By taking into account for Eq. 3-11 through Eq. 3-14, G_c and the moment M can be determined from Eq. 3-15,

$$G_c = \frac{21M_o^2(1-\upsilon^2)}{4h^3E} \quad \text{while } M = \frac{PL}{2b} \tag{3 - 15}$$

As a result, in the four point bending (FPB) technique, the interfacial fracture toughness (G_c) at the interface is found by Eq. 3-16,

$$G_c = \frac{21(1-\nu^2)P_c^2L^2}{16Eb^2h^3} \tag{3 - 16}$$

where ν and E represent Poison's ratio and Young's modulus of the Si substrate. As the geometric parameters of the test sample, as shown in Fig 3.17(a), such as distance between inner and outer pins (L), width of the beam (b), and thickness of the half height of beam (h) are used to calculate the interfacial fracture toughness. Thus, only the critical

force (P_c) needs to be measured from the tests. When loading the FPB samples, the load versus deformation becomes constant which is used to determine P_c (Fig. 3.17(b)) which is then converted to the G_c using Eq. 3-16. The calculated G_c represents the steady state interfacial fracture toughness subjected to a constant moment condition while the interface crack length (a) is very long compared to the substrate thickness, as already mentioned [195, 198]. So, the G_c becomes independent of interface crack length (a) [194, 199, 200]. This is why the four point bending technique is widely accepted as a standard adhesion measurement method.

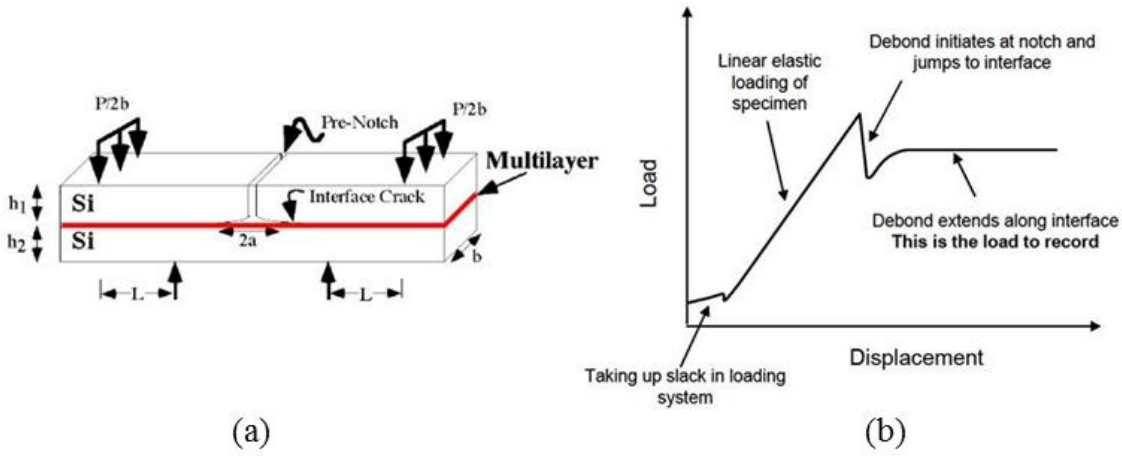

Figure 3.17. Schematic diagrams of: (a) four point bending (FPB) sample and (b) general load vs. displacement curve for FPB tests [154].

Since the FBP technique has a mixed fracture mode with tension (I) and shear (Π), the measured G_c is higher than the values from the double cantilever beam (DCB) method due to higher friction effect at the interface. To be capable of measuring the adhesion strength with this technique, a delicate loading system including load cell and actuator is required to obtain the high resolution load vs. displacement curve. In this work, the loading rate is fixed at 0.5 μm/sec while all tests were carried out at room temperature conditions.

As previously mentioned in section 3.2.3, since the interfacial fracture toughness (G_c) depends on a phase angle which defines the relative amount of mode I to mode II in FPB tests, it is required to calculate the local phase angle at the crack tip (ψ) to define the mixed mode loading condition at the model interface. The phase angle can be calculated using Eq. 3-17 below [141, 151].

$$\psi = \psi_\infty + \omega + \varepsilon \ln(l/h) \tag{3 - 17}$$

when ψ_∞ indicates the far-field applied phase angle ($\psi_\infty \approx 41°$) calculated by Eq. 3-18 [201] where K_I and K_{II} represent the stress intensity factor that are used to predict the stress state near the crack tip caused by a remote load in facture mechanics.

$$\psi_\infty = \tan^{-1}\left(\frac{K_{II}}{K_I}\right) \approx 41° \tag{3 - 18}$$

As the second parameter, ω is defined using Dundur's parameters (α and β) which are the measures of the elastic property mismatch at the interface [139, 195, 202]. The third parameter (ε) indicates the biomaterial constant defined by Eq. 3-19 [201],

$$\varepsilon = \frac{1}{2\pi}\ln\left[\frac{(3-4\nu_1)/\mu_1 + 1/\mu_1}{(3-4\nu_2)/\mu_2 + 1/\mu_2}\right] \tag{3 - 19}$$

where ν and μ are Poison's ratio and shear modulus, respectively, and l is an arbitrary length scale representing a microstructural dimensions of the plastic zone in the model interface while h is taken to the half of the beam height [153]. Therefore, by considering all of the parameters introduced above, the local phase angle (ψ) is fixed at 43° in this dissertation.

3.6.3. Double Cantilever Beam (DCB) Technique

As another standard method, the double cantilever beam (DCB) technique was also used in this study. Unlike the FPB test for the barrier applications, the DCB method was used to determine the adhesive or cohesive failure of interfaces or layers in inverted organic photovoltaic devices.

The general equation for calculating the interfacial fracture toughness using the DCB technique is very straight forward which uses beam theory by considering the sample geometry, as shown in Fig. 3.18(a). From LEFM, it is assumed that the material is linearly elastic and isotropic [143]. In addition, an interfacial crack is initiated and propagates along the interface while the plastic zone near the crack tip is very small [143]. In this case, Eq. 3.20 gives the general expression for the interfacial fracture toughness (G_c, J/m^2).

$$G_c = \frac{P^2}{2b}\frac{dc}{da} \tag{3 - 20}$$

where P represents the load and c and a are the compliance of the beam ($c = u/P$, u = displacement in Fig. 3.18(a)) and the crack length, respectively, during the DCB tests while b is the width of the beam. Using beam theory, Eq. 3-20 can be written in another

form (Eq. 3-21) by using material properties (ν and E) and geometrical parameters (b and h). Therefore, the general equation for calculating the critical energy release rate in the double cantilever beam (DCB) technique is given by [203]:

$$G_c = \frac{12(1-\nu^2)P_c^2 a^2}{Eb^2 h^3}\left(1+0.64\frac{h}{a}\right)^2 \qquad (3-21)$$

when ν and E represent Poison's ratio and Young's modulus of the Si substrate. As the last geometry parameter, h indicates the half thickness of the beam as shown in Fig. 3.18(a). Thus, in the DCB testing, the critical load (P_c) and the critical crack length (a_c) are measured and calculated differently where the FPB method only measures the critical load (P_c). More importantly, the DCB technique allows for measuring multiple critical loads by loading and unloading the sample repeatedly, as schematically shown in Fig. 3.18(b), as well as crack growth rates. When loading the sample, the compliance of the sample is measured and used to calculate the critical crack length (a_c) in the linear elastic region. The critical force is captured when the load vs. displacement curve starts showing nonlinear behavior. So, these two measured values (P_c and a_c) are plugged into the Eq. 3-21 to calculate the interfacial fracture toughness (G_c). Since mode I loading is applied with the pure tension, the phase angle (ψ) for the DCB sample geometry ideally becomes 0°. Generally, this method is widely used for describing the subcritical crack growth behavior including applied strain energy release rate (J/m^2) and crack propagation rate da/dt (m/s) [141, 144, 204]. In this work, the loading rate is fixed at 0.5 μm/sec

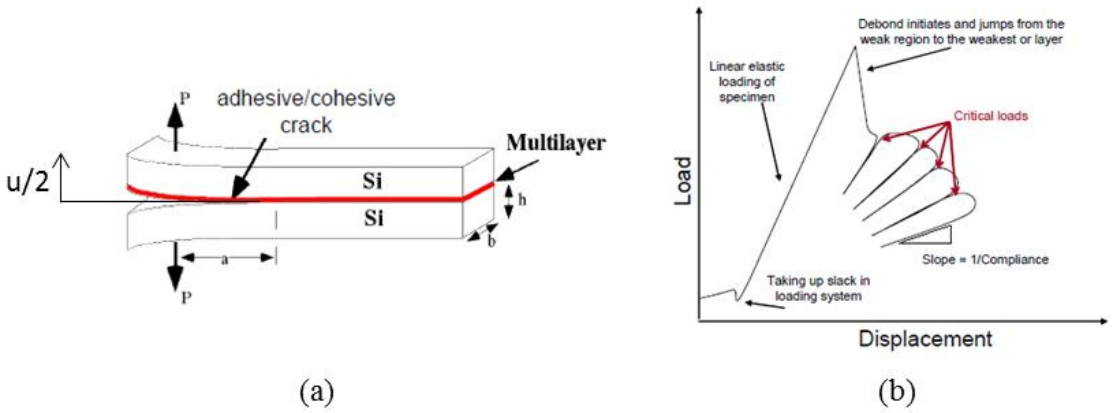

Figure 3.18. Schematic diagrams of: (a) double cantilever beam (DCB) sample and (b) general load vs. displacement curve for DCB tests [154].

3.6.4. Subcritical Debonding Test

It is also possible to determine the crack growth rate (da/dt) as a function of the driving energy (G, J/m^2) which allows one to investigate the early stages of fracture evolution called subcritical crack growth where a and t are the crack length and time, respectively [204]. Since subcritical failure can occur by progressive or time-dependent debonding at even lower stress level than interfacial fracture toughness, it is a reflection of complex interface chemistry and failure mechanisms relating the subcritical debonding to environmentally induced effects [144, 205, 206]. Amongst various environmental factors that influence the subcritical crack growth behavior, moisture-assisted subcritical debonding has been investigated [141, 153, 204], as indicated in Fig. 3.19. By assuming that dissociative chemical reactions occur between corrosive species and strain crack tip bonds, the slope changes in Fig. 3.19 represent different rate-limiting steps for the crack growth. Region I and II indicates the stress dependent chemical reactions from threshold

to intermediate value (region II) and the diffusion of the environmental species to the crack tip, respectively, while region III indicates the onset of critical bond rupture [144, 151, 154]. In addition, at the very low growth rate region in Fig. 3.19, a threshold point ($G_{th} \leq 10^{-10}$ m/s) also becomes a very important factor which is related to the device reliability without causing any interfacial failure because the cracks below G_{th} stay in a dormant state. Therefore, G_{th} represents the maximum driving energy that the system can be tolerable without developing further subcritical cracks.

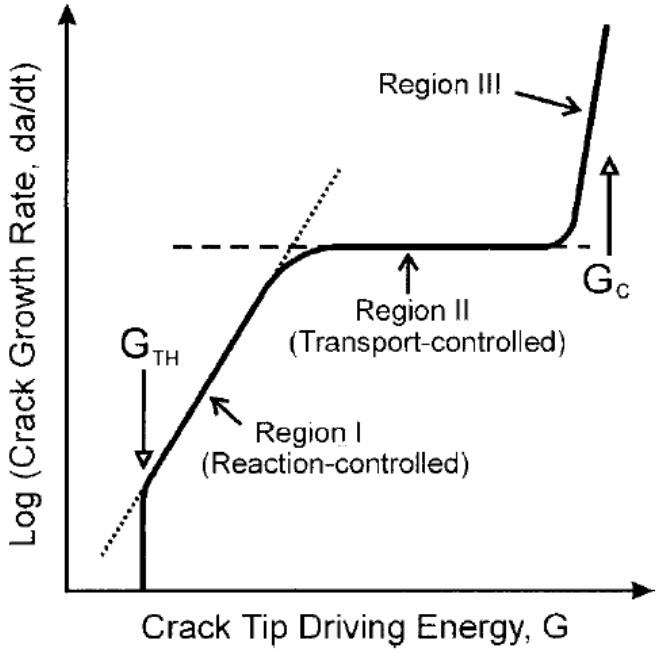

Figure 3.19. Schematic diagrams of crack tip driving energy (G) vs. crack growth rate (da/dt) curve where three different slopes show different debonding mechanics [204].

In order to develop a curve for the crack growth rate (da/dt) vs. the driving energy (G, J/m^2), FPB and DCB techniques are employed using a load relaxation technique under constant displacement conditions. Using FPB or DCB methods, a sample is loaded up to a certain load (P_o) which is less than the critical load (P_c) and the sample is fixed at the same displacement as shown in Fig. 3.20(a). Thus, the resulting time dependent load relaxation at the fixed displacement increases the specimen compliance which can be related to the crack extension using Eq. 3.22. Using Eq. 3.22 [144]can entirely produce the load vs. time curve, as shown in Fig. 3.20(b).

$$\frac{da}{dt} = -\frac{dP}{dt}\frac{P_1 a_1}{P^2} \tag{3 - 22}$$

Finally, the subcritical debond growth data is fitted using a power law expression (Eq. 3.22) where C and m are the constant and the crack growth exponent that depend the material and environmental effects when G can be calculated from FPB and DCB methods.

$$\frac{da}{dt} = CG^m \tag{3 - 23}$$

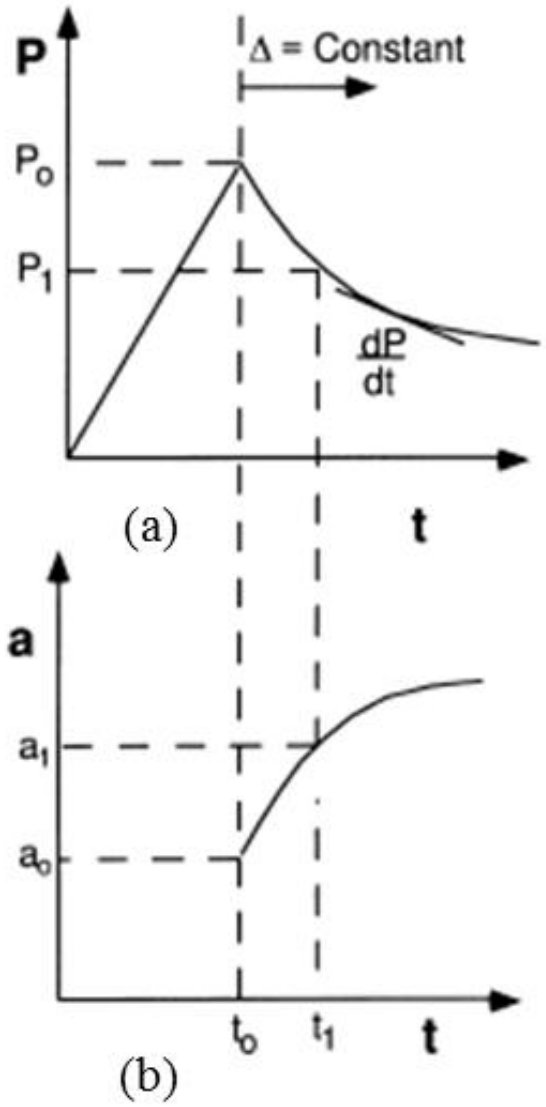

Figure 3.20. Load relaxation curves for: (a) load vs. time and (b) crack extension vs. time [204].

CHAPTER 4

EXPERIMENTAL METHODS

4.1. Introduction

This chapter covers the details of the experimental processes used to fabricate, test, and analyze four point bend and double cantilever beam samples for measuring the interfacial fracture toughness in inverted OPVs and barrier films. We first introduce all of the required sample preparation steps and introduce methods to improve the yield of the tests since poor sample fabrication can cause non-idealities during testing that prevent the measurement of the fracture toughness. Next, surface characterization tools are briefly introduced which allow the characterization from a geometrical and chemical standpoint to verify where the fracture occurred in the OPV or barrier film.

4.2. Sample Preparation for Four Point Bending Tests

4.2.1. Model Inorganic and Organic Multilayer Barrier System

4.2.1.1. Fabrication and Analysis of WVTR of Model Barrier Film

As previously discussed, multilayer barrier films consisting of alternating layers of organic and inorganic films provide one potential solution to limit the exposure of OPVs to environmental degradation from water vapor and oxygen. While there is still much debate over the exact barrier performance that is needed to yield a 20 – 25 year lifetime in solar cells, it is clear that it will depend on the architecture and materials used

in the devices. As previously discussed, inverted OPVs are more environmentally stable than conventional OPVs due to the removal of highly reactive low work function electrodes in the devices. Nonetheless, barrier films are still required and are being developed with water vapor transmission rates in the range of 10^{-4} to 10^{-6} g/m^2/day and oxygen transmission rates (OTR) in the range of $10^{-3} \sim 10^{-5}$ cm^3/m^2/day/atm [207] (Fig. 4.1).

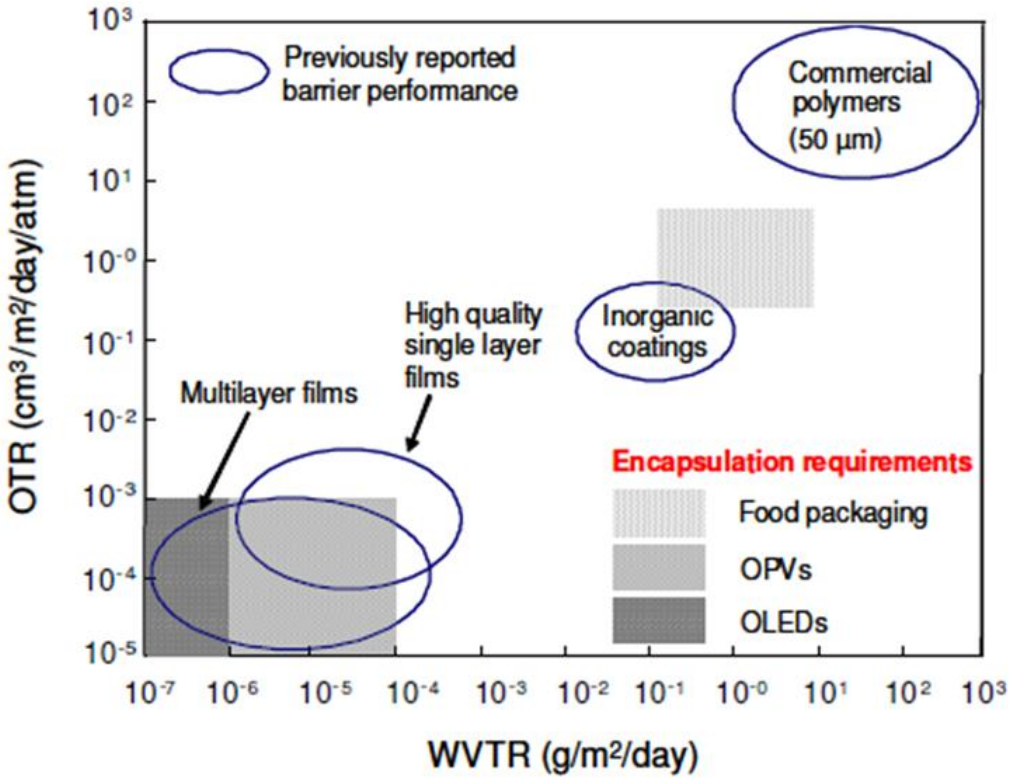

Figure 4.1. Oxygen transmission rate and water vapor transmission rate requirements for organic light emitting devices, organic photovoltaics, and food packaging [50].

There are many challenges in measuring the WVTR of such barrier films as the permeation rate through the films is quiet low. Thus, large area films and/or long test times may be required to detect a sufficient quantity of water vapor that permeates through the film. The best commercially available system today, the MOCON Aquatran, has a limit of detection of 5 x10^{-4} g/m^2/day, which puts it above the required range of detection for many of the ultra-barrier films being developed today. On the other hand, the Ca corrosion test has been developed which is very sensitive to the measurement of the effective WVTR of barrier films. Thus, in this study, WVTRs were measured by using the Ca test method which captures the degradation of the Ca films at the room temperature conditions as shown in Fig. 4.2. The Ca resistance tests were performed by monitoring the change in electrical conductance with respect to time (*dG/dt*). Using this method, the effective water vapor transmission rate was calculated according to Eq. 4-1 [205, 206].

$$WVTR\ [\mathrm{g/m^2/day}] = -n\delta_{Ca}\rho_{Ca}\frac{dG}{dt}\frac{l}{w}\frac{M(H_2O)}{M(Ca)}\frac{Area\,(Ca)}{Area\,(Window)} \qquad (4-1)$$

where, n is the molar equivalent of the degradation reaction (n=2,Ca+2H_2O →Ca$(OH)_2$+H_2) [205], δ_{Ca} and ρ_{Ca} are Ca resistivity (3.4×10^{-8} Ωm) and Ca density (1.55 g/cm^3), respectively. M (H_2O) and M (Ca) refer to the molar masses of permeating reagent (18 amu) and of Ca (40.1 amu) and *l* and *w* indicate Ca length and width, respectively [205]. In this calculation, the ratio of Ca area to permeating window area was also incorporated to account for geometrical effects of the encapsulated samples [47].

The degradation reactions of Ca in air are assumed by following chemical reactions [205, 206].

$$2Ca + O_2 \rightarrow 2CaO \quad (4 - 2)$$

$$Ca + 2H_2O \rightarrow Ca(OH)_2 + H_2 \quad (4 - 3)$$

However, in the Ca test, it is not possible to distinguish the effect from water vapor and oxygen indicating that any Ca measurement actually includes the permeation rates from wafer vapor and oxygen. However, since it is assumed that the reactions with water vapor account for higher than 95% (reactions with oxygen less than 5%) [205], we use an effective water vapor transmission rate to denote the combined effects of water vapor and oxygen which was already used to define Eq. 4-1 previously. Thus, the Ca resistance change was measured using the 4-wire resistance method using an Agilent 34970A data acquisition system, as shown in Fig. 4.2. In order to limit the effects of side permeation, the barrier was sealed over the Ca sensor using a polyisobutylene edge sealant (HelioSealTM PVS 101) with the barrier film facing down to minimize any possible damage during the indirect sealing.

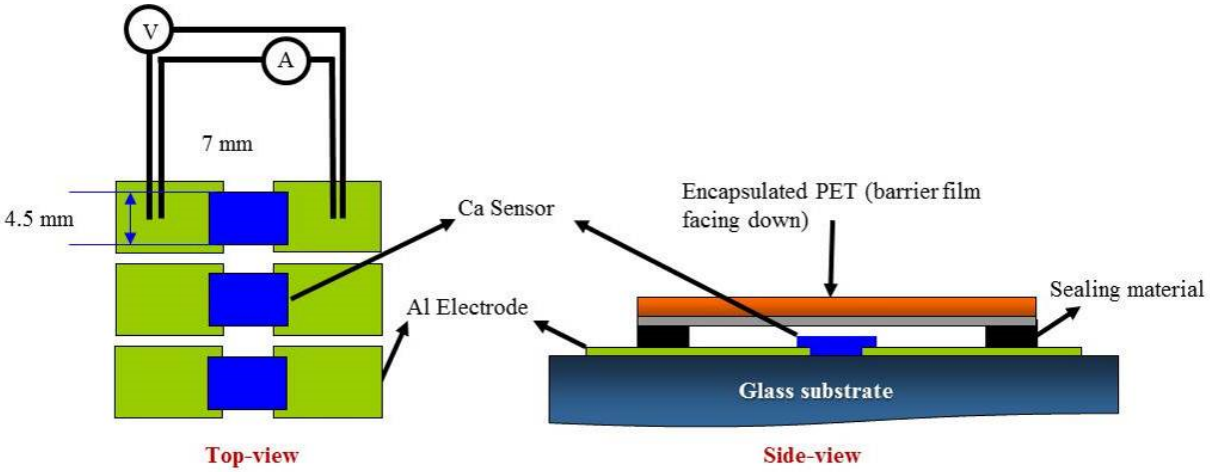

Figure 4.2. Schematic diagram of Ca test when the resistance of the Ca film is measured using 4-wire resistance method and barrier coated PET substrate is sealed using durable polyisobutylene edge sealants (HelioSealTM PVS 101).

4.2.1.2. SiN_x–PMMA Multilayer Barrier Films

As a model barrier material for this study, a multilayer barrier structure was developed by using SiN_x and PMMA combination. This system has the capability to perform very well providing an effective WVTR $\leq 5\times10^{-5}$ g/m^2/day [65, 207]. While it is understood this is not a commercially available film, it will be possible to demonstrate factors that impact interfacial adhesion in such barriers that can be translated to other inorganic/organic multilayer structures.

For the sample fabrication, PET substrates were utilized (ST-505, DuPont) with a thickness of 125 μm. In addition, PET substrates were cut into 1 inch x 1 inch samples and cleaned by 2-propanol dried using a nitrogen gun before the film depositions. First, a 100 nm thick layer of SiN_x was deposited on the PET using plasma enhanced chemical vapor deposition in a Unaxis 790 system. The films were deposited with a substrate

temperature of 110°C, RF power of 30, and a chamber pressure of 900 mTorr. The reaction was carried out using SiH_4 (200 sccm), He (560 sccm), N_2 (720 sccm), and NH_3 (14 sccm) as the reactive and carrier gases. After the film growth, the substrate was removed from the deposition system and a layer of PMMA was deposited using spin coating. For spin coating the PMMA, PMMA powder ($[CH_2C(CH_3)(CO_2CH_3)]_n$, Avg. M. W. 120,000, Spectrum Chemicals & Laboratory Products, item: P2845) and toluene were mixed with a weight ratio of 1:15 and baked on the hot plate at 80°C for 12 hours in a sealed container. The PMMA solution was spin-coated on the SiN_x surface using SCS G3 Spin Coater at 2000 rpm with 60 seconds and it was annealed at the temperature of 110°C for 30 mins to remove any residual solvent in the film. This SiN_x and PMMA fabrication processes were repeated three times on flexible PET substrate as shown in Fig. 4.3 to create the barrier film for WVTR analysis. The thickness of SiN_x (100 nm) was determined using NanoSpec 3000 Reflectometer and thickness of PMMA (400 nm) was verified using SEM while PMMA film was deposited on Si wafer, as shown in Fig. 4.4, and using KLA-Tencor P-15 profiler.

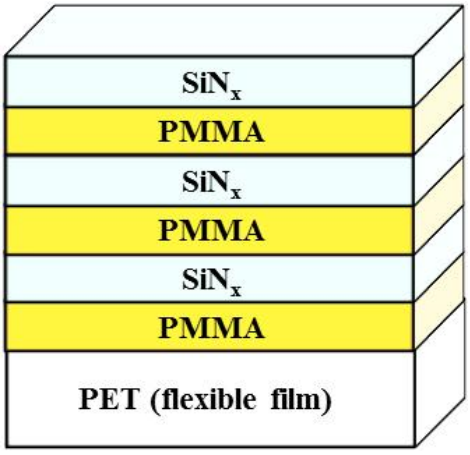

Figure 4.3. Schematic diagram of multilayer barrier films using PMMA and SiN_x combination deposited on PET substrate.

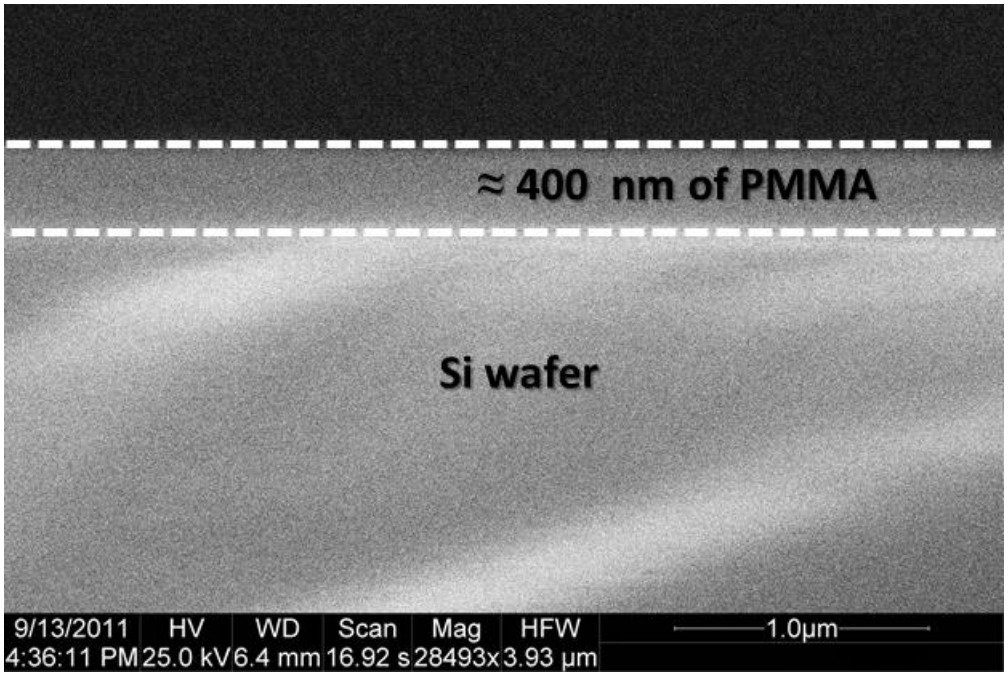

Figure 4.4. SEM image of 400 nm of PMMA spin-coated at 2000 rpm with 60 seconds while the thickness was also verified using a KLA-Tencor P-15 profiler.

4.2.2. Thin Film Fabrication for Four Point Bending Tests

Samples for the FPB interfacial fracture experiments were made by depositing bilayers of SiN_x and PMMA onto standard 4 inch Si wafers (<100> oriented wafers purchased from Wafer World, Inc) in order to conform to the structure needed for experiment. First, a thin strip of gold (thickness: 20 nm and width: 8 mm) was first deposited on the silicon wafer using e-beam deposition, as shown in Fig. 4.5(a). The gold (Au) layer plays a critical role in helping to slow the propagation of the vertical crack and allowing it to turn a propagate along the interface of interest during the four point bend test and will be explained in detail later in section 4.2.4.2.

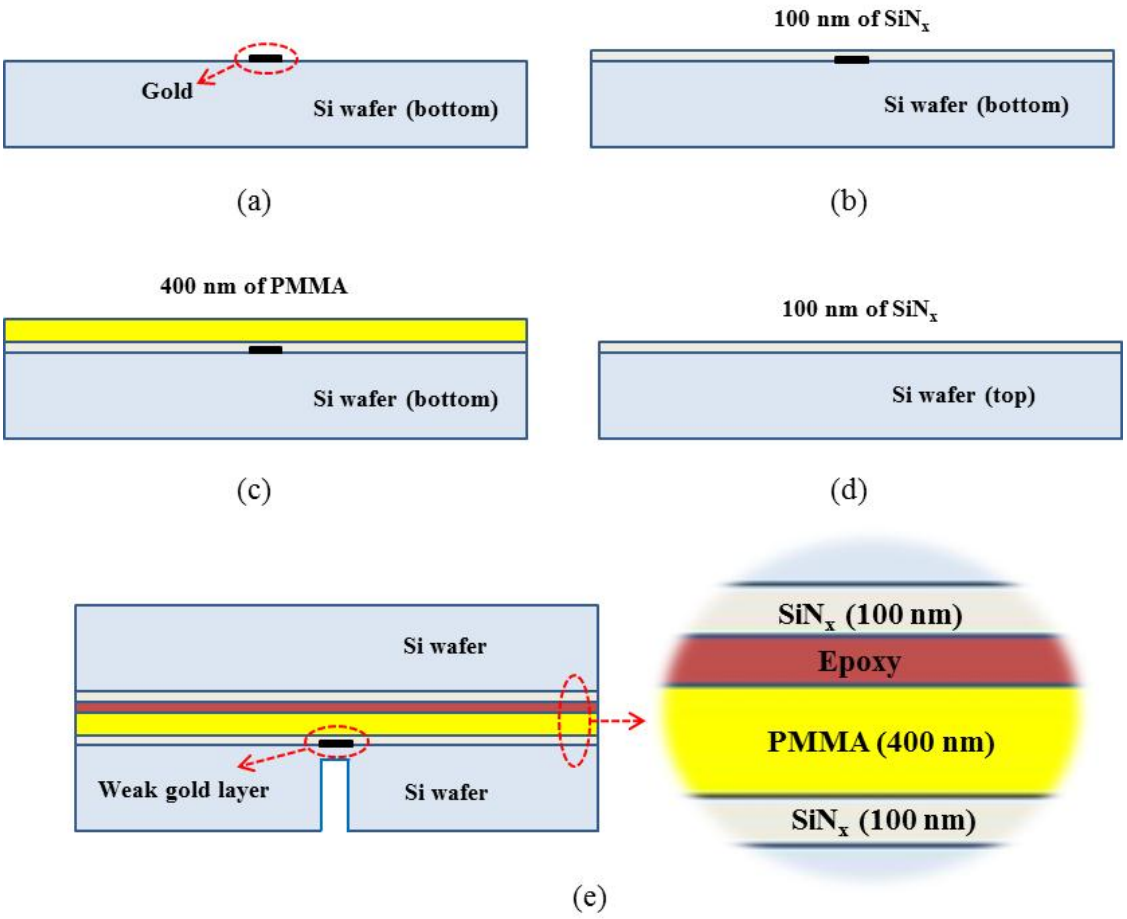

Figure 4.5. Schematic diagram of sample structure; (a) deposition of Au strip (20 nm), (b) deposition of SiN_x (100 nm), (c) spin-cast of PMMA (400 nm), (d) deposition of SiN_x (100 nm) on another Si wafer, and (e) a cross sectional image of final sample bonded by a room temperature curing epoxy (EPO-TEK 301).

Following the deposition of the gold strip, 100 nm of silicon nitride (SiN_x) was deposited over the Au and Si wafer using PECVD at 110°C as shown in Fig. 4.5(b). Next, PMMA was deposited by spin coating and annealing at 110°C for 30 mins to remove any residual solvent in the PMMA film, as shown in Fig. 4.5(c). Another 100 nm of SiN_x layer was also deposited on top of a separate Si wafer (Fig. 4.5(d)) and bonded to the Au−SiN_x−PMMA coated Si wafer using a room temperature curing epoxy (EPO-TEK

301) which was cured at room temperature for 2 days in a press to minimize the epoxy bonding thickness as discussed later. Post curing, the bonded wafers were cut into 45 mm x 5 mm pieces using a DISCO DAD-321 high speed dicing saw (Fig. 4.6) with a very thin blade (30 μm). A cross sectional image of one such sample image is shown in Fig. 4.5(e).

Figure 4.6. DISCO DAD-321 dicing saw used to cut sample for FPB and DCB sample in this dissertation (http://www.classoneequipment.com/content/disco-dad-321-dicing-saw-2).

4.2.3. Sample Cutting Method

4.2.3.1. Conventional Sample Cutting Method

After curing for 24 hours, the bonded Si wafers were cut into 45 mm x 5 mm samples. Conventional methods from the literature were first used to prepare the test samples [193]. The first method requires that the bonded wafers are cut into a 45 mm x 45 mm piece with a dicing saw (blade width: 30 μm and cutting speed: 3 mm/s) followed by cutting it again into 45 mm x 5 mm pieces as shown in Fig. 4.7(a). Since the sides of the 45 mm x 5 mm samples were very coarse due to the grinding of the dicing blade, additional polishing of the edges was required to remove roughness and defects from the edges of the sample. Once the 45 mm x 5 mm pieces were obtained, a prenotch was cut into the Si wafer directly above the Au layer in order to initiate the crack propagation during the bending test. Ideally, as the crack initiates from this prenotch, it will propagate and lose some energy as it passes through the weakly bonded Au layer and turn to propagate along the PMMA/SiN_x interface. However, it is possible to generate multiple cracks at the prenotch or elsewhere in the samples. This behavior is due to the high sensitivity of the Si sample to the defects induced by the grinding of the dicing saw. Without the removal of such defects created by the dicing process, premature failure is developed during the FPB tests as shown in Fig. 4.8.

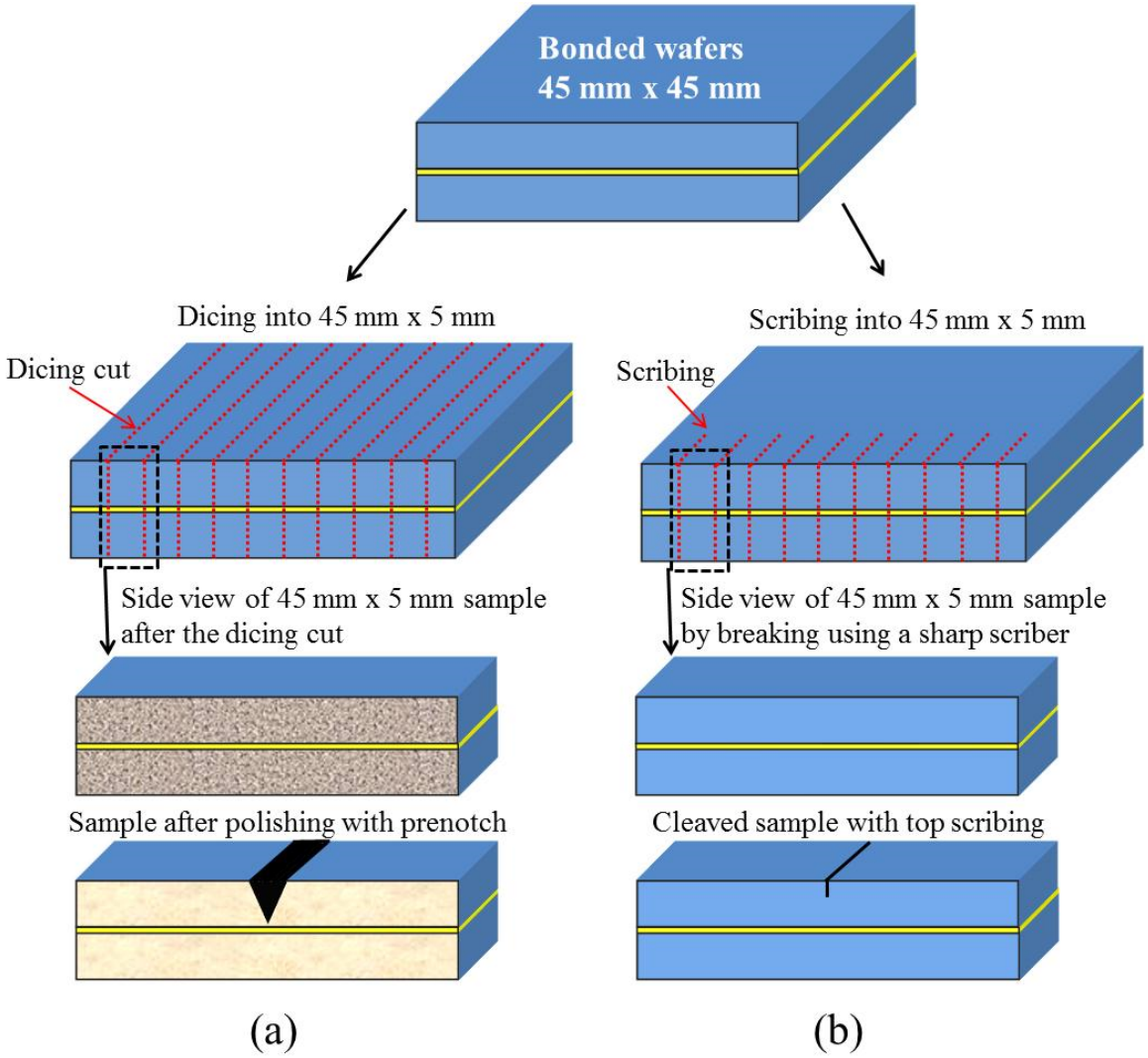

Figure 4.7. (a) Sample preparation method with additional polishing steps and (b) polishing free method that only uses a dicing saw to cut the bonded wafers into 45 mm x 45 mm sizes.

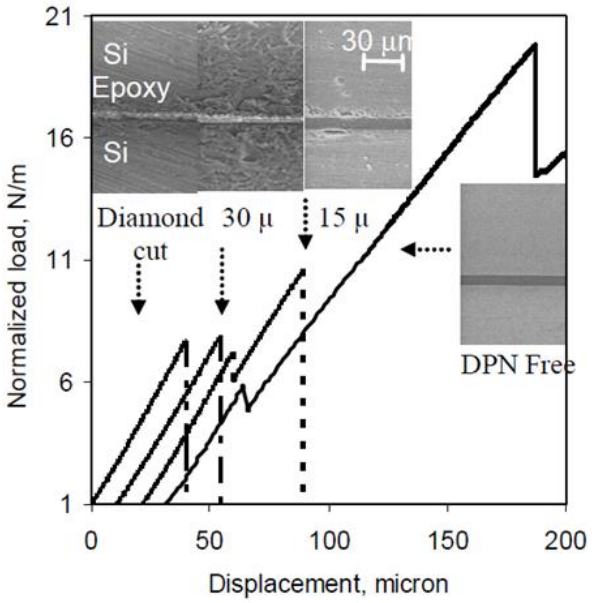

Figure 4.8. (a) Load vs. displacement curves for samples prepared using different cutting methods (Fig. 4.7(a) and (b)) while inserts show morphologies of the sidewalls with diamond cut, 30 µm polish, 15 µm polish, and cleaved surface indicating the failure load increases by reducing the sidewall defects [193]. Premature failures occurred until smooth sidewalls were achieved in the DPN method.

Again, the desire is to have as much control as possible to create a crack that propagates along the interface of interest, as shown in Fig. 4.9(a). However, even with the polishing method to make the surface smooth, very low sample yields were found with this technique as multiple cracks were often found in the samples from the flaws near the prenotch at the crack initiation point, as shown in Fig. 4.9(b). Seventy percent of the samples could fail with these irregularities, thus making the test very time consuming and less desirable.

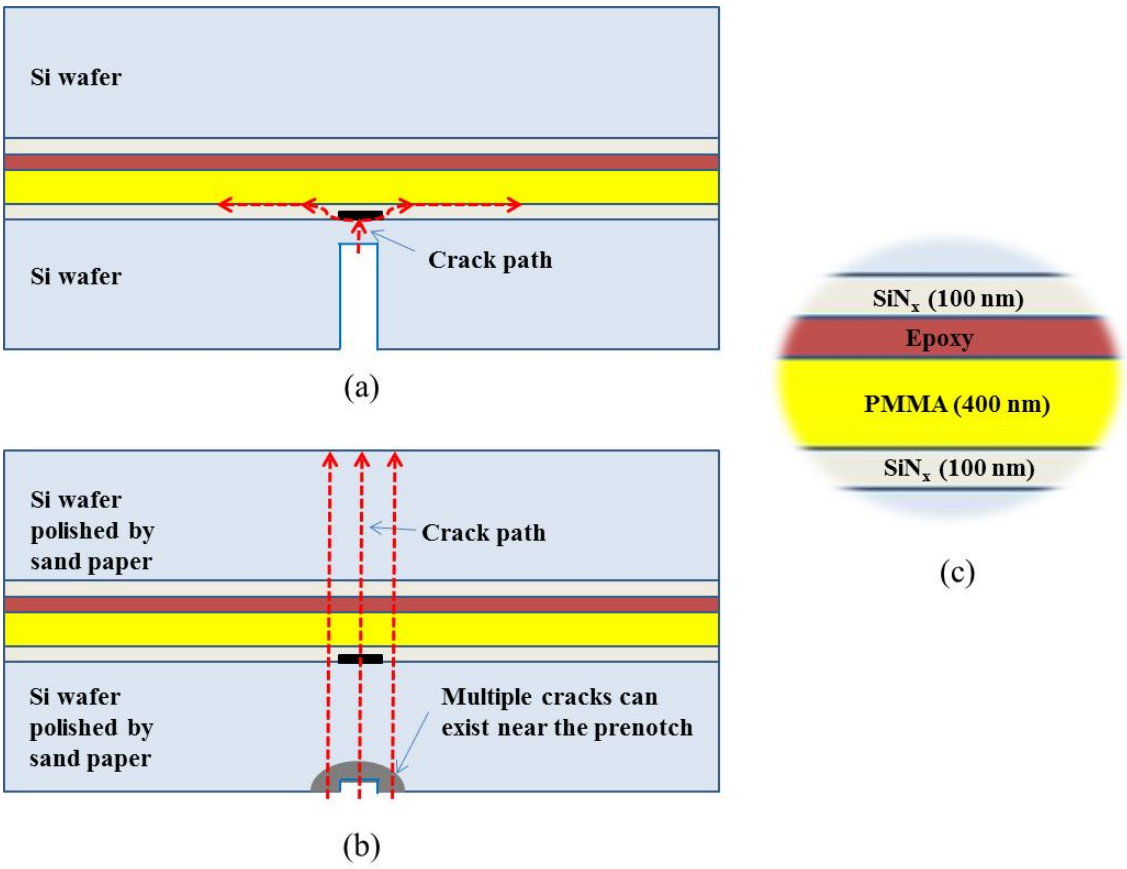

Figure 4.9. (a) The ideal crack propagation path along the interface between SiN_x and PMMA, (b) description of the incorrect failure path that results in the crack propagating through the entire specimen which can result from a shallow prenotch while other failure modes also occur when multiple cracks form near the prenotch. (c) enlargement of film structure used in FPB tests.

The second method (dicing polishing notch free, DPN) (Fig. 4.7(b)) circumvents the damage induced in the Si portion of the samples during the dicing step which also eliminates the need for polishing. To circumvent the damage caused by the dicing saw, it is possible to scribe and break the single crystal Si along preferable crystallographic directions, obtaining atomically smooth facture surfaces with low defects, as shown in Fig. 4.8. To use the orientation of the Si wafer, the scribe lines were made perpendicular to the <110> (plane of primary and second flat) plane of the <100> oriented Si wafers. This polishing free method only uses a sharp diamond scriber to make notches for cutting

the bonded wafers. However, since we need to make the notches on the top and bottom at exactly same positions for utilizing the orientation of the Si wafers, it becomes almost impossible to make the exact size of 40 mm x 5 mm test samples which makes hard to adopt for our sample preparation. In addition, as shown in Fig. 4.10, the flat region versus load from these two conventional methods are usually short (≤ 20 μm) due to the shallow prenotch and the sample damage which makes it very hard to determine the critical force (P_c) when calculating the interfacial fracture toughness (G_c). Due to this variation, these techniques were eliminated from our study. Since the conventional methods shown in Fig. 4.7 from the literature [193] inherently have such disadvantages, a new sample preparation method was developed which will be introduced in the following section.

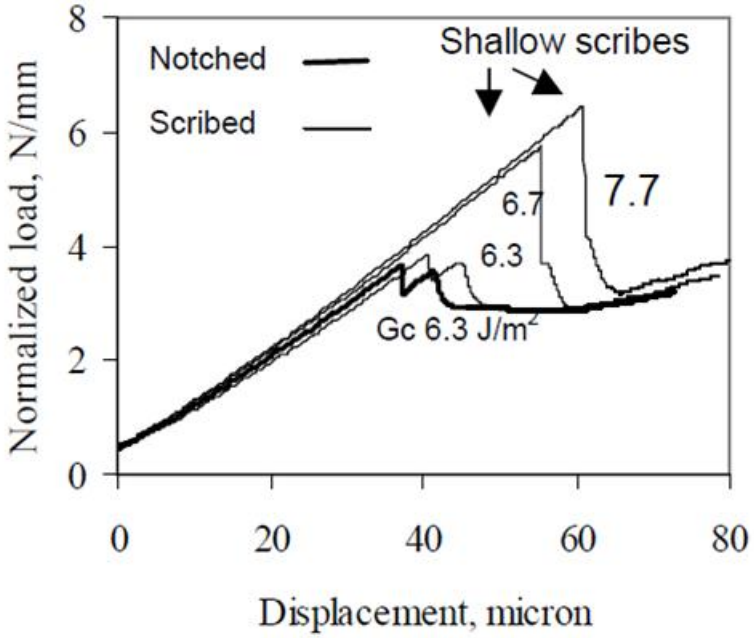

Figure 4.10. Load vs. displacement curves from the conventional methods (Fig. 4.7) indicating a very short flat regions (≤ 20 μm) which makes hard to determine the critical force (P_c) when calculating the interfacial fracture toughness (G_c) [193].

4.2.3.2. Polishing Free Method

In order to increase the yield of the FPB test, it was necessary to reduce damage near the notch root due to the low damage sensitivity of the Si wafer. As seen in the previous section, this can be done by scribing and breaking, but this yields large variations in sample dimensions. To overcome the issues in the two methods mentioned in the literature, aspects of both processing methods were combined to create a polishing free method with greater control over sample dimensions. To do this, the bonded Si wafers were first cut into a 70 mm x 45 mm piece. Next, scribe notches were made using the dicing saw on the top and bottom Si surfaces down to 60% of the thickness of the Si wafer. The cuts were made perpendicular to <110> (plane of primary and second flat) plane of <100> oriented Si wafers. The scribe notches were made at the same locations on the top and bottom wafers using an optical alignment system of the DISCO DAD-321 dicing saw (Fig. 4.6) to give us an accurate vertical positioning of the scribe notches. Next, the fracture prenotch was made on the top substrate above the Au layer down to 80~90% of the thickness of the Si wafer. This prenotch served as the vertical crack initiation point as shown in Fig. 4.12. By using a deep prenotch during the FPB tests, less strain energy is needed to break the remaining Si ligament in the structure and thus, the crack reaches the Au layer with less energy. This makes it easier for the crack to turn and transition along the interface of the FPB sample versus propagating through the entire structure as shown in Fig. 4.9. The final 45 mm x 5 mm test sample was cleaved from the prenotched sample with well defined dimensions as shown in Fig. 4.11(e).

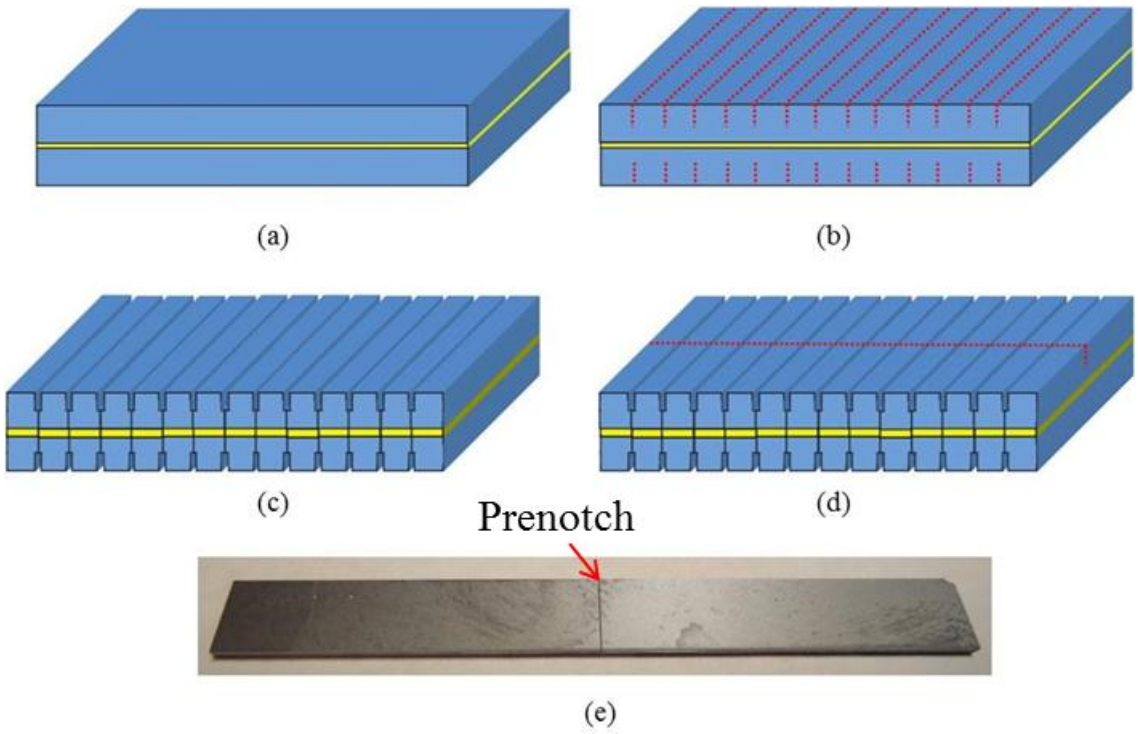

Figure 4.11. Polishing free sample cutting method: (a) Dice a 70 mm x 45 mm piece from the bonded wafer, (b) cut scribe notches on top and bottom down to 60% of the thickness of each Si wafer on top and bottom, (c) 70 mm x 45 mm piece after the prenotch cut, (d) cut prenotch down to 80-90% of the thickness of the Si wafer directly above the Au layer to serve as the crack initiation, and (e) extract the final four point bending sample (45 mm x 5 mm) by breaking the samples from figure (d) along the scribe notches to yield a smooth surface around the fracture initiation prenotch.

By doing this, low defect and atomically smooth surfaces exist around the vertical prenotch which reduces the random failures and provides more control over the crack initiation location as seen in Fig. 4.12. As a result, this new method gives several benefits compared to the conventional methods that were discussed in section 4.2.3.1: (a) less sample damage from the dicing process at the prenotch root (Fig. 4.12(d)), (b) accurate sample cutting from the optical alignment system of the dicing saw, and (c) higher sample yield during testing (>70% yield), and (d) a long flat constant load region

during the bending test used to clearly determine the critical load. Thus, this method is used throughout this work for fabricating four point bend test samples.

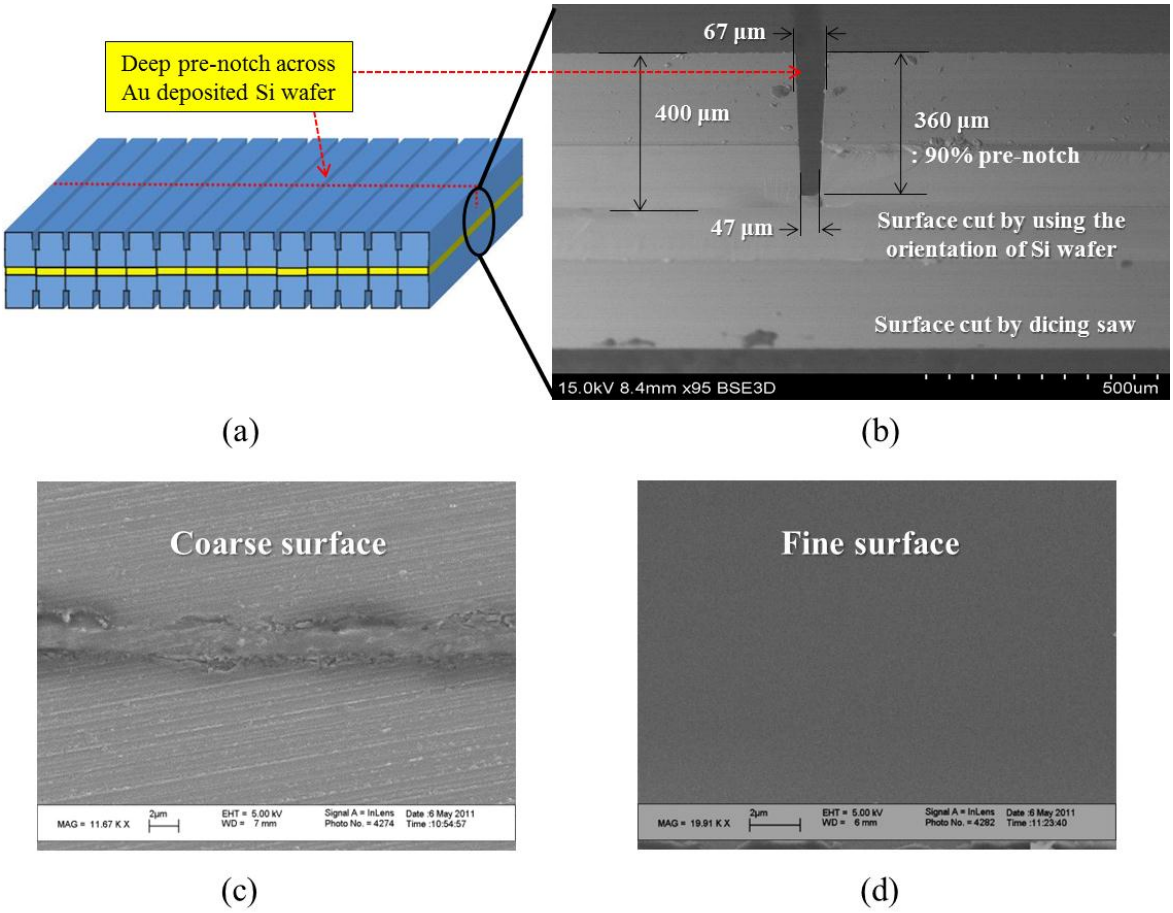

Figure 4.12. (a) Bonded Si wafers with pre-notch using a dicing saw (Fig. 4.8(d)), (b) cross sectional SEM image of four point bending (FPB) sample surfaces cut by a dicing saw, (c) SEM image of Si bonded wafer cut by only dicing saw, and (d) SEM image showing the fine surface which was created by using the polishing free method.

4.2.4. Thickness Control of Epoxy

In developing FPB samples, it is critical to minimize the thickness of the epoxy to limit energy dissipation in this layer during the fracture process. Epoxy layer thicknesses on the order or less than 1μm have been found to be sufficient for a wide range of FPB testing by previous researchers. In order to minimize the thickness of the epoxy, top and bottom wafers were sandwiched together using two thick metal substrates pressed using an Irwin Quick-Grip 6-inch Clamp as shown in Fig. 4.13.

When the thickness of the epoxy layer is significantly thick, most of the applied energy is absorbed by the thick epoxy which will eventually cause an overloading issue during the mechanical bending tests. Thus, if the overloading issue occurs from the plasticity effect in the epoxy layer, it becomes hard to obtain the critical load (P_c) because the vertical crack from the top substrate directly goes into the bottom substrate and breaks the test sample without changing the crack direction. In this dissertation, this clamping method to minimize the thickness of epoxy was used for FPB and DCB samples.

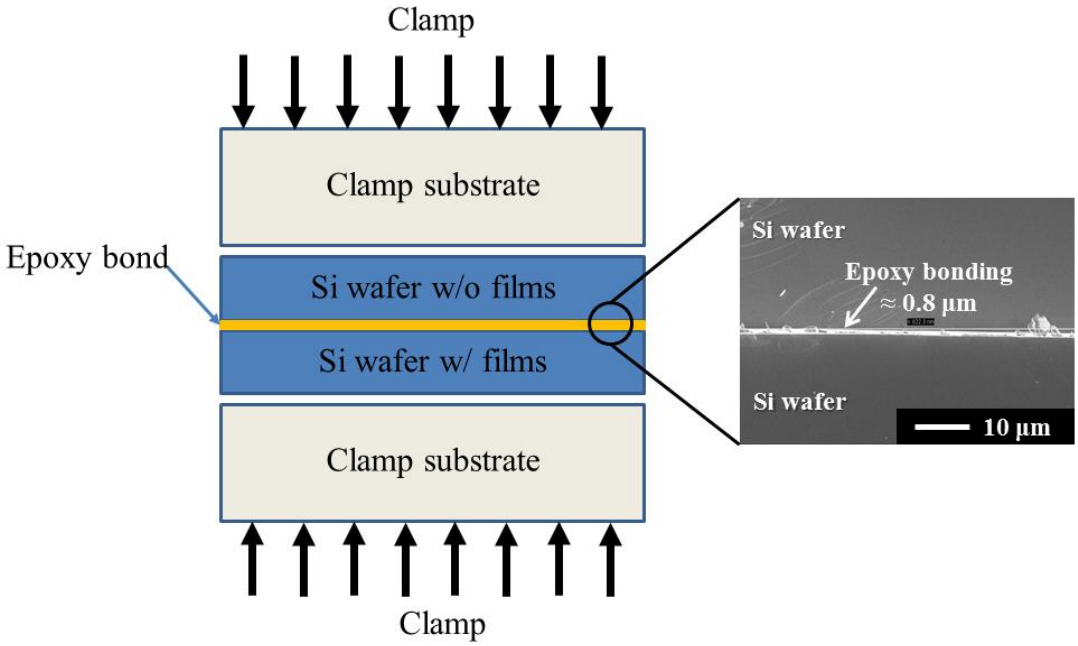

Figure 4.13. Si wafers bonded using a room temperature curing epoxy sandwiched by metal substrates under high load using a Irwin Quick-Grip 6-inch Clamp where a SEM image shows the thickness of the epoxy layer after 2 days curing.

4.3. Sample Preparation for Double Cantilever Beam Tests

4.3.1. Device Fabrication

Double cantilever beam samples were used to test the interfacial adhesion and cohesion in inverted organic photovoltaics. The samples were made with thermally oxidized (300 nm of SiO_2) 4 inch Si wafers (<100> orientation purchased from University Wafers) as the substrate to act as the large elastic and compliant member in the experiment. Since the OPVs did not need to be operational for the mechanical tests, ITO was not used as an electrode when building the inverted OPV devices. Instead, the SiO_2 layer was used as a surrogate for the ITO on which the remainder of the device was built. On top of the SiO_2 layer, interface modifiers such as ZnO were deposited to interface with the active layer of the OPV. Thus from a material point of view, the active layer sees the same chemical interface as it would in the operational device and is not expected to behave differently in this surrogate structure versus the real structure. It should be noted that the sample fabrication was performed in collaboration with Professor Bernard Kippelen's group of the School of Electrical and Computer Engineering at the Georgia Institute of Technology and the National Renewable Energy Laboratory (Dana Olson, Joe Berry, Sarah Cowan, Corinne Packard, and Mukesh Kumar). Moreover, special recognition is given to Mukesh Kumar and Sarah Cowan of NREL who made the P3HT:PCBM OPVs while Jae Won Shim of Prof. Kippelen's group fabricated the PBDTTT-C:PCBM OPVs for this experiment.

In this dissertation, two different types of inverted organic photovoltaic devices were fabricated and tested using P3HT:PC_{61}BM [208] and PBDTTT−C:PC_{60}BM [209] BHJ active layers. Before making any film deposition, thermal oxidized 2" x 2" square Si substrates were cleaned in an ultrasonic bath of detergent (Liqui−Nox® Phosphate-

Free Liquid Detergent, Alconox, Inc., White Plains, NY) water, rinsed with deionized water, and then cleaned in sequential ultrasonic baths of deionized water, acetone, and 2-propanol. Nitrogen was used to dry the substrates after each bath. After cleaning, the first structure was fabricated using P3HT:$PC_{61}BM$ BHJ active layer which is the most widely used polymeric active layer (PCE < 4%) [25, 30, 208, 210-212], as shown Fig. 4.14. As the first layer, ZnO was deposited using diethylzinc sol-gel solution (1.1M in toluene, purchased from Sigma Aldrich), additionally stabilized by mixing (1:3) by volume in anhydrous tetrahydrofuran (purchased from Sigma Aldrich). ZnO films were spin cast in air to a thickness 40 nm or conditions of 7,000 RPM for 60 seconds. Subsequently, films were annealed at 120 ˚C in air for 20 min and allowed to cool down. After the ZnO deposition, Poly(3-hexylthiophene-2,5-diyl) (P3HT) (Reike, 4002-EE) and phenyl-C61-butyric-acid methyl ester ($PC_{61}BM$) (Nano-C) were used as received. Films of P3HT:$PC_{61}BM$ blend (25 mg P3HT /mL; 20 mg $PC_{61}BM$ /mL (1:0.8 wt%) in anhydrous 1,2-dichlorobenzene (Aldrich)), were spun at room temperature conditions at 600 rpm for 60 seconds onto the ZnO layer (~250 nm). Each substrate was then slow-dried in an individual petri dish in a nitrogen environment until dry. Substrates were then annealed at 150°C for 10 minutes. As an interlayer, Plexcore OC XA-1871™ (given by Plexcore company) hole−collecting contact was spun onto the active layer in air at a rate of 2000 RPM for 60 seconds (~50 nm). Films were subsequently annealed in the glove box at 120°C for 10 minutes to promote solvent evaporation. As another interlayer, MoO_x (Sigma Aldrich) was deposited via thermal evaporation at $5x10^{-7}$ T pressure and a rate of 0.2 A/s to 10 nm thickness. As the last electrical contact, Ag was evaporated in an Angstrom Thermal Evaporator system, with a base pressure of $2x10^{-8}$ Torr, and an

evaporation pressure of $8x10^{-7}$ Torr at 1.0 Å s^{-1} for 100 nm of silver. To this structure, a second SiO_2/Si wafer was bonded as shown in Fig. 4.14. Recently, NREL (National Renewable Energy Laboratory) reported 3.5% PCE with this structure (Fig. 4.14).

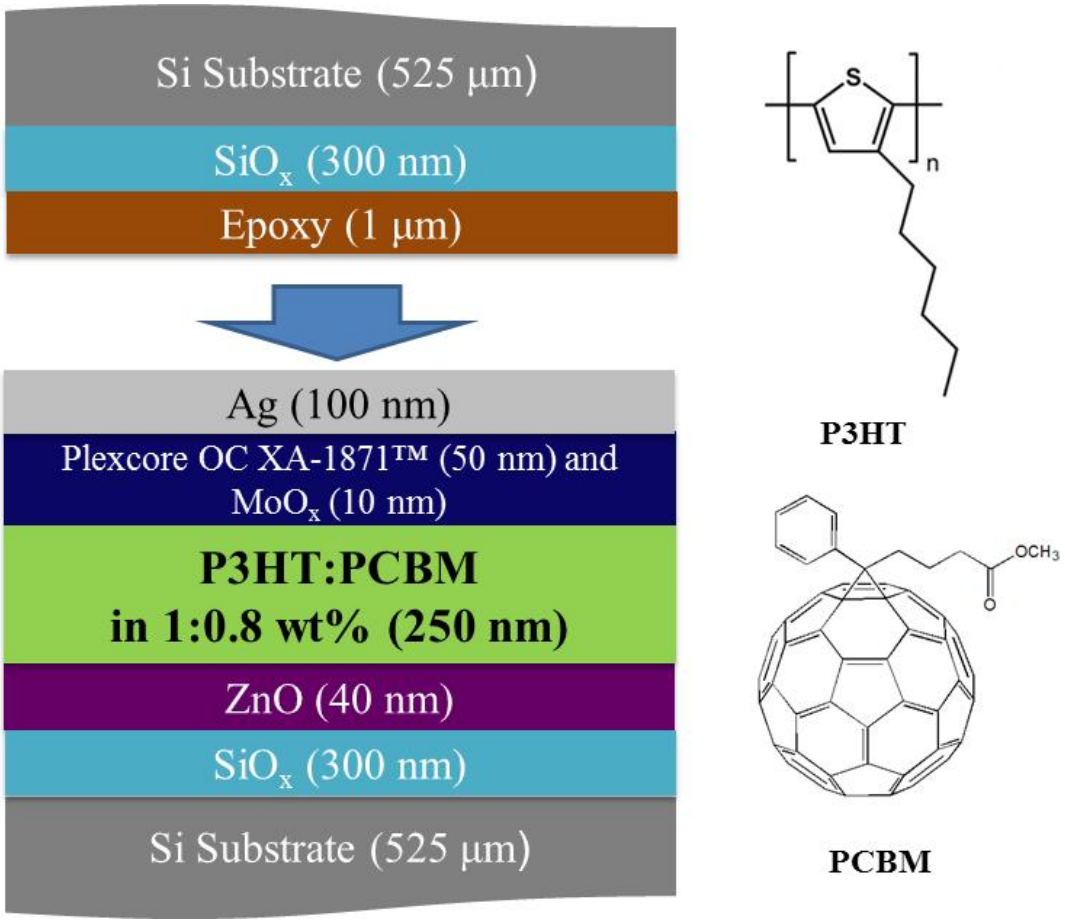

Figure 4.14. A cross sectional image of DCB sample structure including Si wafer, ZnO, active layer (P3HT:$PC_{61}BM$), MoO_x/ Plexcore OC XA-1871™ hole collecting contact, and Ag bonded with another Si wafer using a room temperature curing epoxy (EPO-TEK 301).

For the second structure using PBDTTTC−C:$PC_{60}BM$ BHJ active layer (Fig. 4.15) which recently shows 6.6% PCE [209], a 28 nm thick ZnO layer was first deposited using atomic layer deposition (ALD) system (Savannah 100, Cambridge Nanotech, Cambridge, MA) using diethyl zinc as the Zn precursor and water as the oxidant. To deposit the ZnO, one growth cycle in the ALD system was comprised of sequential pulses of H_2O (15 ms pulse) and diethyl zinc (15 ms pulse) precursors injected into the ALD reactor utilizing nitrogen as a carrier gas at a temperature of 150°C. Another electron selective contact, polyethylenimine (PEIE), was also used to replace ZnO in this study to investigate the effect of polymer/polymer contacts on mechanical properties in OPVs. Polyethylenimine (PEIE) (80% ethoxylated, M_w ~70,000 g/mol, 35-40 wt. % in water purchased from Aldrich, St. Louis, MO) was diluted into 2-Methoxyethanol (Aldrich, St. Louis, MO) to a concentration of 0.4 wt. % and stirred overnight in ambient air. A10 nm thick PEIE (0.4 wt.%) layer was spin cast through a 0.2-μm-pore PTFE filter onto the substrates in air at a speed of 5000 rpm for 1 minute followed by thermal annealing on a hotplate at a temperature of 100 ºC for 10 minutes in air.

To deposit the active layer, a solution of PBDTTT−C (Solarmer Materials, Inc., El Monte, CA):$PC_{60}BM$ (Nano−C, Westwood, MA) was made in a mixed solvent of chlorobenzene (Aldrich, St. Louis, MO) and 1,8-diiodooctane (Aldrich, St. Louis, MO), (97:3, v/v) with a weight ratio of 1:1.5 (PBDTTT−C:$PC_{60}BM$) and a total PBDTTT−C:$PC_{60}BM$ concentration of 25 mg/ml. The PBDTTT−C:$PC_{60}BM$ solution was stirred overnight in a nitrogen-filled glove box before the use. Approximately, 90 nm thick PBDTTT-C:$PC_{60}BM$ layer was deposited on top of substrates by spin coating at a speed of 1000 rpm for 20 seconds. As an interlayer between PBDTTT−C:$PC_{60}BM$ and

Ag electrode, two different types of interface modification layers were used. First, MoO_x was used in conjunction with the ZnO bottom contact to investigate an inverted OPV with all inorganic contact to the active layer. MoO_x was also used with PEIE replacing ZnO to isolate the effect of PEIE on the adhesive/cohesive failure. Next, PEDOT:PSS CPP 105 DM (H.C. Starck, Newton, MA) was used instead of the MoO_x with the ZnO bottom contact to isolate the effect of PEDOT:PSS. Finally, PEDOT:PSS was used with the PEIE bottom contact to investigate the performance of an all polymer contact architecture. To deposit the MoO_x layer, samples were loaded into a vacuum thermal evaporation system (SPECTROS, Kurt J. Lesker) and 20 nm thick layer of MoO_x (estimated from the crystal thickness monitor) was deposited at a rate of 0.1 ~ 0.2 nm/second and a base pressure of ~8×10^{-8} Torr. For PEDOT:PSS CPP (100 nm), this layer was spin−coated on top of the active layer at a speed of 2000 rpm for 45 sec in air and annealed at 120 °C for 10 min in the N_2 filled glove box. As a final step, the samples were transferred to the vacuum thermal evaporation system and 150 nm of Ag was deposited at a rate of 0.1 ~ 0.2 nm/second and a base pressure of $\approx 8 \times 10^{-8}$ Torr. The final sample structure is shown in Fig. 4.15.

In order to prepare for the double cantilever beam (DCB) samples, a bare 2" x 2" SiO_2/Si substrate was used to bond with the OPV films on the coated SiO_2/Si wafer using a room temperature curing epoxy (EPO-TEK 301) in the same way that was done for making FPB sample, as already discussed in section 4.2.4. This bonded sample was cured at room temperature for 2 days and was cut by using DISCO DAD-321 dicing saw (Fig. 4.6) with a very thin blade (30 μm).

.

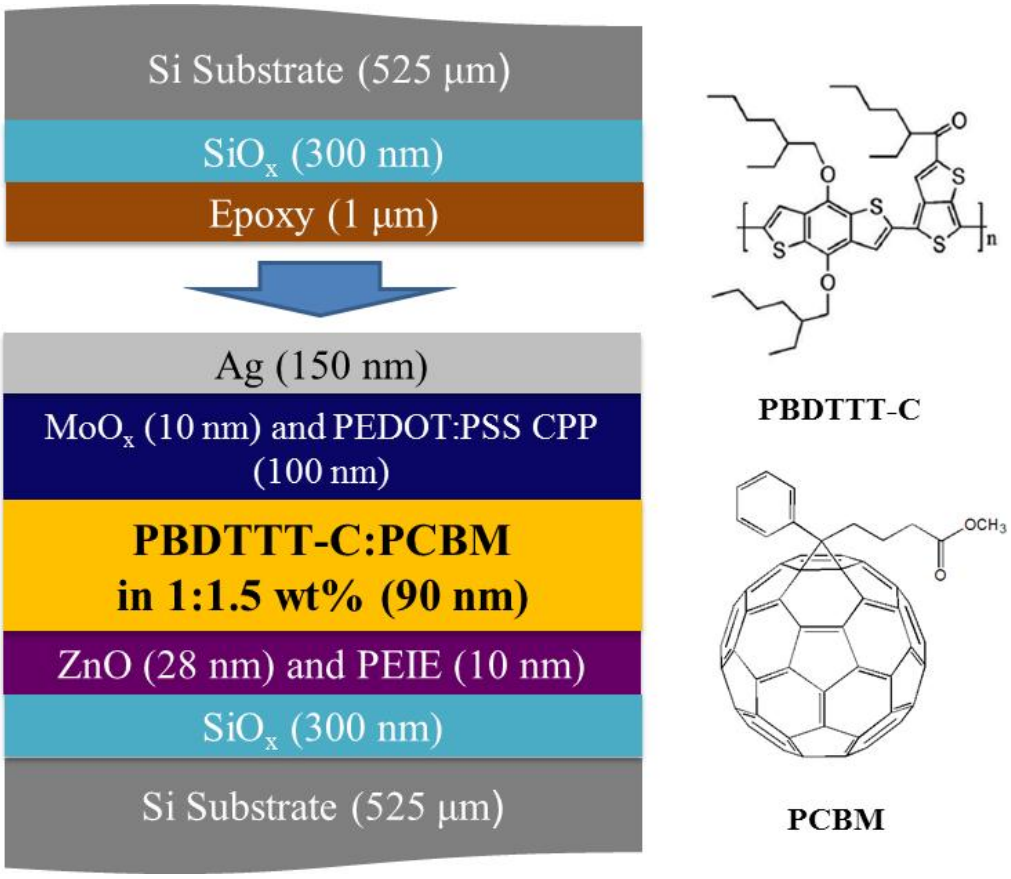

Figure 4.15. A cross sectional image of DCB sample structure including Si wafer, ZnO/PEIE, active layer (PBDTTT−C:PCBM), MoO_x/PEDOT:PSS CPP, and Ag bonded with another Si wafer using a room temperature curing epoxy (EPO-TEK 301).

4.3.2. DCB Sample Preparation Using Dicing Saw

Double cantilever beam (DCB) samples were prepared in a similar manner to the FPB sample preparation, but without the fracture prenotch. To increase the yield of the DCB test, it was also necessary to reduce possible damage around the sidewall due to the low damage sensitivity of the Si wafer. Additionally, since some of the interfaces in the inverted OPV devices can be easily damaged during the dicing process from the dicing blade, scribe notches on the top and bottom were made using the dicing saw to cleave the samples as shown in Fig. 4.16. To make the final 5 mm x 45 mm DCB samples from 50.8 mm x 50.8 mm pieces (Fig. 4.16(a)), the scribe notches were made down to 60% of the thickness of the Si wafer using the high speed dicing saw, as shown in Fig. 4.16(b) and (c). An example of a cleaved sample with grips attached using an epoxy for the DCB tests is shown in Fig. 4.17.

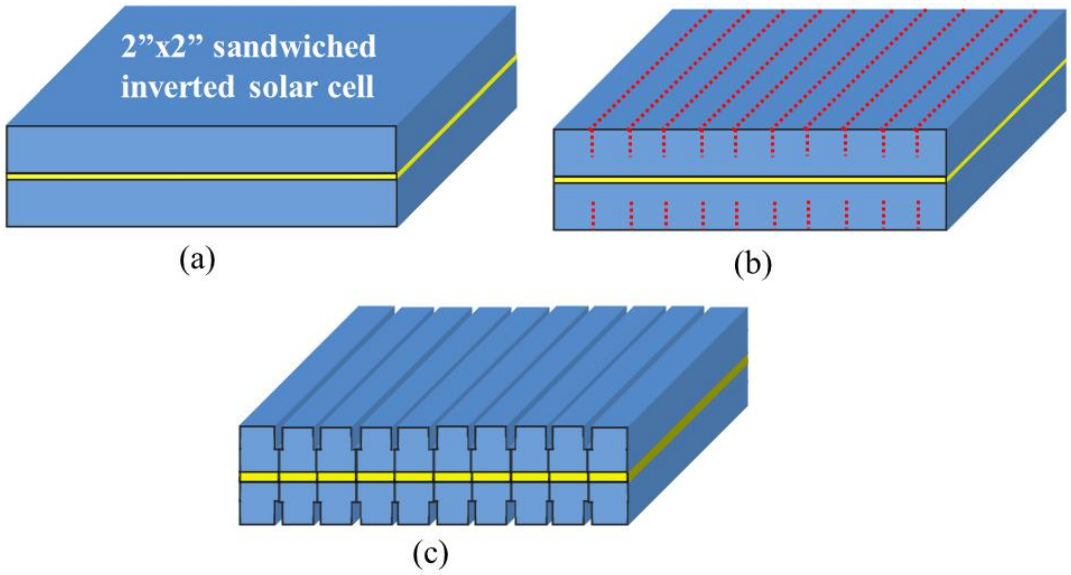

Figure 4.16. Double cantilever beam (DCB) sample preparation: (a) 50.8 mm × 50.8 mm (2" × 2") piece bonded using the room temperature curing epoxy (EPO-TEK 301), (b) pre-notch on top and bottom down to 60% of the thickness of single Si wafer, and (c) 50.8 mm × 50.8 mm piece after the pre-notch cut.

Figure 4.17. Final 45 mm x 5 mm double cantilever beam sample with tension grips attached on the sample using a room temperature curing epoxy.

4.4. DTS Delaminator

For FPB and DCB tests to measure the adhesion and cohesion strength in barrier films and inverted OPVs, a DTS Delaminator table top mechanical test system (Dauskardt Technical Services, Inc.) was entirely used in this study, as shown in Fig. 4.18(a). In order to measure the mechanical properties of the nanoscale films, the DTS delaminator is equipped with an high-resolution piezoelectric motor actuator (100nm step resolution) and a load cell (maximum measured force = 200 N) that allows control of the displacement at 0.5 μm/s during the tests (Fig. 4.18). For FPB tests, four physical contacts are made using two bend grips which have different spans between contact points (40 mm and 27 mm) as shown in Fig. 4.18(b). However, for DCB tests, different grips were used to connect the DCB sample (Fig. 4.17) to DTS delaminator (Fig. 4.18(c)). The detail dimensions of DCB grips connecting to the DTD delaminator are shown in Fig. 4.19. Thus, using these grips, pure mode I loading was applied to the DCB samples.

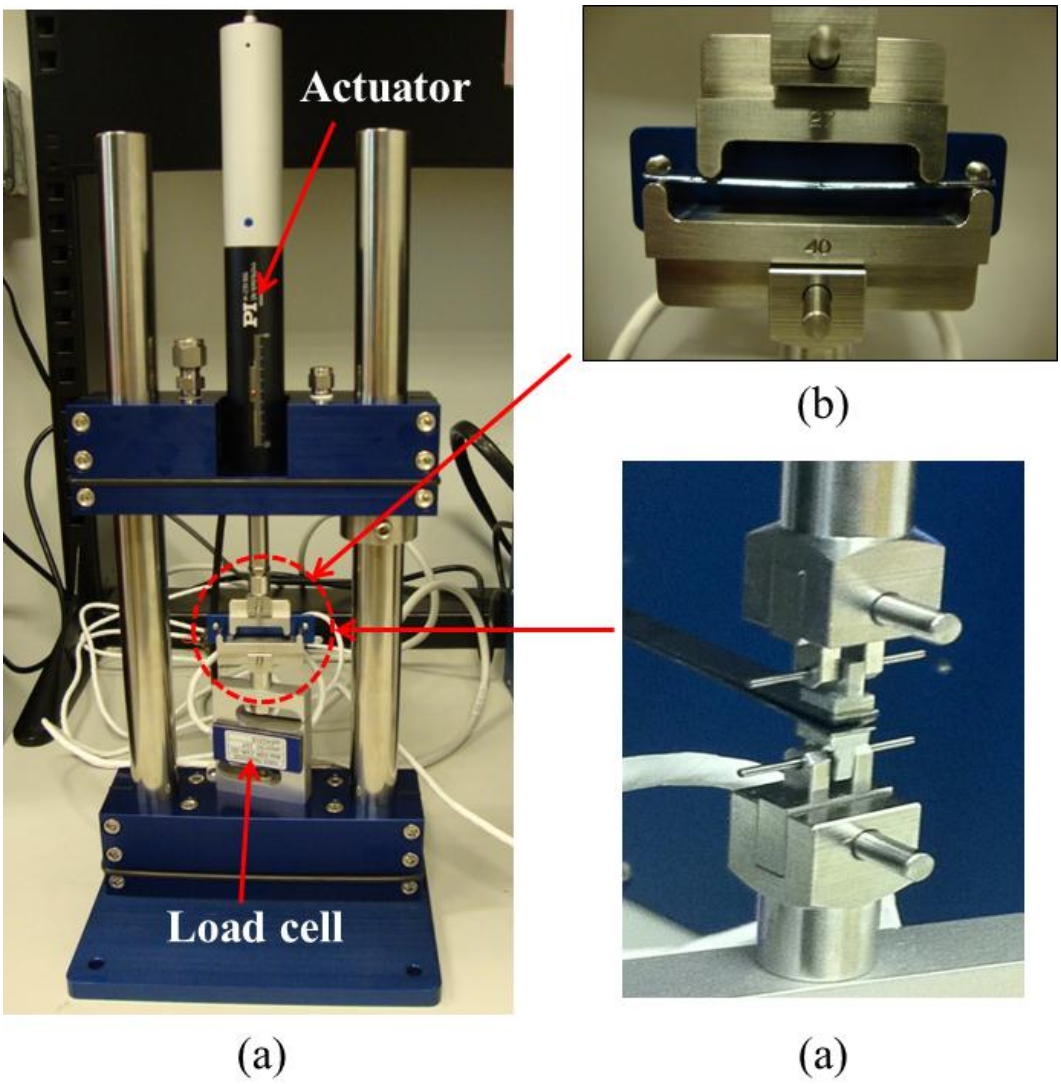

Figure 4.18. (a) DTS delaminator with a high-resolution piezoelectric actuator andload cell (maximum measured force = 200 N), (b) bend grips for FPB tests, and (c) grips for DCB tests.

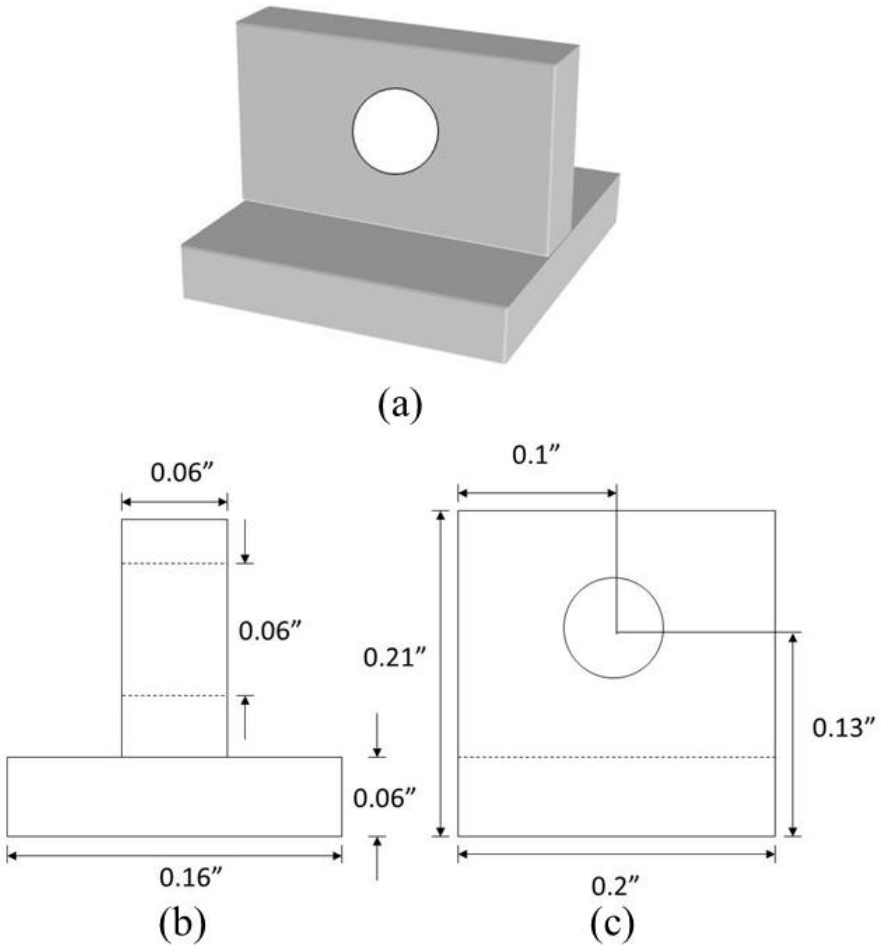

Figure 4.19. (a) Schematic diagram of a DCB grip, (b) side view of the DCB grip with specific dimensions, and (c) front view of the DCB grip with specific dimensions.

4.5. Contact Angle Measurements

Surface energy is the quantification of the disruption of molecular bonds when a surface is created through breaking the bulk material. The total surface energy is determined by van der Waals forces (Keesom force, Debye force, and London force) [166]. Since the surface energy cannot be directly measured, it is possible to infer through the measurement of the contact angles of liquid droplets (with known surface energies and characteristics) on the surface of interest that tell us the interactions between the liquids and the surfaces as shown in Fig. 4.20. In Fig. 4.20, γ_{sl},

γ_{lv}, and γ_{sv} represent the interfacial tensions between the solid and the liquid, the liquid and the vapor, and the solid and the vapor, respectively, and the θ_c is the measured contact angle. Thus, in order to evaluate the permanent and instantaneous dipole-dipole reactions at the interface, the contact angles with two different liquids (Di water and Diiodomethane) using the Ramé-hart Model 250 goniometer (Fig. 4.21) are measured on surfaces and converted to the surface energies by using Eq. 4-4 [213]. The polar (γ^p) and dispersive (γ^d) components are calculated from the harmonic mean method (Eq. 4-4) [213] where γ represents the surface tension, 1 and 2 refer to different liquids that were used in this work, *p* and *d* represent the polar and dispersive components, and s indicates the specific surface. This method has been used previously to measure the polar and dispersive surface energies of surfaces such as ITO, Ni200 alloy, polymer films (polymethyl metacrylate (PMMA), polycarbonate (PC), and polypropylene (PP), etc.) [175, 213].

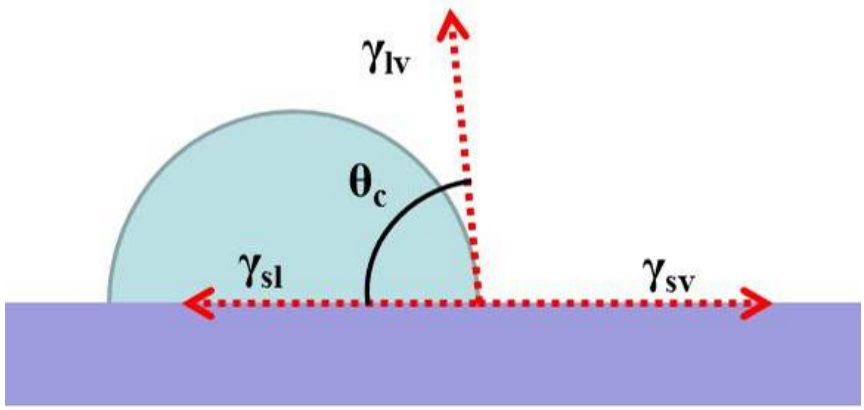

Figure 4.20. Schematic diagram of contact angle measurement.

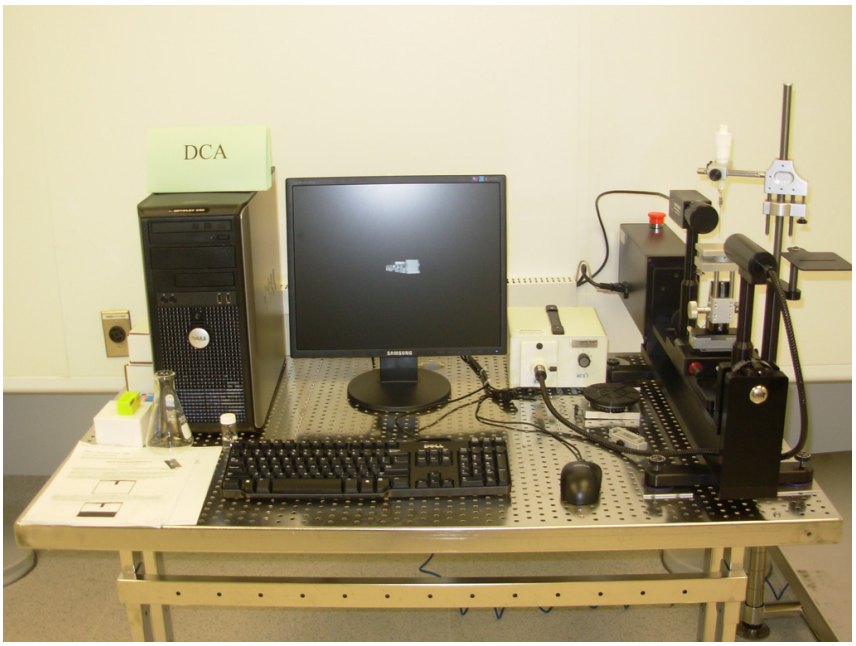

Figure 4.21. Ramé-hart Model 250 goniometer (https://cleanroom.ien.gatech.edu/equipment/195/contact-angle-measurement-system/).

$$(1+\cos\theta_1)\gamma_1 = 4\left(\frac{\gamma_1^d\gamma_s^d}{\gamma_1^d+\gamma_s^d}+\frac{\gamma_1^p\gamma_s^p}{\gamma_1^p+\gamma_s^p}\right)$$
$$(1+\cos\theta_2)\gamma_2 = 4\left(\frac{\gamma_2^d\gamma_s^d}{\gamma_2^d+\gamma_s^d}+\frac{\gamma_2^p\gamma_s^p}{\gamma_2^p+\gamma_s^p}\right) \quad (4-4)$$

4.6. Surface Characterization

4.6.1. Scanning Electron Microscopy

In this study, scanning electron microscopy was utilized as a tool to image interfaces and samples prior to and after mechanical testing. Since all of the films (PMMA, SiN_x, SiO_x, and Al_2O_3) are non-conductive, a Hitachi S-3700N VP-SEM (Fig. 4.22) was utilized to scan delaminated surfaces and cross sections of four point bending (FPB) and double cantilever beam (DCB) samples because Hitachi S-3700N VP-SEM can be operated in a variable pressure mode with a low vacuum level (6~270 Pa) enabling charge-free observation without requiring any special sample preparation.

Figure 4.22. A Hitachi S-3700N VP-SEM (https://cleanroom.ien.gatech.edu/equipment/237/hitachi-s-3700n-vp-sem/).

4.6.2. Atomic Force Microscopy

In this study, a Veeco AFM (Dimension 3100 Scanning Probe Microscope), Fig. 4.23), was used in the tapping mode to examine surface morphology after four point bending (FPB) and double cantilever beam (DBC) tests. Since inorganic films (SiN_x, SiO_x, and Al_2O_3) form very small features on the surfaces, a NSC15 cantilever (purchased from Micromasch USA) was used, which has a tip radius of 10 nm. AFM scanning was important for verifying the roughness of the surfaces prior to sample fabrication as well as analyzing features on failed interfaces post mechanical testing.

Figure 4.23. Veeco AFM (dimension 3100 Scanning Probe Microscope) (https://clea nroom.ien.gatech.edu /equipment/73/veeco-afm/).

4.6.3. X-ray Photoelectron Spectroscopy

In order to explore chemical compositions of the surface, the sample is placed in a high vacuum environment and is irradiated with a focused beam of X-rays allowing photoelectrons to be emitted from the surface, as shown in Fig. 4.24(a). The emitted electrons are collected by the electron analyzer and the kinetic energy of the emitted photoelectrons is determined by a spectrometer which finally presents intensity vs. binding energy data. The binding energy (E_b) of individual electrons that exist on the surface is determined using Eq. 4-5 with known information such as the energy of X- ray photons (hv), the kinetic energy of the emitted electron, and the work function (W) of the spectrometer [214].

.

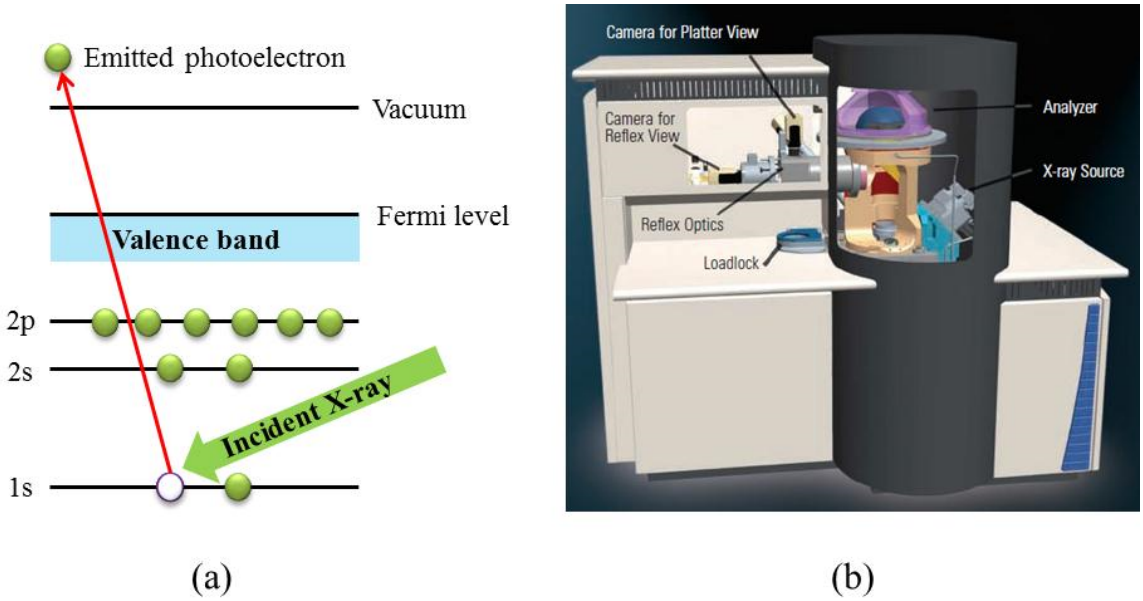

Figure 4.24. (a) Schematic showing the processes that occur during XPS and (b) a Thermo K-Alpha X-ray photoelectron spectroscope (www.thermoscientific.com).

$$E_b = h\nu - E_k - W \quad (4 - 5)$$

To accurately determine the exact failure location amongst the many layers present in our test samples after the delamination tests, a Thermo K-Alpha X-ray photoelectron spectroscope (Fig. 4.24(b)) with an Al 1486 X-ray source was used to scan the two fracture surfaces to determine the elemental composition of the delaminated surfaces within approximately the first 5 nm of the surface. This technique was used as the primary means to determine if the fractured surfaces failed due to adhesive or cohesive failure and the location within the sample.

CHAPTER 5

FRACTURE TOUGHNESS MEASUREMENTS OF MULTILAYER BARRIER FILMS

5.1. Overview

In this chapter, interfacial fracture toughness results for SiN_x−PMMA multilayer barrier films are presented. First four point bending results are presented for the as-made barrier films as described in Chapter 4. Next, modifications to the SiN_x-PMMA interface are performed to determine their impact on the strength of the interface. Corresponding changes in surface energy are measured and correlated to the changes in adhesive strength. XPS and AFM measurements are used to help determine the location of the fracture within the failed samples and verify adhesive or cohesive failures.

5.2. Interfacial Fracture Toughness of SiN_x−PMMA Interfaces

In order to determine the baseline value of the interfacial fracture toughness of the model SiN_x−PMMA interface, three separate sample batches amounting to a total of 39 samples were prepared and tested. The initial results summarized in Table 5.1 show that the interfacial fracture toughness (G_c) of the SiN_x−PMMA interface was 4.58 ± 0.85 J/m^2. Fig. 5.1(a) shows a delaminated sample during FPB tests and Fig. 5.1(b) describes the typical load vs. displacement response that was measured in this study. To determine the exact location of delamination, X-ray photoelectron spectroscopy (XPS) was used to

identify the elemental composition of the delaminated surfaces. Fig. 5.2 depicts the delaminated sample after FPB tests, and Fig. 5.3 and 5.4 show the XPS scans for the inorganic side (SiN_x, 100 nm) and the organic side (PMMA, 400 nm). As shown in Fig. 5.3 and 5.4, there is distinct evidence of a N1s peak (≈ 398.08 eV) on the inorganic side, while there is no N1s peak on the organic side. The XPS data therefore indicates that the delamination took place at the desired interface between SiN_x and PMMA, thus supporting the idea that the measured G_c value (4.58 ± 0.85 J/m^2) corresponds to the baseline interfacial fracture toughness of the model interface (SiN_x–PMMA).

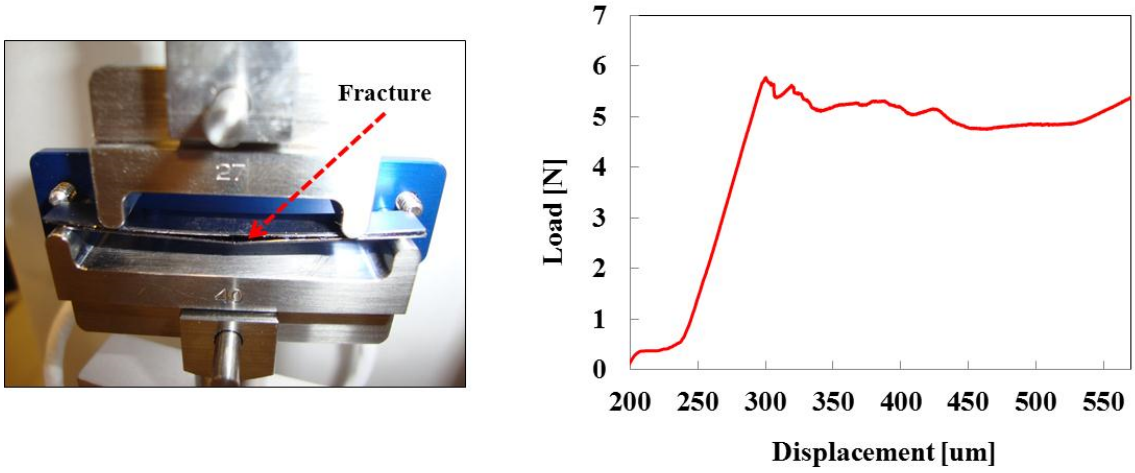

Figure 5.1. (a) Delaminated SiN_x–PMMA interface during four point bending tests and (b) a typical load vs. displacement curve obtained in this study.

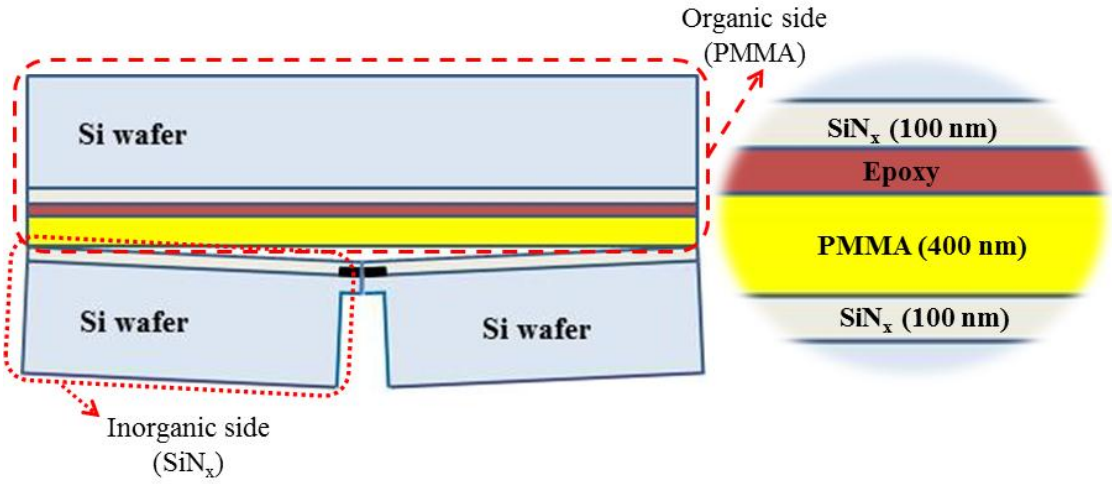

Figure 5.2. (a) Schematic diagram of the delamination in the model SiN_x–PMMA interface using the four point bending technique.

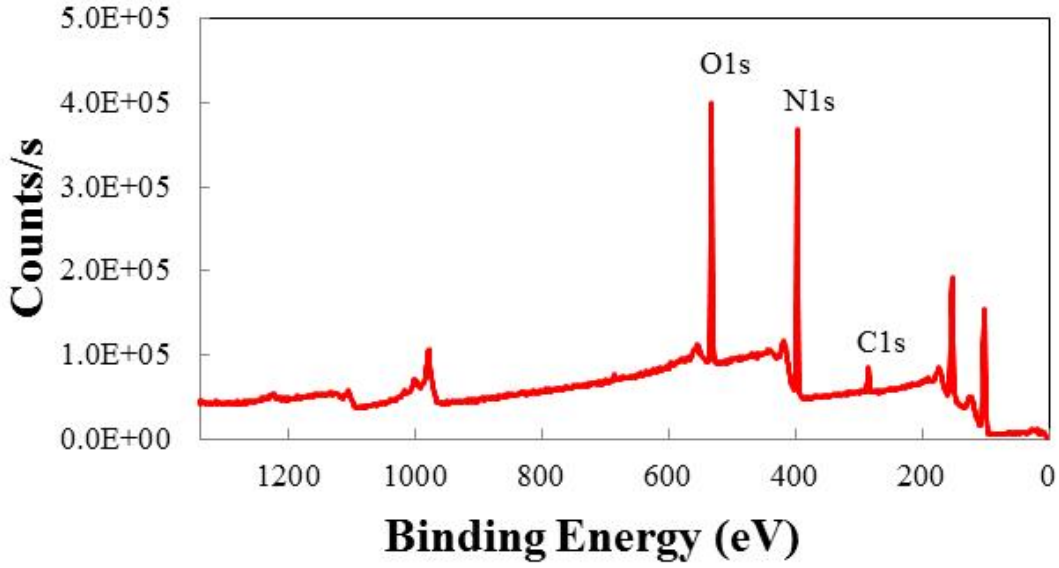

Figure 5.3. XPS scan of the inorganic side (Fig. 5.2) revealing the presence of SiN_x and the lack of any signature of PMMA on the surface.
+

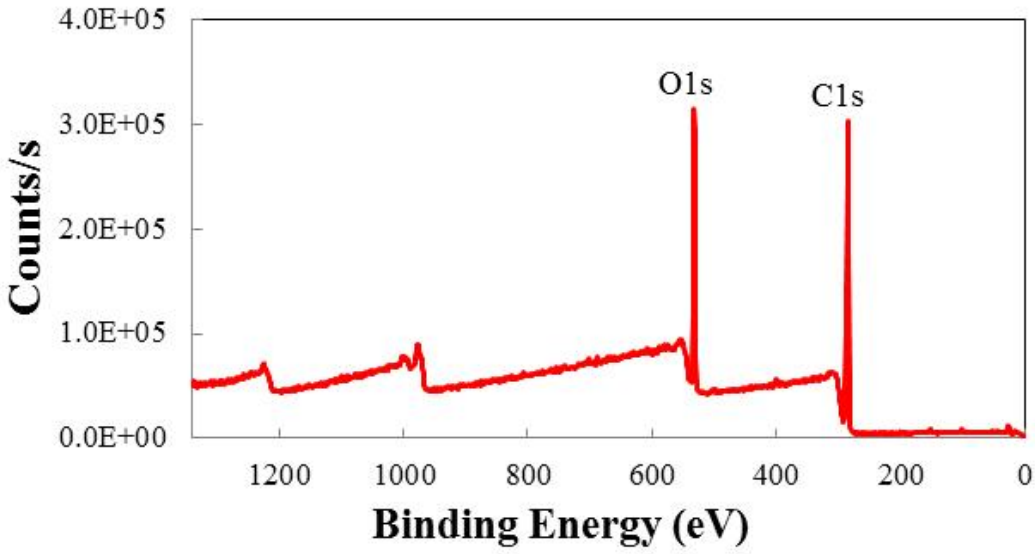

Figure 5.4. XPS scan for organic side (Fig. 5.2) revealing the presence of PMMA on the surface and the lack of SiN_x. This combined with Fig. 5.3 indicates that failure occurred at the interface between SiN_x and PMMA.

5.3. Adhesion Promotion with Secondary Bonding Mechanisms

5.3.1. Adhesion Promotion Using Oxygen Plasma Exposure

To explore the effect of the permanent dipole-dipole interactions which can possibly change interfacial adhesion, an oxygen plasma treatment system (Yes R1 Plasma Cleaner: 6 mins, O_2: 1.5 slm, and 700 W) was used to treat the SiN_x surface prior to bonding to PMMA. The O_2 plasma activation is expected to introduce polar hydroxyl groups onto the surfaces. Contact angle measurements yielding the polar and dispersive energy components of the surface energy were performed as described in chapter 4.5, as shown in Fig. 5.5. O_2 plasma treated SiN_x showed a 13.25 mJ/m^2 (total surface energy = 72.93 mJ/m^2) increase in its surface energy compared to bare SiN_x (total surface energy = 56.98.

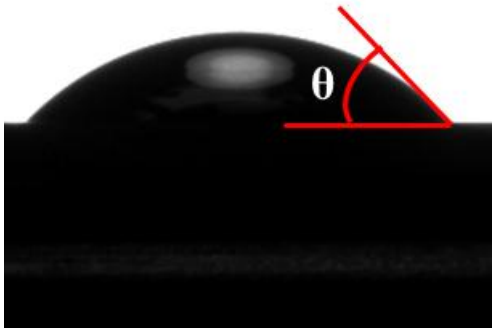

Figure 5.5. Example of the contact angle measurement of a DI water drop on SiN_x surface ($\theta = 46°$).

mJ/m^2). In particular, while there could be other mechanisms that can affect the adhesion strength in the model interface, it was observed that a higher polar component of surface energy being 42.20 mJ/m^2 was achieved when compared to only 27.56 mJ/m^2 for bare SiN_x Four point bending tests conducted on O_2 plasma activated SiN_x bonded to PMMA showed an increased adhesion strength of 9.44±1.15 J/m^2 compared to untreated SiN_x (4.58±0.85 J/m^2). The increase in measured G_c is consistent with the hypothesis that the increase in the polar component of the surface energy of the substrate leads to increased permanent dipole-dipole interactions between the substrate and the PMMA that are in general stronger than the instantaneous dipole-dipole interactions induced by the dispersive component of the surface energy [156], thus possibly enhancing the adhesion at the interface by causing the localized polymer plasticity at the crack tip [152].

5.3.2. Adhesion Promotion Using an Oxide Capping Layer

Modifications to the SiN_x surface was performed by depositing a metal oxide which can readily form hydroxyl groups when exposed to water vapor in the environment to increase the surface energy. While O_2 plasma activation of substrates improves

adhesion, the effects of the plasma activation will diminish over time if the bonding is not performed instantaneously. Hence, a more permanent method of increasing the surface polarity was explored through the deposition of a thin layer of Al_2O_3 on top of the SiN_x, as shown in Fig. 5.6. Since it is well known that a Al_2O_3 film using an atomic layer deposition (ALD) in general forms hydroxyl groups when exposed to the ambient environment [215], 10 nm of Al_2O_3 was deposited on top of the SiN_x surface to create more permanent interactions from its high polarity. An added advantage of depositing the Al_2O_3 layer is that it serves as a capping layer to the barrier and is expected to enhance its barrier performance by filling micro defects that exist in the SiN_x film, leading to lower water vapor transmission rate ($g/m^2/day$) [47]. To modify the SiN_x, a 10 nm thick layer of Al_2O_3 was deposited by atomic layer deposition (Savannah 100 ALD by Cambridge NanoTech). One growth cycle in the ALD system was comprised of sequential pulses of H_2O (15 ms pulse) and trimethylaluminum, TMA, (15 ms pulse) precursors injected into the ALD reactor utilizing nitrogen (5 seconds of purging) as a carrier gas at a temperature of 110°C. 100 cycles were performed to make 10 nm of Al_2O_3 capping layer as shown in Fig. 5.6.

Before conducting the FPB tests and surface energy analysis, bare SiN_x films and SiN_x films coated with 10 nm of Al_2O_3 were scanned by AFM to check its surface morphology. As shown in Fig. 5.7, there was a negligible change in surface roughness value (R_q, nm) from 0.4 nm for SiN_x surface to 0.3 nm for SiN_x coated with 10 nm of Al_2O_3 surface which can also be in an error range of AFM. Therefore, we assumed that the mechanical bonding due to the interlocking between the interfaces by adding the 10

nm of Al_2O_3 film should be negligible because the mechanical adhesion is mostly affected by the surface roughness [152].

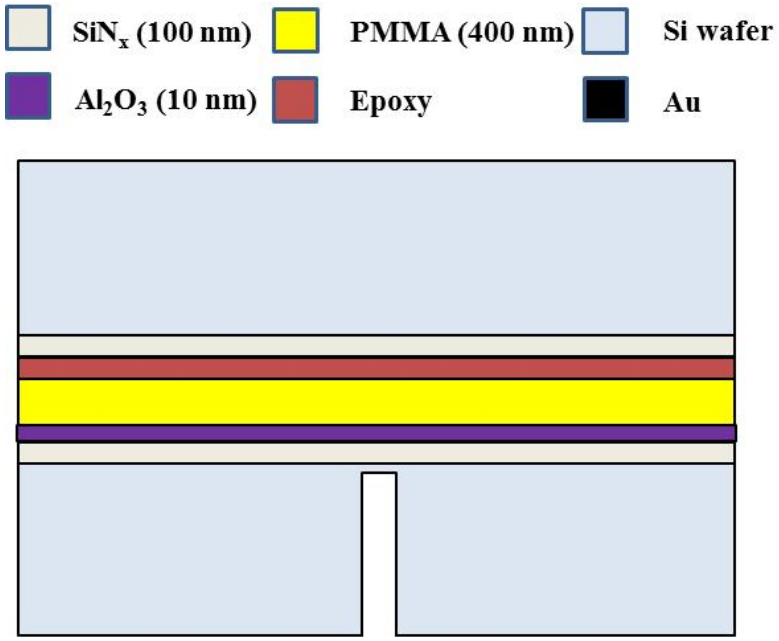

Figure 5.6. A schematic diagram for of SiN_x/Al_2O_3−PMMA sample structure.

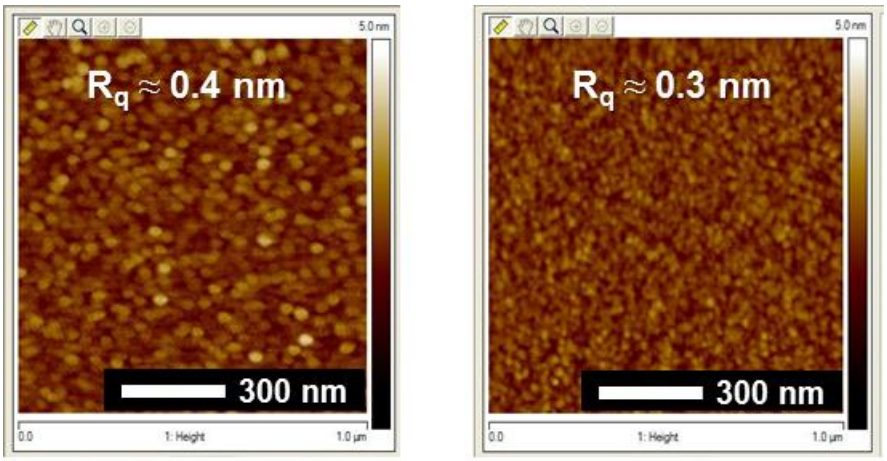

(a) (b)

Figure 5.7. Surface morphologies obtained by AFM scans of: (a) bare SiN_x (100 nm) and (b) SiN_x (100 nm) coated with 10 nm of Al_2O_3. The scans reveal that if there is any change in the adhesion strength using 10 nm of Al_2O_3 film, the change results from the modification of SiN_x surface with a hydrophilic Al_2O_3 film indicating the mechanical bonding due to the interlocking between the interfaces should be negligible.

Contact angle measurements were performed on the Al_2O_3 layer and showed an increase of 11.95 mJ/m^2 in the polar component of the surface energy over bare SiN_x while the dispersive components remain almost same, as shown in Table 5.1. Four point bending tests of the SiN_x/Al_2O_3−PMMA interface showed that the interfacial fracture toughness (G_c) increased to 7.72±0.62 J/m^2 with the addition of the 10 nm of Al_2O_3 capping layer without any additional treatments. XPS scans (Fig. 5.8 and Fig. 5.9) of the delaminated surfaces also determined that delamination occurred at the Al_2O_3 and PMMA interface demonstrating the effect of increased polarity on the interface bond strength.

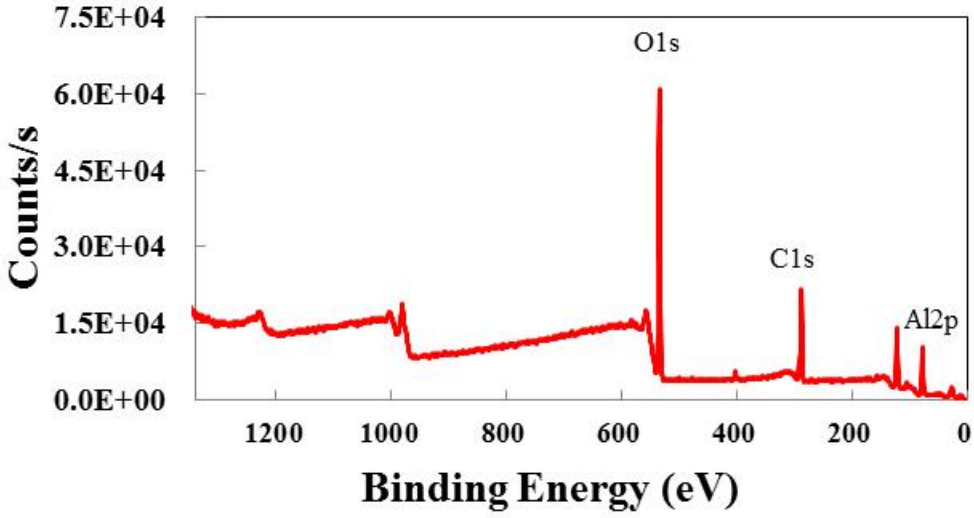

Figure. 5.8. XPS scan of inorganic side revealing the presence of Al_2O_3 by having Al2p (≈ 75.5 eV) and the lack of any signature of PMMA on the surface.

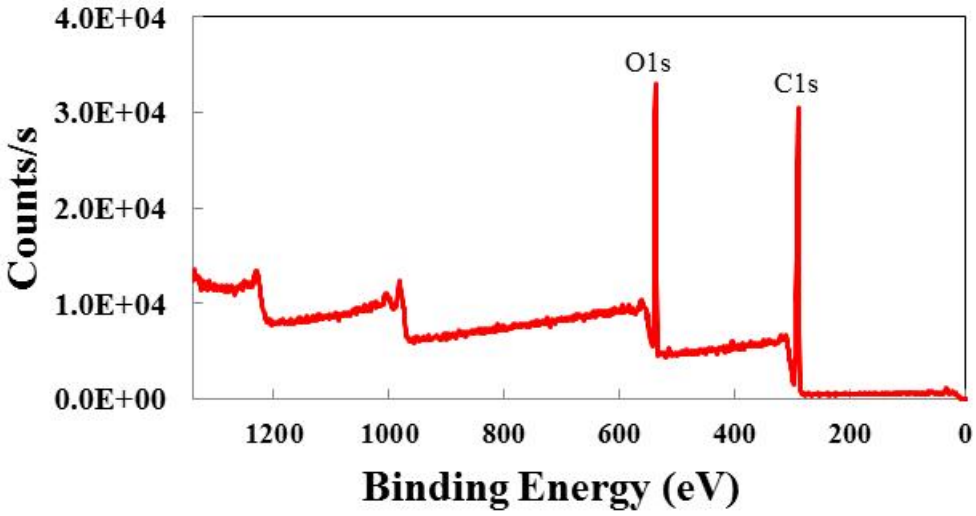

Figure 5.9. XPS scan for organic side revealing the presence of PMMA on the surface and the lack of Al_2O_3. This combined with Fig. 5.8 indicates that failure occurred at the interface between Al_2O_3 and PMMA.

While the increase in G_c by addition of the 10 nm thick Al_2O_3 capping layer was not as high as that of O_2 plasma treated SiN_x, it is still higher than the bare SiN_x–PMMA interface while also providing enhanced barrier performance as discussed earlier. The effect of further enhancing the polarity of the Al_2O_3 capped SiN_x on the interfacial adhesion strength was explored by O_2 plasma treatment of the Al_2O_3 layer. Contact angle measurements in the case of O_2 plasma activated SiN_x/Al_2O_3 surfaces were difficult due to the large polar component that led to a super hydrophilic surface. FPB tests conducted on O_2 plasma activated SiN_x/Al_2O_3 bonded to PMMA showed increased adhesion strength to 10.03±0.94 J/m^2 compared to 7.72±0.62 (J/m^2) obtained for untreated SiN_x/Al_2O_3–PMMA interface and similar to that of O_2 plasma activated uncapped SiN_x–PMMA interface (9.44±1.15 J/m^2).

Interfacial surface energy modification through increased polarity which is associated with atomic or molecular separation also produced changes in the crack tip

behavior at the model interface when compared to the unmodified interface. The load vs. displacement data for SiN_x/Al_2O_3−PMMA interface is shown in Fig. 5.10. This periodic hardening and softening in the load vs. displacement response originated from an energy dissipation effect at the crack tip during the FPB tests. When the crack propagates along the SiN_x/Al_2O_3−PMMA interface, it extends its plastic zone size by dissipating the energy at the crack tip and forming a crazing zone in the polymer layer. As the crazing zone develops and the polymer chains stretch, the material then hardens again until fracture of the crazing zone occurs allowing the crack to propagate. This is accompanied by a drop in the load and the process repeats itself as described in Fig. 5.10 and 11. Thus, the crack goes through periodic propagation and arrests modes during the fracture process. Evidence of this was also observed through atomic force microscope (AFM) scans of the delaminated region (Al_2O_3 side after FPB tests) in Fig. 5.12.

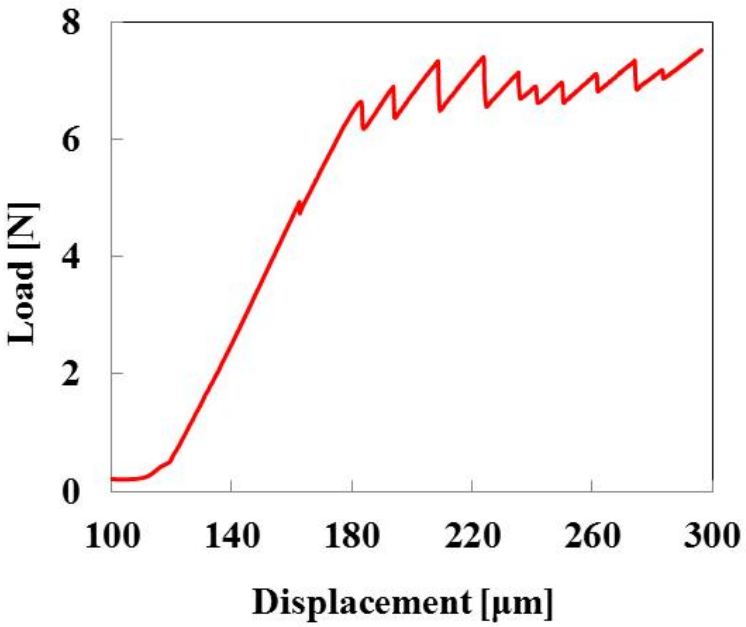

Figure 5.10. Load vs. displacement curve of SiN_x/Al_2O_3−PMMA sample.

The periodic pattern of the tearing of the PMMA layer that remains on the surface of the Al_2O_3 is indicative of this failure mode. In order to check the chemical compositions of the delaminated SiN_x/Al_2O_3−PMMA interface, the delaminated surface containing Al_2O_3 and partial PMMA strips were scanned using SEM (Fig. 5.13) and XPS (Fig. 5.14). Fig. 5.13 shows SEM images of SiN_x/Al_2O_3−PMMA interface after the FPB tests. In Fig. 5.13, point 1 mostly has PMMA (dark area in SEM image) while there is more Al_2O_3 (bright area in SEM image) at point 3. The chemical compositions of dark (PMMA) and bright (A_2O_3) areas in Fig. 5.14 were also checked with XPS using a "Al2p" peak, as shown in Fig. 5.14.

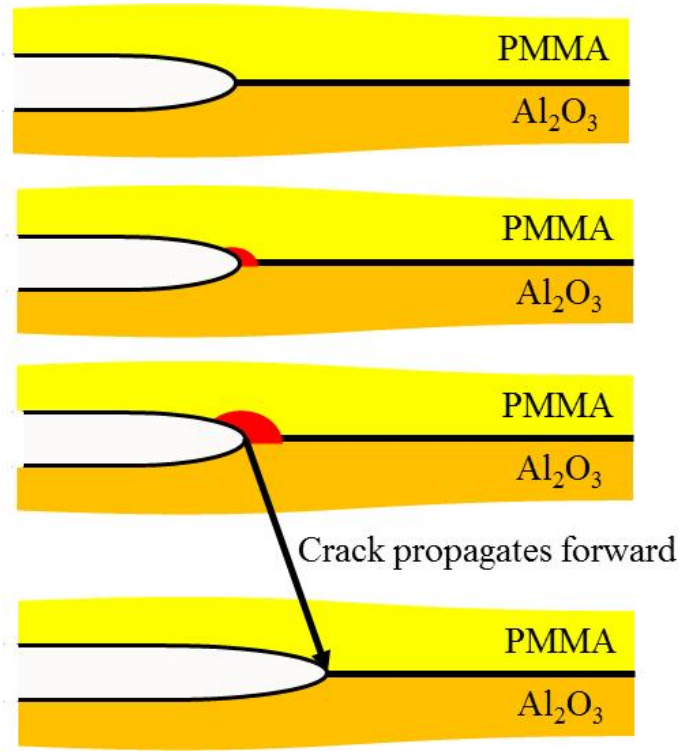

Figure 5.11. Crack propagation mechanism along the SiN_x/Al_2O_3−PMMA interface where the plastic zone extends into the PMMA causing crazing and failure due to the increased strength of the Al_2O_3/PMMA interface when compared to SiN_x/PMMA. As the crack starts and stops during the propagation, the load in the load-displacement trace oscillates due to the periodic crazing and fracture of the PMMA.

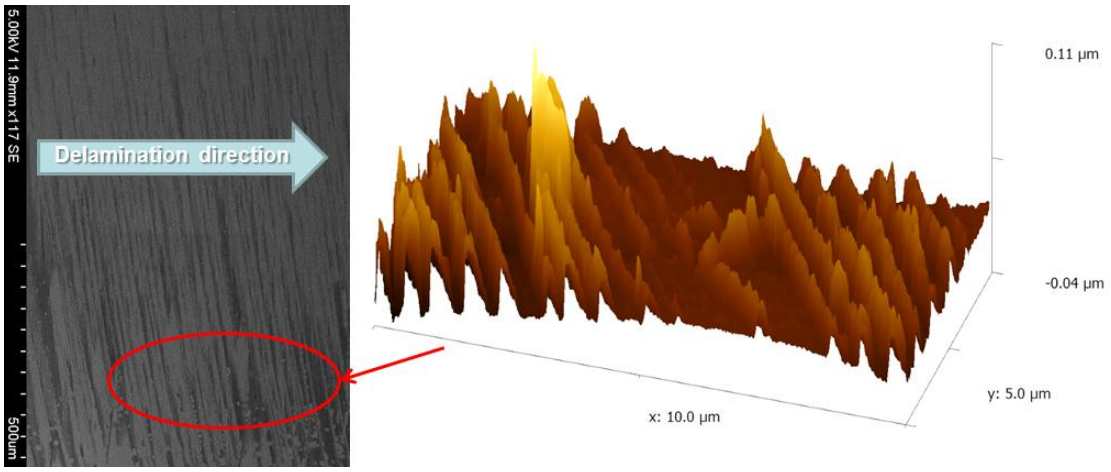

Figure 5.12. SEM image of the failed SiN_x/Al_2O_3−PMMA interface after the FPB test along with a three dimensional (3D) atomic force microscopy (AFM) scan showing the tearing pattern of the PMMA that occurs during the periodic crazing and crack propagation of the FPB test.

Figure 5.13. SEM image of SiN_x/Al_2O_3−PMMA interface after the FPB test with three different position containing different amount PMMA as strips (dark areas indicate PMMA).

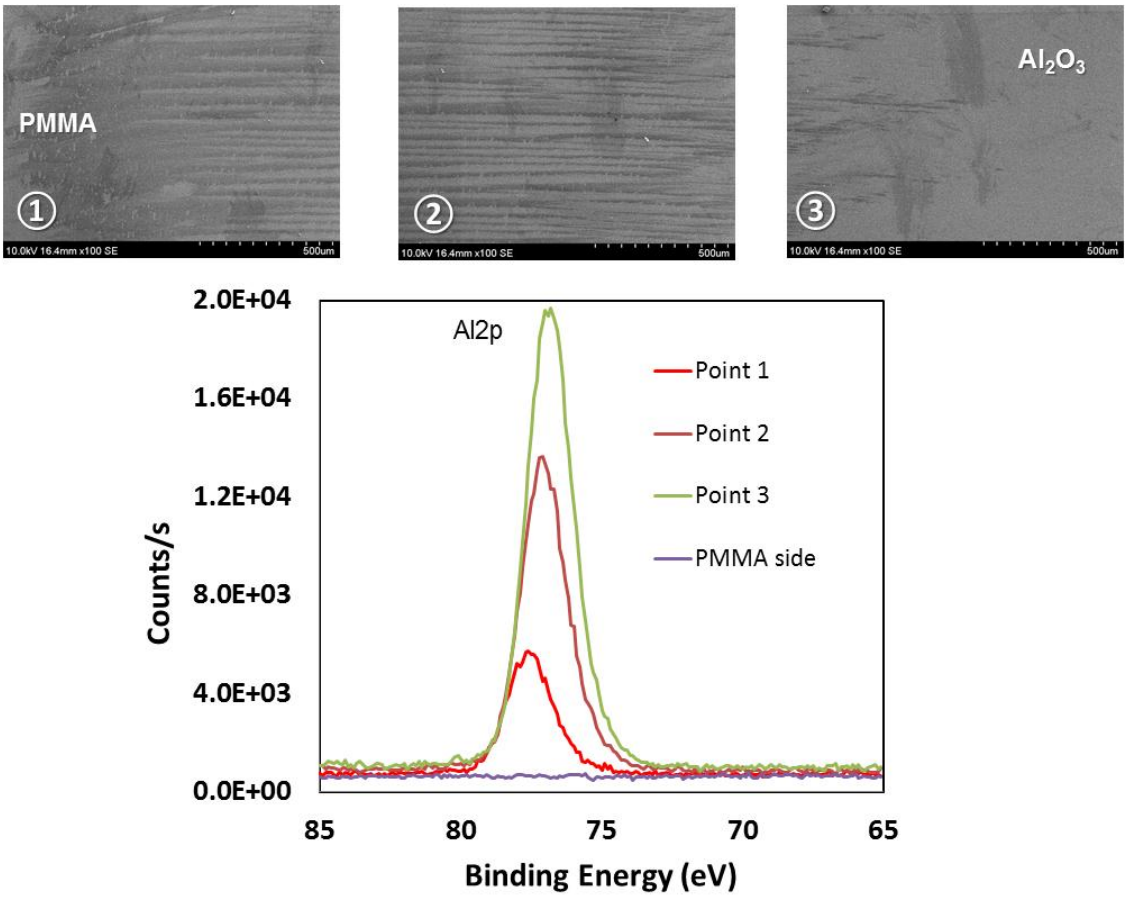

Figure 5.14. XPS scans for different delamination positions on SiN_x (100 nm)/Al_2O_3 (10 nm) surface containing partial PMMA strips.

5.3.3. Adhesion Promotion with Phosphonic Acids (PAs)

5.3.3.1. Phosphonic Acid Modification

Phosphonic acid modification of the interfaces in the model barrier film was carried out in collaboration with Prof. Seth Marder and Sergio Paniagua-Barrantes of the School of Chemistry and Biochemistry at the Georgia Institute of Technology. In order to vary the surface energy at the interface, phosphonic acids (PAs) with tail group variations were used. Phosphonic acid modification of the substrates consisted of

immersing the substrates in 10 mM solution of PA in ethanol for 1 hour at 75°C. Before dipping the substrates in the PA solution, the substrates were activated with a mild O_2 plasma system using an atmospheric pressure Surfx Atomflo TM 300 Series for 10 mins at 140 W. This plasma treatment was performed to remove carbonaceous contamination, and introduce hydroxyl groups that enabled the PA head group to covalently bond with the substrate [169, 171]. After immersion for one hour in the PA solution, the substrates were rinsed with ethanol followed by sonication in a solution of 5% (v/v) triethylamine in ethanol to remove any physisorbed PA molecules from the substrates. This process ensures that only covalently bonded PA molecules are left behind on the surface.

In this study, two types of PAs were used; 1) MCBPA (4-Methoxycarbonylbutyl phosphonic acid) and 2) ODPA (octadecyl phosphonic acid) as shown in Fig. 5.15. MCBPA ($C_6H_{13}O_5P$ with M. W. 196.14) and ODPA ($C_{18}H_{39}O_3P$ with M. W. 334.47) were purchased from Epsilon Chimie and Sigma-Aldrich, respectively.

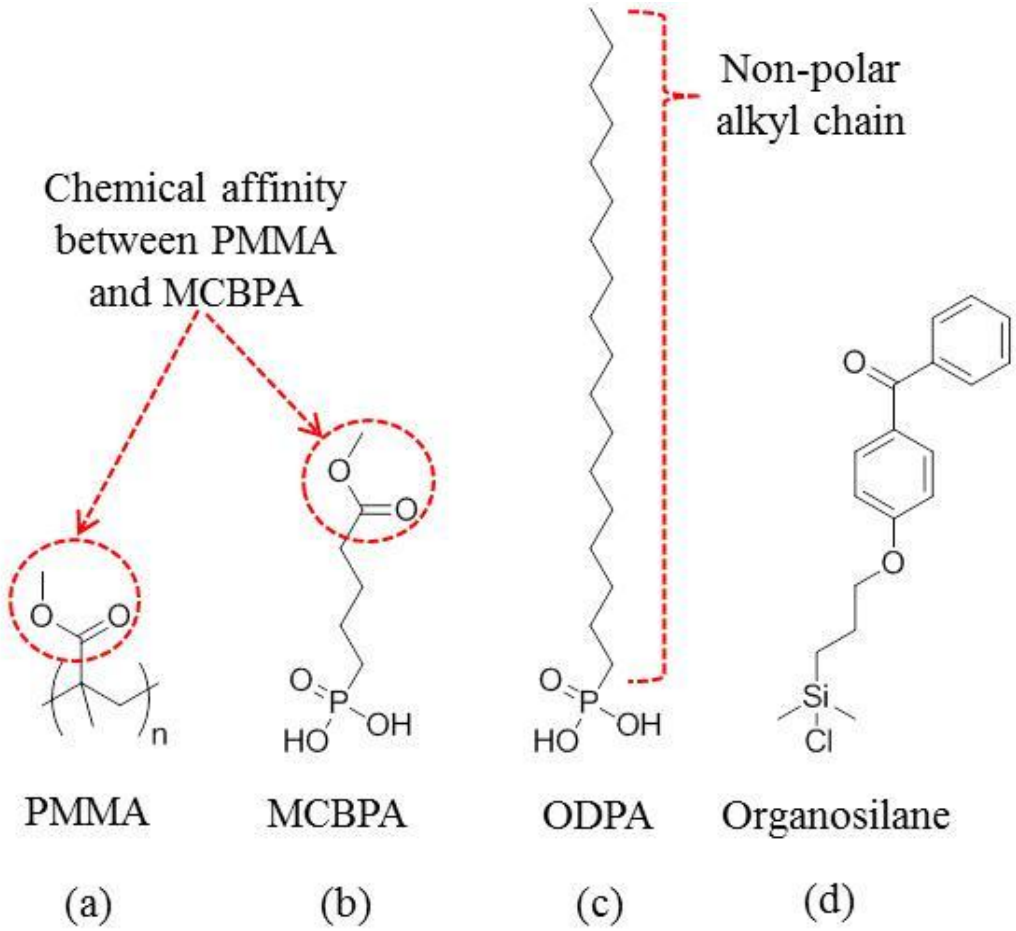

Figure 5.15. Structures of PMMA, phosphonic acids, and the silane based surface modifier used in this study: (a) PMMA, (b) MCBPA (4-methoxycarbonylbutyl phosphonic acid), (c) ODPA (octadecyl phosphonic acid), and (d) benzophenone derivative (4-(3′-chlorodimethylsilyl) propyloxybenzophenone silane).

5.3.3.2. PFBPA Verification on Inorganic Surfaces

In order to conduct surface modification of SiN_x using PAs, it was hypothesized that the previously discussed Al_2O_3 capped SiN_x would be required since PAs are typically used in the modification of metal oxides [169]. To confirm the bonding of PAs to SiN_x, pentafluorobenzyl phosphonic acids (PFBPA) were used as an initial test surface

modifier, as shown in Fig. 5.16. This particular molecule was chosen due to the large number of fluorine atoms present on the tail benzyl group. In cases where the PAs bonded, an intense F1s peak can be observed in the XPS spectrum, as previously reported [171]. In this study, it was found that XPS analysis of SiN_x surfaces after attempted PA modification (according to literature methods for metal oxides [171]) lacked the presence of any fluorine suggesting difficulty of PAs to directly modify SiN_x, as shown in Fig. 5.17. Therefore, in order to study the effect of PA surface modification on the interface adhesion, it was decided to conduct all investigations using the Al_2O_3 capped SiN_x. First, additional experiments were used to verify the ability of PFBPA to bond to the Al_2O_3 capping layer. From these experiments, it was clearly seen through XPS analysis that the F1s peak from PFBPA was present on the Al_2O_3 as shown in Fig. 5.17.

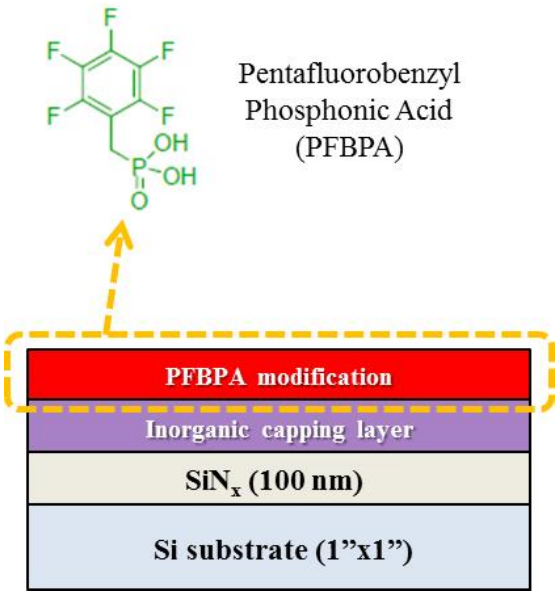

Figure 5.16. Schematic diagram of pentafluorobenzyl phosphonic acid (PFBPA) modification on SiN_x (100 nm) coated with 10 nm of inorganic capping layers (SiO_x and Al_2O_3).

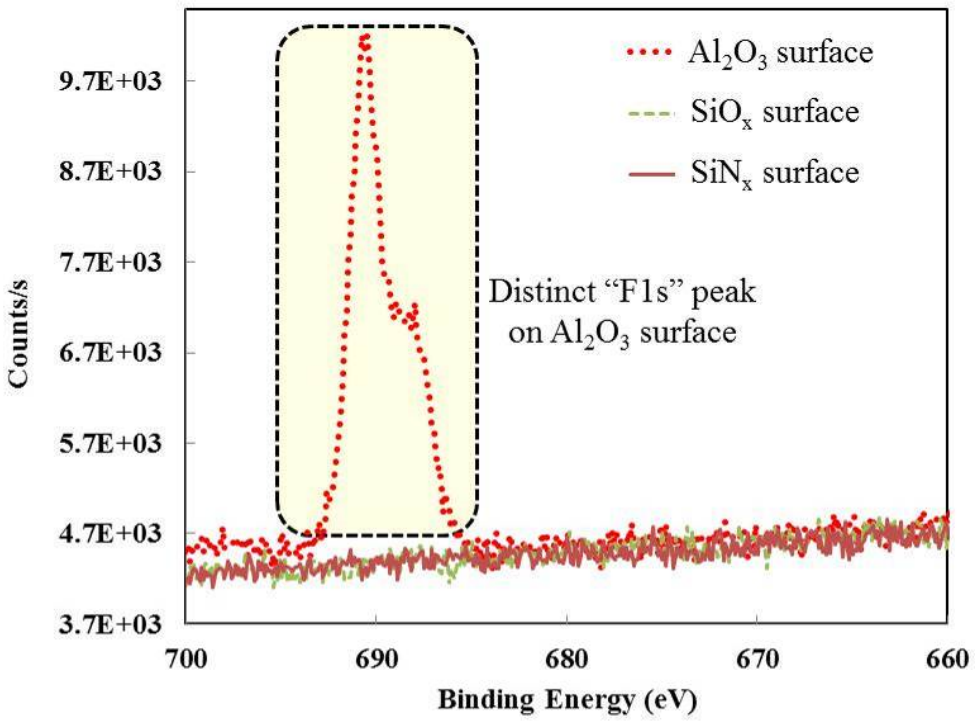

Figure 5.17. XPS scans of SiO_x, SiN_x, and Al_2O_3 surfaces after pentafluorobenzyl phosphonic acid (PFBPA) surface modifications.

5.3.3.3. Test Results with Phosphonic Acid Modification

Surface energy modification using PAs can be performed by varying the polarity of the tail group where a benzyl, fluorine or methyl terminating tail group commonly result in low polar energy component while amines or hydroxyl tail groups commonly result in increased polarity [169]. While phosphonic acids bind to the Al_2O_3 capped SiN_x through covalent bonds [47], the head group of the PAs is expected to bind to the PMMA through weak secondary bonds such as van der Waals forces. These two features of molecular interface modifiers as in the case of phosphonic acids provide us with two distinctive modes to modify the interfacial fracture strength; 1) by varying the polarity of the surface through suitable choice of the PA tail group and 2) through the chemical

affinity effect between the PMMA and the PA by matching the PA tail group to the PMMA.

For this experiment, two different PAs (MCBPA and ODPA) were identified based on the energy of the tail groups, as shown in Fig. 5.15. MCBPA (Fig. 5.15(b)) has the same tail group (methoxy group; O - CH_3 and carbonyl group; O = C) as PMMA and is therefore expected to produce a strong interface due to its chemical affinity with PMMA (shown in Fig. 5.15(a) and (b)). As expected, even though the polarity of the MCBPA modified SiN_x/Al_2O_3 surface (24.59 mJ/m^2) was similar to that of bare SiN_x surface (27.56 mJ/m^2), the interfacial fracture toughness increased almost by a factor of two (4.58 to 7.78 mJ/m^2) due to the chemical affinity between the PMMA and MCBPA that potentially enabled them to form a strong interface. However, the improvement in adhesion through the chemical affinity effect of SiN_x/Al_2O_3 and PMMA using MCBPA (7.78 mJ/m^2) was still lower than that measured with O_2 plasma activated Al_2O_3/SiN_x–PMMA interface (10.03 mJ/m^2) indicating that the polar component of the surface energy at the interface dominantly play a role to enhance the interfacial adhesion by inducing more permanent dipole interactions rather than the tail group matched interface that results in a weaker bond while there could be other factors that can also influence the fracture energy.

The second PA modifier, ODPA (OctaDecyl Phosphonic Acid, Fig. 5.15(c)) was chosen due to its low polarity (3.54 mJ/m^2). As expected, the ODPA modified surface weakened the interfacial fracture toughness, and was measured to be 0.84 mJ/m^2. The weak bond possibly resulted from the large number of instantaneous dipole-dipole interactions induced between the highly non-polar ODPA and the PMMA dominating the

interface strength and minimizing any contribution from the polar component of the surface energy.

Table 5.1. Impact of Surface Modifications on the Interfacial Fracture Toughness.

Structure	Interface modification (IM)	Total surface energy (γ^p) [mJ/m^2]	Dispersive component (γ^p) [mJ/m^2]	Polar component (γ^p) [mJ/m^2]	G_c [J/m^2]
SiN_x – PMMA	×	59.68±0.71	32.12	27.56	4.58±0.85
SiN_x – IM–PMMA	O_2 plasma treatment	72.93±0.37	29.74	42.20	9.44±1.15
SiN_x – Al_2O_3 – PMMA	×	71.39±1.85	31.88	39.51	7.72±0.62
SiN_x – Al_2O_3 – IM–PMMA	O_2 plasma treatment	–	–	–	10.03±0.94
SiN_x – Al_2O_3 – IM–PMMA	MCBPA	56.96±0.68	32.37	24.59	7.78±0.73
SiN_x – Al_2O_3 – IM–PMMA	ODPA	33.30±0.10	29.76	3.54	0.84±0.27

5.4. Adhesion Promotion with Primary Bonding Mechanism

5.4.1. Chlorosilane Modification

Benzophenone derivatized organosilanes, which have been discussed to form strong covalent bonds at SiN_x-PMMA interfaces [216-218], were used in this study. In particular, a monochlorosilane (4-(3′-chlorodimethylsilyl) propyloxybenzophenone silane), as shown in Fig. 5.15(d), was chosen in order to avoid the homocondensation reactions. This silane was synthesized (in collaboration with Prof. Seth Marder and Anthony Giordano of the School of Chemistry and Biochemistry, Georgia Institute of

Technology) in a manner similar to that reported in the literature [219] and used instead of benzophenone containing phosphonic acid since PAs will not covalently bind with bare SiN_x as was already explained in 5.3.3.2. In the case of the silane, the SiN_x surface was treated for 3 minutes with oxygen plasma followed by immediate immersion in a toluene solution containing the benozophenone silane (15 mM) under a flow of nitrogen. Several drops of anhydrous triethylamine (0.5 mL) was added in an effort to promote the binding based on previous reports in the literature [220] and the substrate was allowed to remain in solution overnight. Following overnight modification, the surface was rinsed with chloroform and dried under a flow of nitrogen. In order to initiate the photochemical reactions between bezophenone derivatives and PMMA, 400 nm of PMMA was spin-cast on the silane soaked SiN_x surface followed by UV exposure (Stratagene UV Stratalinker 2400, 60 minutes, 300 nm irradiation and a Rayonet RPR-100 photoreactor, 45 minutes, 350 ± 50 nm irradiation, Fig. 5.18) in a similar manner to what has been reported, previously [152, 219].

(a) (b)

Figure 5.18. UV exposure to initiate the photochemical reactions between bezophenone derivatives and PMMA using: (a) Stratagene UV Stratalinker 2400 (60 minutes, 300 nm irradiation) and (b) Rayonet RPR-100 photoreactor (45 minutes, 350 ± 50 nm irradiation).

5.4.2. Test Results with Chlorosilane Modification

Results from FPB tests for the benzophenone silane treatment of the SiN_x−PMMA interface show that the interfacial fracture toughness increased by a factor of five compared to that of the unmodified SiN_x−PMMA interface (27.78 ± 2.83 J/m^2, 4.58 ± 0.85, respectively). This enhancement in the interfacial fracture toughness is likely due to the strong covalent bonds between the benzophenone tail group attached to the organosilane and PMMA through photochemical reactions initiated by irradiation with UV light [219, 221]. To verify where the delamination happened after the FPB tests, a high resolution XPS scan of a "C1s" peak was used to check a C = O bond (≈ 288.6 eV in Fig. 5.19) [173] which is a component of PMMA film, as shown in Fig. 5.15. Thus, if both surfaces after the FPB tests have C = O bonds (≈ 288.6 eV) [173], it will indicate

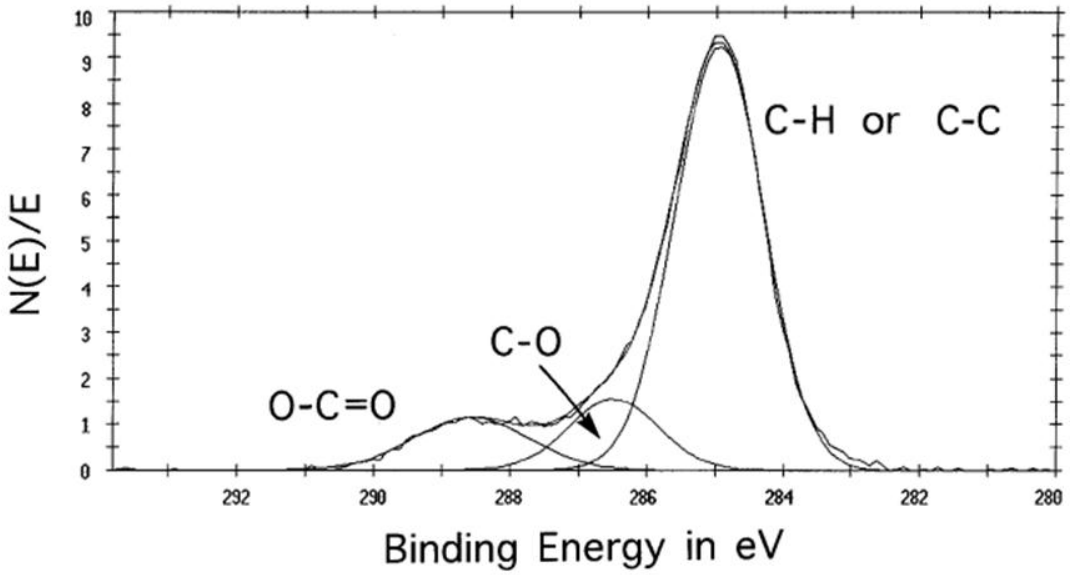

Figure 5.19. High resolution XPS scans of "C1s" peak for an as-received aluminum substrate [173].

that the failure took place in the PMMA layer because other films except for PMMA should not have C = O bonds.

High resolution XPS scans show that both delaminated surfaces have C = O bonds (≈ 288.6 eV), as shown in Fig. 5.20 and 5.21 indicating that the delamination happened in PMMA layer which enhanced the interfacial fracture toughness by having more energy dissipation effect during the FPB tests. In conclusion, among the three chemical surface modification methods explored in this dissertation, the benzophenone silane treatment produced the largest enhancement in interfacial fracture strength for a constant PMMA thickness of 400 nm. As discussed in section 5.3.3.2, the choice of organosilane treatment of the interface was driven by the fact that PAs will not covalently bond to a bare SiN_x surface. However, based on the current results, the modification time required for a PA versus a chlorosilane (that we used in this study) is much shorter (a few

minutes for PAs vs. 24 hours modification for silanes) and PA modification shows better long term shelf stability compared to organosilanes [152, 167, 168] which make them more attractive for barrier applications. Moreover, the use of the Al_2O_3 capping layer to enable the PA modification of the SiN_x surface will also lead to lower water vapor transmission rate ($g/m^2/day$) [47], as discussed in section 5.3.2. While surface treatment utilizing the benzophenone silane provided the largest G_c value, the more complicated methodology compared with that of O_2 plasma activated SiN_x/Al_2O_3−PMMA makes it less appealing, particularly after considering that O_2 plasma treated interface on its own produces adhesion strength as high as 10.03 ± 0.94 J/m^2. Thus, further research is needed on rapid deposition of benzophenone derived interface modifiers in order to enable their integration in barrier film manufacturing.

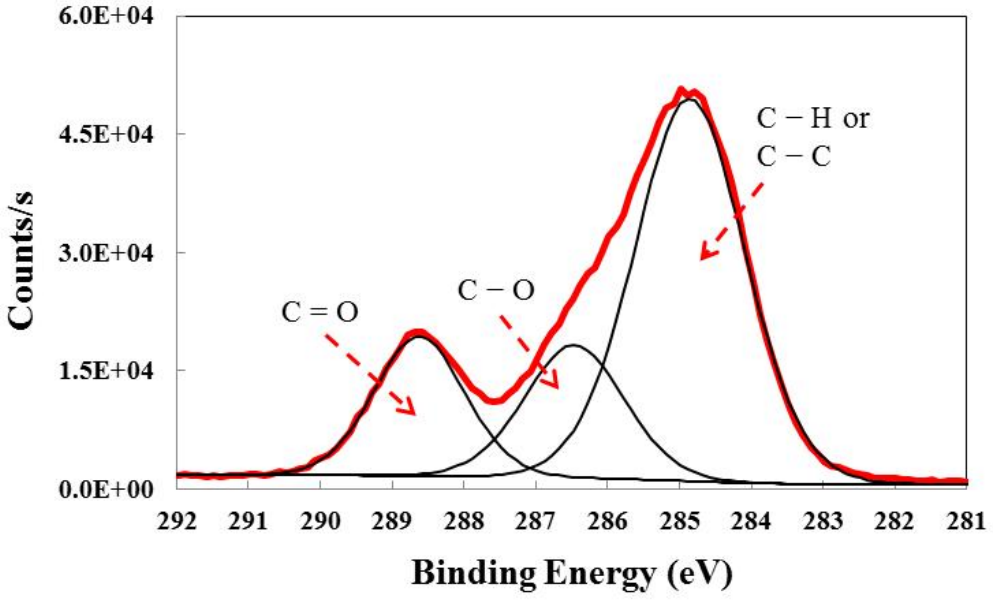

Figure 5.20. High resolution XPS scan for organic side containing PMMA film.

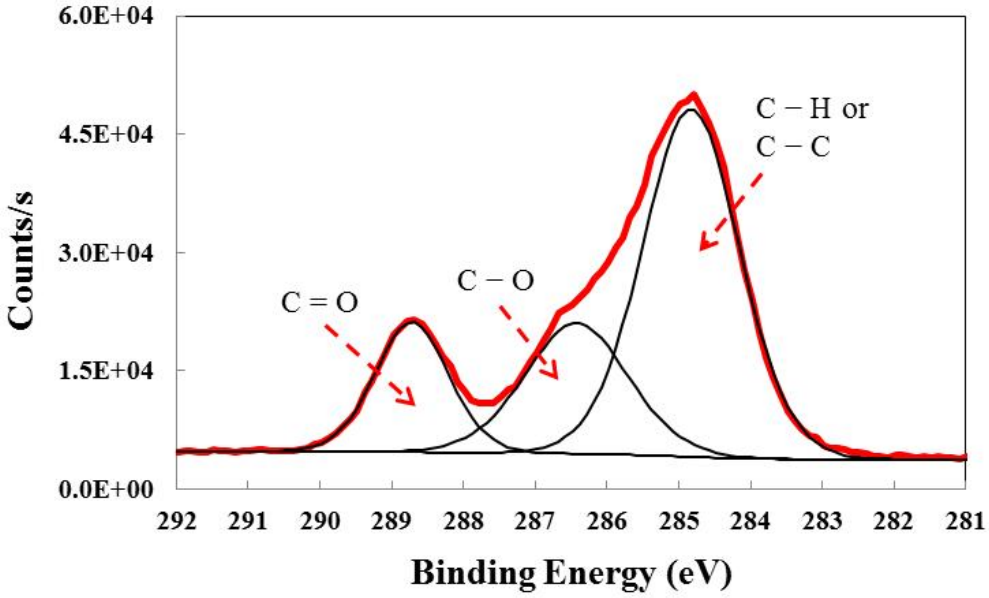

Figure 5.21. High resolution XPS scan for inorganic side containing SiN_x film.

5.5. Effect of PMMA Thickness on Interfacial Fracture Toughness

Previous research with poly(arylene)ether (PAE), showed that the plastic zone size can be constrained by two stiff elastic layers in a sandwich structure such as the one used in this study and this strongly influences the interfacial fracture toughness (Fig. 5.22) [67]. Thus, the cohesive strength of PAE increases by having a thicker polymer layer due to the increased energy dissipation in the polymer [67]. In our model SiN_x–PMMA structure, the plastic zone size is also constrained by the thickness of the PMMA layer (400 nm) that is sandwiched between the stiff Si substrates as shown in Fig. 5.1. To further investigate the effect of energy dissipation at the crack tip as a function of plastic zone size, three different SiN_x–PMMA interfaces with 120 nm, 400 nm (original

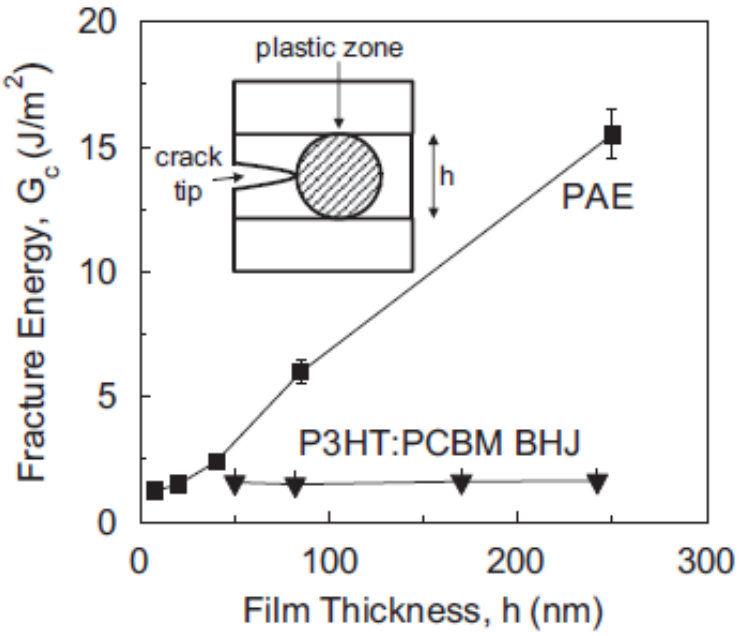

Figure 5.22. Thickness dependence of P3HT:PCBM OPV device and poly(arylene) ether (PAE) on cohesive fracture energy [67].

PMMA thickness), and 2.16 μm of PMMA layers were fabricated, and tested using four point bending tests. The results are summarized in Table 5.2, and show that the interfacial fracture toughness of the SiN_x-PMMA interface was enhanced from 1.47 ± 0.43 J/m^2 in the case of the 120 nm thick PMMA to 13.12 ± 0.66 J/m^2 in the case of the 2.16 μm of PMMA. While the theoretical plastic zone size of the PMMA layer is approximately 33 μm for a bulk thick sample and is significantly thicker than our entire FPB structure, it is clear that a thickness dependence should be expected due to the constraint effect. By increasing the PMMA thickness in this work, the interfacial fracture strength is enhanced by almost three times compared to our model structure just by reducing the constraint plastic zone at the crack tip obtained by increasing the thickness of the PMMA layer. It should be noted that it is not clear what impact the thickness will have on the overall

barrier performance. It is expected that the lag time from transient permeation will increase with increasing polymer layer thickness since it will take longer to reach equilibrium conditions. However, the steady state WVTR is expected to be controlled by the inorganic layers and thus, is not expected to change much for small the thickness range given here.

Table 5.2. Impact of PMMA Thickness on Interfacial Fracture Toughness.

Thickness of PMMA	Interfacial Fracture Toughness [J/m^2]
120 nm	1.47±0.43
400 nm	4.58±0.86
2.16 μm	13.12±0.66

5.6. Summary

The various factors affecting interfacial fracture toughness of a model SiN_x−PMMA interface were studied and quantified using a four point bending technique. As the one of the potential factors that alters the adhesion strength, the effect of surface energy modification at the interface was studied through the introduction of polar capping layers and O_2 plasma activation where the adhesion strength of the SiN_x−PMMA interface was almost doubled from 4.58 J/m^2 (SiN_x−PMMA) to 10.03 J/m^2 (SiN_x/Al_2O_3−PMMA) through increased surface polarity. Phosphonic acids with various tail groups were also used to chemically treat the interface to have both chemical affinity as well as to further investigate the importance of surface polarity at the interface. While

the chemical affinity of the two contact materials at the interface enhanced the adhesion strength to 7.78 mJ/m^2, we found the consistent result proposing the polar energy of the surface energy dominantly affects interfacial fracture toughness by enabling strong permanent dipole-dipole interactions as observed by the large improvement in adhesion obtained in the case of O_2 plasma treated substrates (10.03 mJ/m^2) while there could be other factors influencing the adhesion strength. The use of benzophenone, which has been shown to produce strong covalent bonds with polymer overlayers [219], at the model interface resulted in a five times enhancement of adhesion strength. However, even though this type of surface treatment maximized the adhesion strength, it would not be the ideal candidate for barrier applications due to its more complex and lengthy processing conditions. Additionally, interfacial adhesion was also increased through mechanical modification of the structure where the plastic zone size at the crack tip was varied by changing the thickness of the PMMA layer and found to increase the fracture toughness by three times. Overall, this chapter shows that increasing the polarity of the interface through surface treatments and increasing the plastic zone size are effective in enhancing the interfacial adhesion strength and reliability of hybrid organic-inorganic barrier layers while ensuring the integrity of the barrier.

CHAPTER 6

INTERFACIAL FRACTURE TOUGHNESS OF INVERTED OPV DEVICES

6.1. Overview

To address the lack of fundamental and quantitative information about the adhesive/cohesive strength in inverted OPVs, a study of the interfacial fracture toughness using an inverted OPV is presented. Inverted OPVs using both PDBTTT-C:$PC_{60}BM$ and P3HT:$PC_{61}BM$ are tested using the double cantilever beam technique to determine the weakest interfaces/layers with a quantitative adhesion strength value. For the structures tested, power conversion efficiencies are known from tests on separate samples. Interface modifications are then introduced to determine its impacts on interfacial strength. Chemical characterization of the failed samples is performed using XPS which helped to identify the failure location in the structure. Methods to improve the interfacial strength for polymer contacts consisting of PEDOT:PSS to PBDTTT-C:PCBM active layer are finally discussed.

6.2. Adhesion in OPVs with P3HT:PCBM Active Layers

Conventional organic photovoltaics utilize a low work function metal as an electron collecting electrode can easily be oxidized in air which is a major factor contributing to their limited environmental stability [9, 51, 65, 79, 81, 246]. To address this degradation issue of conventional OPV structures, inverted organic solar cells insert

a hole-blocking layer (e.g., ZnO, PEIE, Al_2O_3, TiO_2, etc.) [23, 209, 222] between the ITO and the active layer allowing the electrons to reach the ITO and additional high work function materials (PEDOT:PSS, MoO_x, NiO_3, etc.) [56-60] are placed in the back electrode to collect the holes, as shown in Fig. 1.5. As a result, these inverted structures become more air stable (Fig. 1.9(b)) [223], but limited information about their mechanical reliability exists. Therefore, in order to investigate the mechanical behavior of inverted OPVs, the most widely used active layer (P3HT:PC_{61}BM, PCE < 4% [25, 30, 208, 210-212]) was first used to fabricate samples and determine the mechanical strength of the weakest interfaces/layers.

A test structure consisting of Si substrate, SiO_x (300 nm), ZnO (40 nm), active layer (P3HT:PC_{61}BM in 1:1.5 wt%, 250 nm), Plexcore OC XA-1871™ (50 nm), Ag (100 nm), epoxy (1 μm), and SiO_x (300 nm), and Si substructure was fabricated to make DCB samples, as shown in Fig. 4.14 and outlined in detail in Chapter 4 while NREL (National Renewable Energy Laboratory) recently reported 3.5% PCE using this inverted OPV structure. In order to determine the interfacial fracture toughness, 2 separate sample batches were made which provided 18 individual DCB samples. The DCB fracture measurements with the P3HT:PC_{61}BM (1:1.5 wt%) based inverted solar cell show that the failure occurs at the interface between the active layer and PEDOT:PSS based Plexcore material reporting a very low G_c value (0.18 ± 0.15 J/m^2). This low interfacial fracture toughness indicates that the hydrophobic P3HT:PC_{61}BM active layer and negatively charged PEDOT:PSS polymer forms the weakest interface [11]. In order to verify where the delamination took place during the DCB tests, the delaminated interfaces were examined using high resolution scans in a XPS. To distinguish between

the P3HT:PC_{61}BM active layer and the PEDOT:PSS contact, the shape of the S2p was used. The P3HT:PC_{61}BM BHJ active layer has only one narrow S2p peak at 164 eV (Fig. 6.1(a)) and while the PEDOT:PSS base material has two S2p peaks at 164 eV and 168 eV (Fig. 6.1(b)) [22, 224, 225]. Our high resolution XPS scans after the fracture tests revealed that one side of the sample contained only one S2p peak (Fig. 6.2(c) indicating P3HT:PC_{61}BM BHJ active layer) and the other side had two S2p peaks (Fig. 6.2(a) indicating PEDOT:PSS based Plexcore material) which infers that the interfacial failure occured at the interface between the P3HT:PC_{61}BM active layer and PEDOT:PSS Plexcore material.

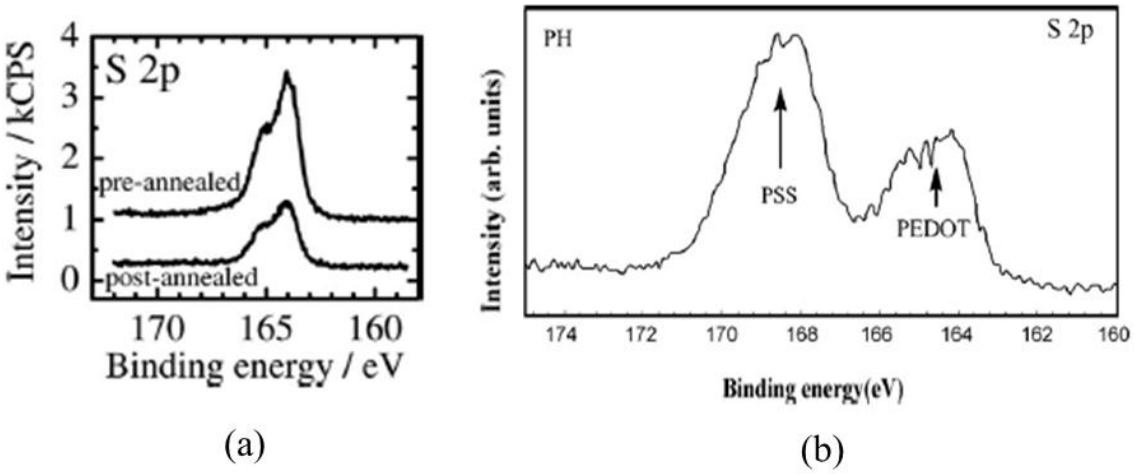

Figure 6.1. XPS (S2p) spectra from high resolution scans of: (a) P3HT:PCBM based film and (b) PEDOT:PSS film [22, 224, 225].

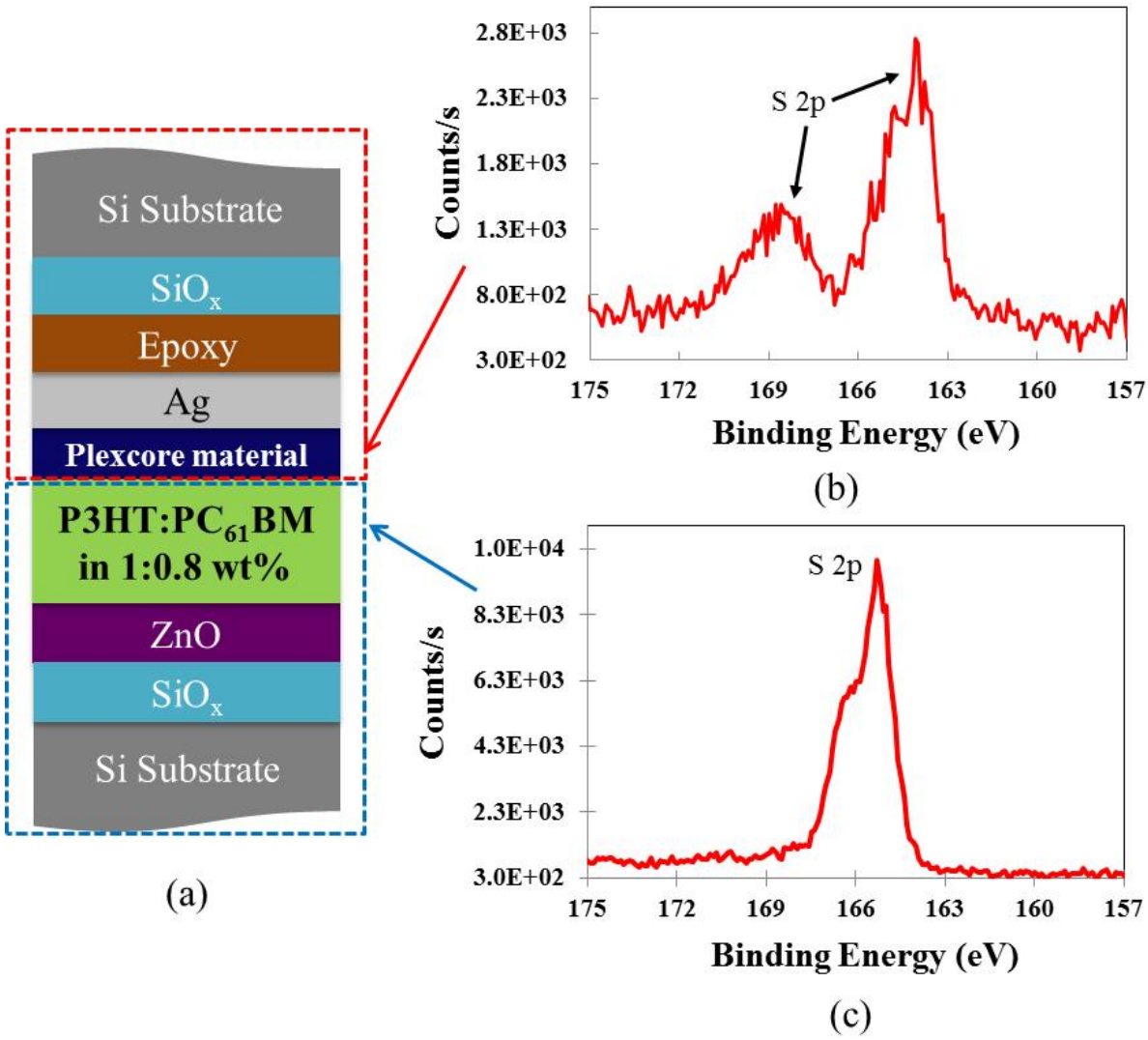

Figure 6.2. (a) Schematic diagram of DCB structure composed of Si substrate, SiO_x (300 nm), ZnO (40 nm), active layer (P3HT:PC_{61}BM in 1:1.5 wt%, 250 nm), Plexcore material (50 nm), Ag (100 nm), epoxy (1 μm), and SiO_x (300 nm), and Si substructure, (b) a high resolution XPS scan of the delaminated surface which has PEDOT:PSS based Plexcore material verified by using two "S2p" peaks, and (c) a high resolution XPS scan of the delaminated surface which has P3HT:PC_{61}BM BHJ active layer verified by using one "S2p" peak.

Another P3HT:PC_{61}BM based inverted OPV structure using MoO_x (PCE ≈ 3.5%) for a hole collecting contact was tested. Two different sample batches leading to 18 individual samples were fabricated consisting of Si substrate, SiO_x (300 nm), ZnO (40 nm), active layer (P3HT:PC_{61}BM in 1:1.5 wt%, 250 nm), MoO_x (10 nm), Ag (100 nm), epoxy (1 μm), and SiO_x (300 nm), and Si substructure, as shown in Fig. 4.14. Unlike the structure (Fig. 6.2(a)) using the PEDOT:PSS, the failure occurred in the P3HT:PC_{61}BM BHJ active layer when MoO_x hole collecting contact was used which resulted in a higher G_c value (0.39 ± 0.09 J/m^2). The failure location was verified using high resolution scans of XPS with S2p peaks at 164 eV, as shown in Fig. 6.3(b) and (c). While both delaminated surfaces have S2p peaks indicating that the failure occurred in the P3HT:PC_{61}BM layer, Mo3d peaks (232 eV for $Mo3d_{5/2}$ and 235 eV for $Mo3d_{3/2}$) were detectable on the upper side of inverted OPV samples (Fig. 6.4(b)) while the other side does not have peaks representative of any other layer in the device(Fig. 6.4(b)). This high resolution XPS scan infers that the cohesive failure took place in the upper side of the P3HT:PC_{61}BM layer near the MoO_x layer by considering the average measurement scan depth of XPS which is around 10 nm. This can be possible considering that the PCBM can phase separate as well as have a vertical gradient resulting in a gradient in mechanical properties along the active layer. Thus, if the top portion of the device is P3HT rich, the adhesive strength is expected to drop and thus may lead to this failure location.

Recently Dauskardt and colleagues [11] also presented results on a similar OPV structure involving P3HT:PCBM. They produced the facture toughness data by changing the composition ratio of P3HT:PCBM active layer and annealing the structures which

also proves that the failure occurs at the interface between the P3HT:$PC_{61}BM$ BHJ active layer and PEDOT:PSS layer while the interfacial fracture toughness data ranges in the similar region with our measured data. Combined with the investigation in this dissertation, these data clearly show that a weak link exists at the interface of P3HT:PCBM and PEDOT:PSS hole collecting contacts in OPVs.

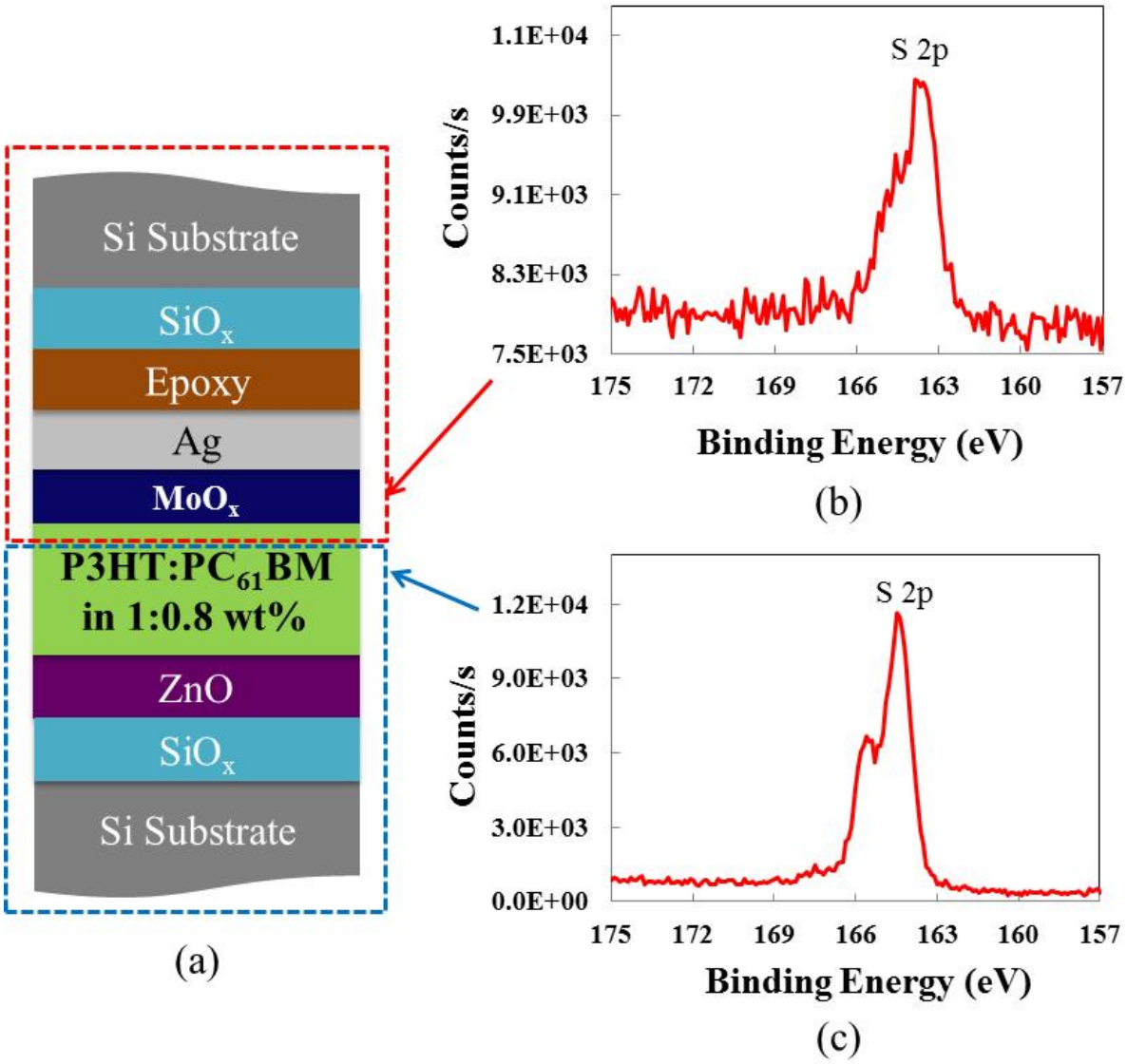

Figure 6.3. (a) Schematic diagram of DCB structure composed of Si substrate, SiO_x (300 nm), ZnO (40 nm), active layer (P3HT:$PC_{61}BM$ in 1:1.5 wt%, 250 nm), MoO_x (10 nm), Ag (100 nm), epoxy (1 μm), and SiO_x (300 nm), and Si substructure and (b) and (c) high resolution XPS scans of the delaminated surfaces which have P3HT:$PC_{61}BM$ BHJ

active layer verified by using "S2p" peak (164 eV) indicating the failure occurred in the active layer.

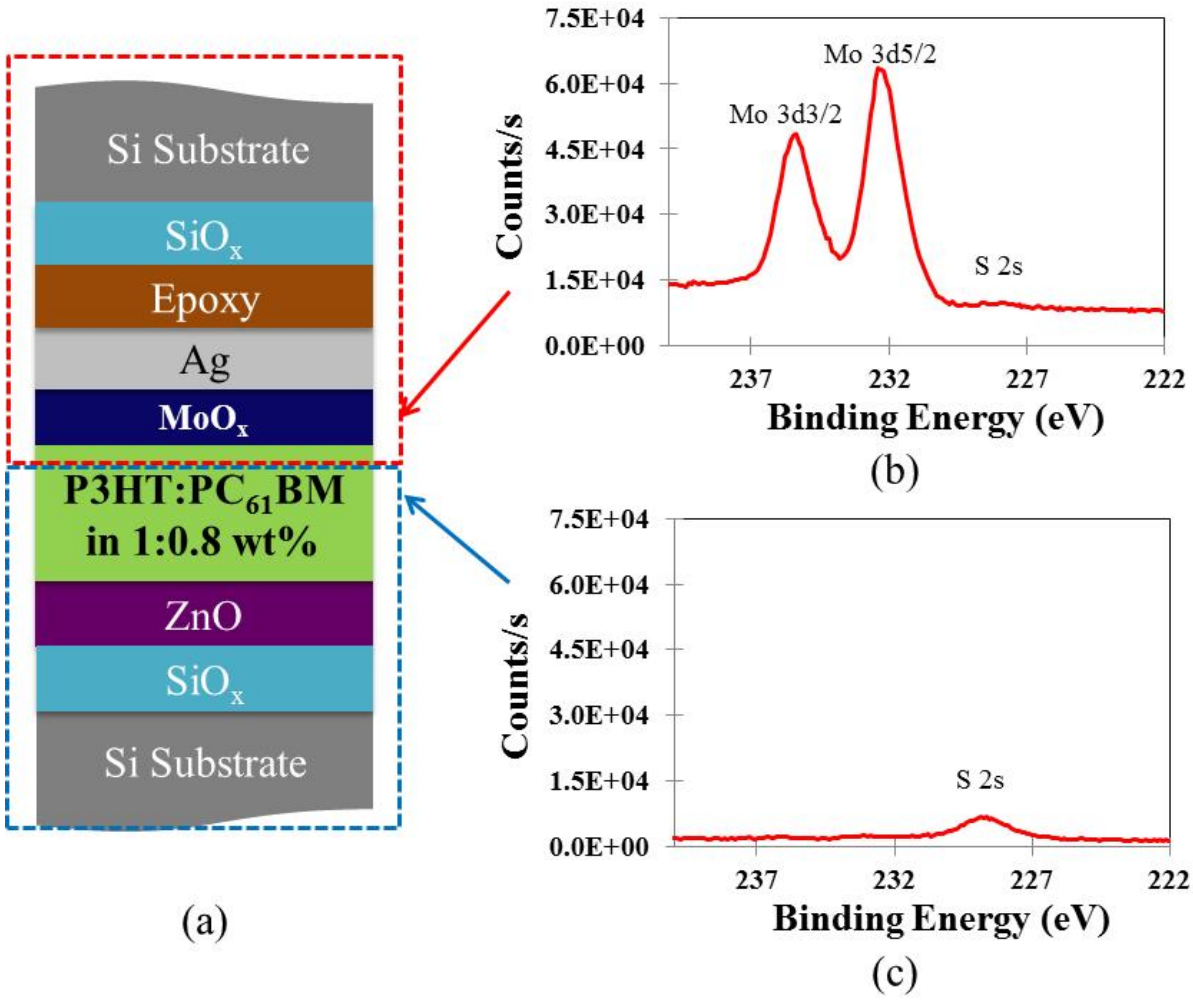

Figure 6.4. (a) Schematic diagram of DCB structure composed of Si substrate, SiO_x (300 nm), ZnO (40 nm), active layer (P3HT:PC_{61}BM in 1:1.5 wt%, 250 nm), MoO_x (10 nm), Ag (100 nm), epoxy (1 μm), and SiO_x (300 nm), and Si substructure, (b) a high resolution XPS scan of the delaminated surface which has partial P3HT:PC_{61}BM BHJ active layer and MoO_x verified by using "Mo3d" peaks, and (c) a high resolution XPS scans of P3HT:PC_{61}BM BHJ active layer that does not have "Mo3d" peaks indicating that the cohesive failure occurred in the upper side of P3HT:PC_{61}BM layer.

6.3. Adhesion in Baseline OPVs with PBDTTT−C:PCBM Active Layers

As another type of inverted OPVs, a PBDTTT−C:$PC_{60}BM$ BHJ active layer was chosen for the mechanical tests due their high PCE (6.6 %) which represents a more state-of-the-art material when compared to P3HT:PCBM [209], as shown in Fig. 4.15. For the PBDTTT−C:$PC_{60}BM$ based inverted solar cell structure, ZnO or PEIE were used as hole blockers to create electron collecting contacts. Next, PEDOT:PSS CPP and MoO_x were used as the hole collecting contacts combined with an Ag metal contact. However, as already mention in section 4.3.1, ITO was replaced with a thin film of SiO_2 (300 nm) because operational devices were not needed to test the adhesion or cohesion in the devices. The SiO_2 surface was coated with a hole blocking layer which was in contact with the active layer and thus, never impacted the deposition or behavior of this interface or the active layer.

To provide a reference baseline for this OPV structure before modifying the contacts or interfaces, the following inverted OPV structure was first tested: Si substrate, SiO_x (300 nm), ZnO (28 nm), PBDTTT−C:$PC_{60}BM$ in 1:1.5 wt% (90 nm), MoO_x (10 nm), Ag (150 nm), epoxy (1 μm), SiO_x (300 nm), Si substrate, as shown in Fig. 6.5(a). To determine the weakest interfaces/layers in the baseline structure (Fig. 6.5(a)), three separate sample batches amounting to a total of 29 samples were prepared and tested with the double cantilever beam (DCB) method. The initial results, as summarized in Table 6.1, show that the interfacial fracture toughness (G_c) of the weakest interface was 0.42 ± 0.06 J/m^2 where the failure occured at the interface between PBDTTT−C:$PC_{60}BM$ active layer and MoO_x as verified by XPS analysis. Following this baseline test, modifications to the electron and hole contacts were made as shown in Figure 6.5

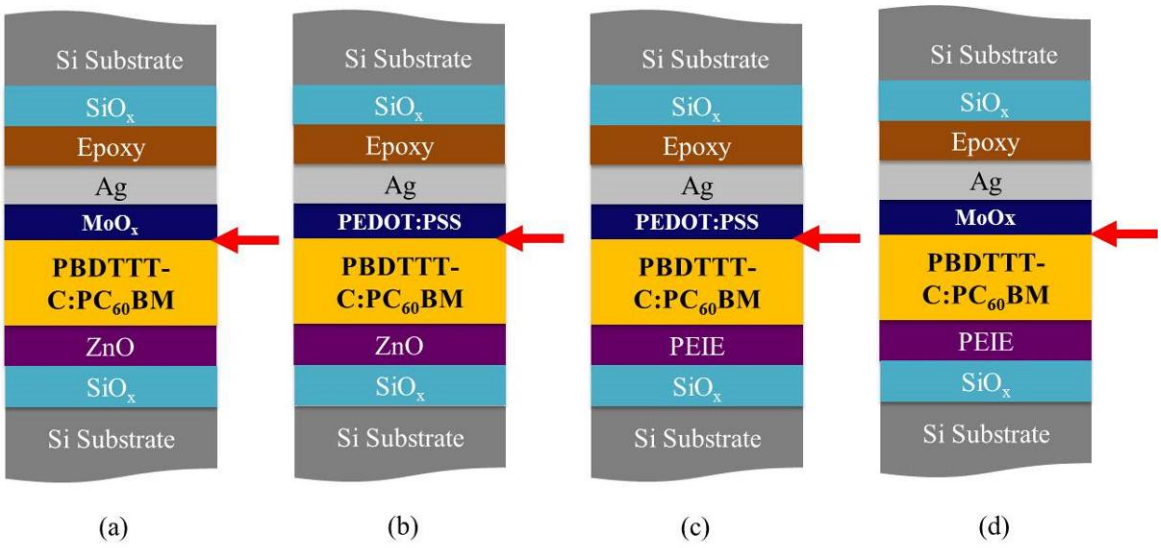

Figure 6.5. Schematic diagram of DCB sample structures composed of Si substrate, SiO_x (300 nm), ZnO (28 nm)/PEIE (10 nm), active layer (PBDTTT−C:PC_{60}BM in 1:1.5 wt%, 90 nm), MoO_x (10 nm)/PEDOT:PSS CPP (100 nm), Ag (150 nm), epoxy (1 μm), SiO_x (300 nm), and Si substrate where arrows indicate the interfacial failure locations.

6.4. Impact of Modifying the Hole Collecting Contact on Adhesion

6.4.1. Using Polymer Electrodes: PEDOT:PSS CPP

After determining the initial adhesion strength using ZnO and MoO_x in the basic structure (Fig. 6.5(a)), the MoO_x was replaced with PEDOT:PSS CPP to see how the polymeric material will impact the adhesion strength in the inverted OPV structure. Unlike the oxide hole collecting contact (MoO_x), the DCB tests showed that the interfacial fracture toughness of the modified structure with PEDOT:PSS CPP was 0.13 ± 0.07 J/m^2 which is approximately three times lower. The delaminated surfaces were scanned using XPS showing the mechanical failure also occurs at the interface between PBDTTT−C:PC_{60}BM active layer and PEDOT:PSS CPP. This inherently weak interface

behavior results from weak van der Waals forces between PBDTTT−C:$PC_{60}BM$ and PEDOT:PSS CPP. For the enhanced adhesion mechanism using the MoO_x hole contact material deposited by a thermal vapor deposition method, it is strongly assumed that this relatively stronger interface using the thin oxide film (MoO_x) compared to the polymeric contact (PEDOT:PSS CPP) structure (0.13 ± 0.07 J/m^2) is created by the MoO_x diffusion during the thermal vapor deposition process [226].

6.4.2. Impact of Order of Film Deposition

It is clear the PEDOT:PSS interfaces represent a weak interface that must be addressed in inverted OPV structures. To further investigate this issue, an OPV with some similarities to the conventional structure was made in which the order of deposition of the layers were reversed yielding the following structure: Si substrate, SiO_x (300 nm), PEDOT:PSS CPP (100 nm), active layer (PBDTTT−C:PCBM in 1:1.5 wt%, 90 nm), ZnO (28 nm), Ag (150 nm), epoxy (1 μm), SiO_x (300 nm), as shown in Fig. 6.6(a). Note that a low work function electrode was not used due to its propensity to oxidize. The purpose of reversing the order of deposition was to see if the in-situ exposure of the stack during the deposition of the ZnO layer would anneal the interface between the active layer and PEDOT:PSS, causing an enhancement in the adhesion strength. Such a process would be expected to occur in conventional OPV devices.

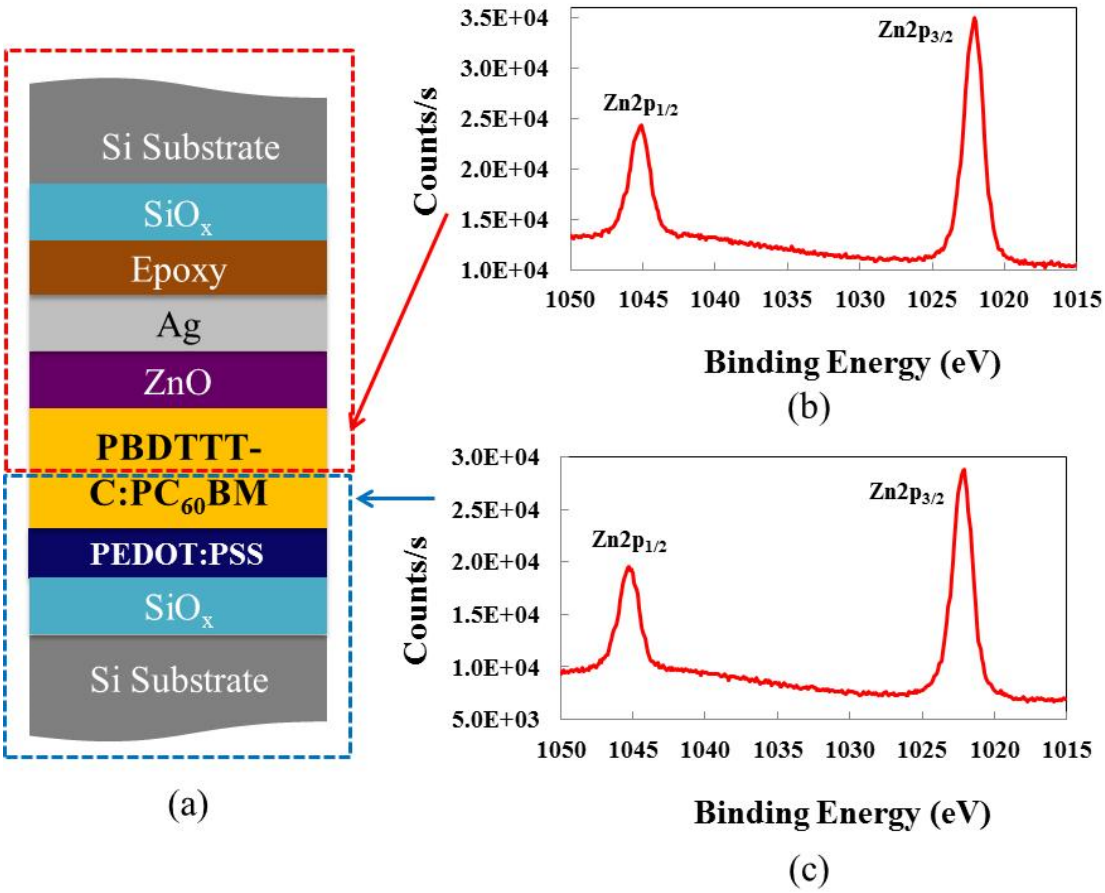

Figure 6.6. (a) A cross sectional image of DCB sample to investigate the order of film deposition comprised of Si substrate, SiO_x (300 nm), PEDOT:PSS CPP (100 nm), active layer (PBDTTT−C: $PC_{60}BM$ in 1:1.5 wt%, 90 nm), ZnO (28 nm), Ag (150 nm), epoxy (1 µm), SiO_x (300 nm) and high resolution XPS scans of delaminated surfaces after DCB tests where (b) is an electron collecting contact side containing PBDTTT−C:$PC_{60}BM$ active layer, ZnO, and Ag and (c) is a hole collecting contact side containing PBDTTT−C: $PC_{60}BM$ active layer and PEDOT:PSS CPP.

The DCB tests from 27 samples showed that the cohesive strength of the samples were 0.33 ± 0.12 J/m^2. The exact failure location was also verified using XPS scans showing that both surfaces after the DCB tests have the same S2p peak (≈ 164 eV) verifying the cohesive failure in the PBDTTT−C:$PC_{60}BM$ BHJ active layer. It is posed that the thermal annealing of the interface helped to form a stronger bond, but no chemical analysis of the interface was used to prove the nature of the reaction or products

formed at the interface. AFM scans (Fig. 6.7) show the surface morphologies of the cohesive failure sample increased in roughness (R_q: 8.31 nm) compared to the adhesive failure sample used in section 6.4.1 in Fig. 6.5(a) (R_q: 2.09 nm). The increased roughness resulted from the deflected crack path and the contact of asperities behind the crack tip during the tensile loading [227].

Beside the annealing effect of the active layer during the ALD ZnO deposition at high temperature, it is possible for the precursor of ZnO (diethylzinc, $(C_2H_5)_2Zn$) to diffuse into polymer layers with repeated precursor injections, forming a ZnO_x network [94]. The high resolution XPS scans revealed a Zn2p peak found on both delaminated surfaces while the failure clearly occurs in the PBDTTT−C:PC_{60}BM BHJ active layer, as shown in Fig. 6.6(b) and (c). While it is not clear what impact the presence of the Zn in

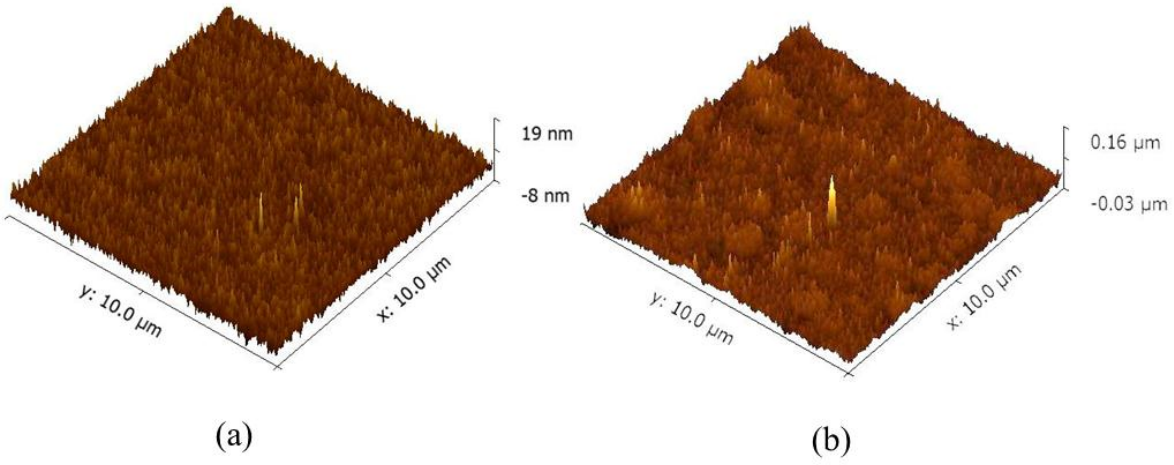

Figure 6.7. 3D AFM image of: (a) delaminated surface of PBDTTT−C:PCBM active layers in inverted OPV structure (Fig. 6.5(a)) where the failure occurred at the interface between the PBDTTT−C:PCBM active layer and PEDOT:PSS CPP (R_q = 2.09 nm) and (b) delaminated surface of PBDTTT−C:PCBM active layers in conventional OPV structure (Fig. 6.6) where the failure occurred in PBDTTT−C:PCBM active layer (R_q = 8.31 nm).

this case, two things are certain: 1) the failure location has shifted from the PEDOT:PSS active layer interface to the bulk of the active layer and 2) the failure strength is much closer to that of the baseline case. Whether or not this can be contributed simply to a Zn based network forming throughout the PEDOT:PSS and active layer is not clear for this case. Thus, additional annealing experiments should be performed without the exposure of the active layers to ZnO ALD processing.

6.4.3. Impact of O_2 Plasma Treatments

As already pointed out in section 6.4.1, the structure containing PEDOT:PSS CPP shows a low interfacial fracture toughness value (0.13 ± 0.07 J/m^2). Therefore, it was decided to modify this interface (PBDTTT−C:PC_{60}BM BHJ active layer and PEDOT:PSS CPP) using an O_2 plasma treatment, as shown in Fig. 6.8. This treatment was expected to increase the wettability of the PEDOT:PSS CPP on the BHJ active layer by introducing polar hydroxyl groups. However, in this application, the plasma exposure can introduces hydroxyl groups to enhance the adhesion strength by permanent dipole-dipole interactions at the interface and it can etch the active layer of the device. As a baseline, the PBDTTT−C:PC_{60}BM BHJ active layer was O_2 plasma treated only for 1 second which has been shown not to damage the device or power conversion efficiency. For the O_2 plasma treatment on the BHJ active layer for 1 second, the DCB tests and XPS scans show that the adhesion strength is 0.14 ± 0.05 J/m^2 while the failure took place at the interface between the active layer and PEDOT:PSS CPP as expected. Therefore, even though short O_2 plasma treatments help increase the wettability of PEDOT:PSS CPP

on the PBDTTT−C:$PC_{60}BM$, it was concluded that the 1 s O_2 plasma treatment does not sufficiently enhance the interfacial fracture toughness.

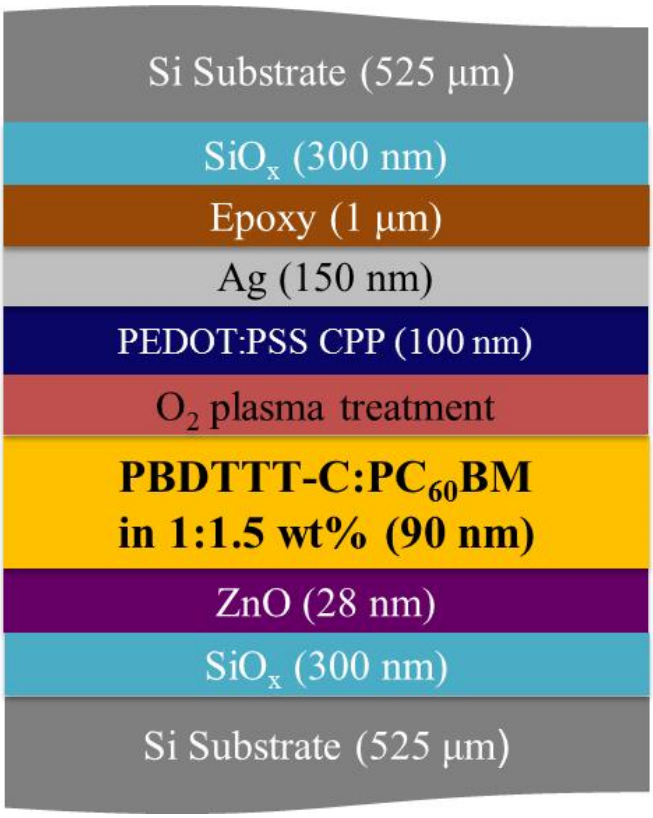

Figure 6.8. A cross sectional image of DCB sample to investigate O_2 plasma treatment effect on the BHJ active layer comprised of Si wafer, ZnO, active layer (PBDTTT−C:$PC_{60}BM$), O_2 plasma exposure, PEDOT:PSS, and Ag bonded with another Si wafer using a room temperature curing epoxy (EPO-TEK 301).

In order to vary the amount of hydroxyl groups introduced from the O_2 plasma treatment, we prepared bare PBDTTT−C:$PC_{60}BM$ films deposited on 2.54 cm × 2.54 cm SiO_2/Si wafers and O_2 plasma treated the surfaces in different time scales (0, 1, 5, 10, 30, 60, and 120 seconds), as shown Fig. 6.9. The surface energy measurements show that the polarity of the PBDTTT−C:$PC_{60}BM$ BHJ active layer saturated after 30 seconds of O_2 plasma treatment, as shown in Fig. 6.9. However, since it is well known that the O_2 plasma treatment on the polymeric materials can damage the surface which eventually increases the surface roughness (R_q) [174-176, 228, 229], the surface roughness of O_2 plasma treated films also was measured to evaluate the surface morphology effect while the rougher surface leading to larger contact area can also enhance the adhesion strength at the interface from mechanical interlocking effect (Fig. 3.6), as explained in section 3.4. Thus, in order to isolate the surface morphology effect from the high polarity effect when measuring the interfacial fracture toughness, 30 seconds O_2 plasma treatment was chosen because the surface polarity is maximized at this point while the surface roughness also remains almost same at 1 nm (R_q) (Fig. 6.9). By further treating the surface with O_2 plasma system, the surface was clearly damaged as the surface roughness increased to higher values (2.2 nm and 3.3 nm for 1 and 2 mins O_2 plasma treatment).

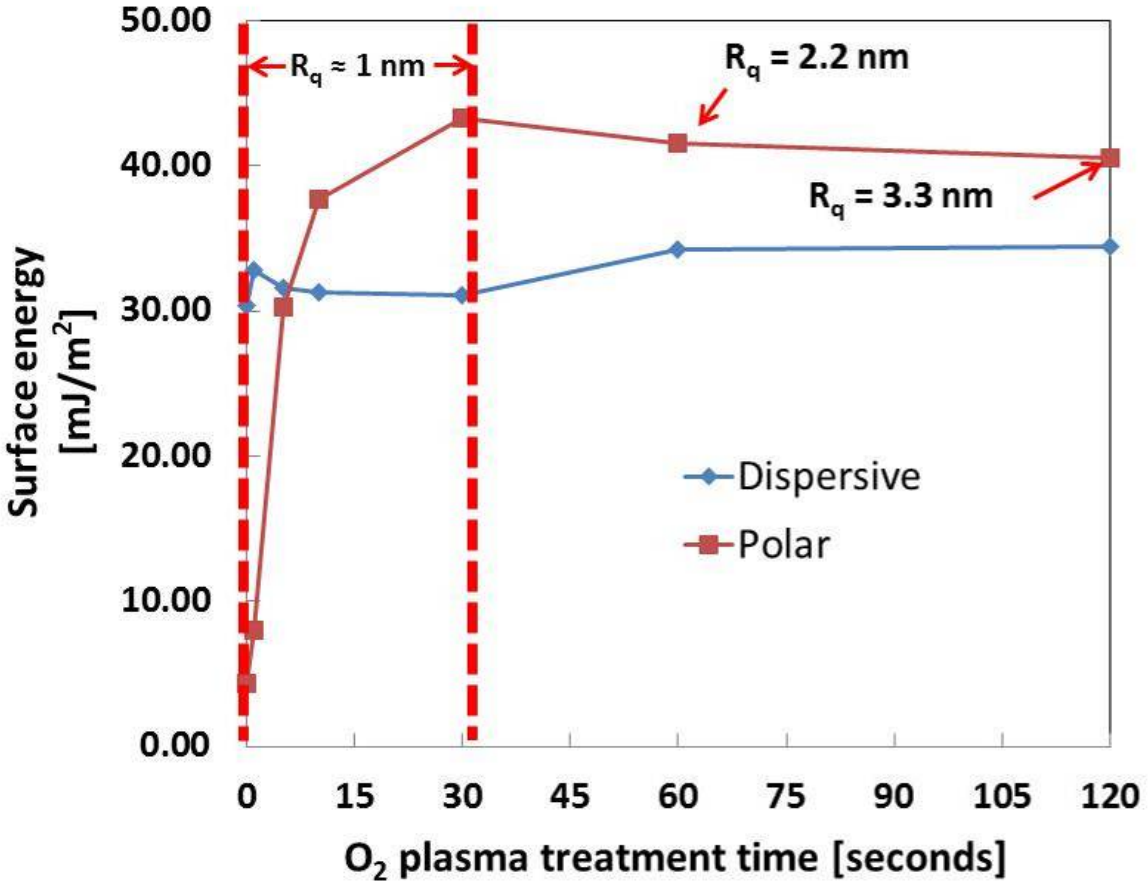

Figure 6.9. O_2 plasma treated PBDTTT−C:PC_{60}BM BHJ active layers for 0, 1, 5, 10, 30, 60, and 120 seconds with related to surface energy (mJ/m^2) and surface roughness (R_q, nm) where the surface polarity is saturated at 30 seconds while the surface roughness remains the same at 1 nm.

By optimizing the O_2 plasma treatment conditions, two different samples batches for DCB samples were fabricated again by only adding a 30 seconds O_2 plasma treatment process on the PBDTTT−C:PC_{60}BM BHJ active layer, as shown in Fig. 6.10(a). The DCB tests show that the failure location shifted toward the PBDTTT−C:PC_{60}BM BHJ active layer with higher fracture toughness values (0.32 ± 0.14 J/m^2) comparing to the interface without the O_2 plasma treatment (0.13 ± 0.07 J/m^2). Thus, it also shows the

consistent result with our hypothesis that 30 seconds O_2 plasma treatment on the PBDTTT−C:PC_{60}BM BHJ active layer introduces sufficient hydroxyl groups to induce more permanent dipole−dipole intermolecular interactions between the PBDTTT−C:PC_{60}BM BHJ active layer and PEDOT:PSS CPP, and to form a stronger interface compared to the bare interface without any treatment. The failure location was verified using high resolution XPS scans showing both delaminated surfaces after the DCB tests only have one S2p peak at 164 eV (Fig. 6.10(b) and (c)) indicating the XPS scanned surfaces are the PBDTTT−C:PC_{60}BM active layer supporting the cohesive failure for this new structure.

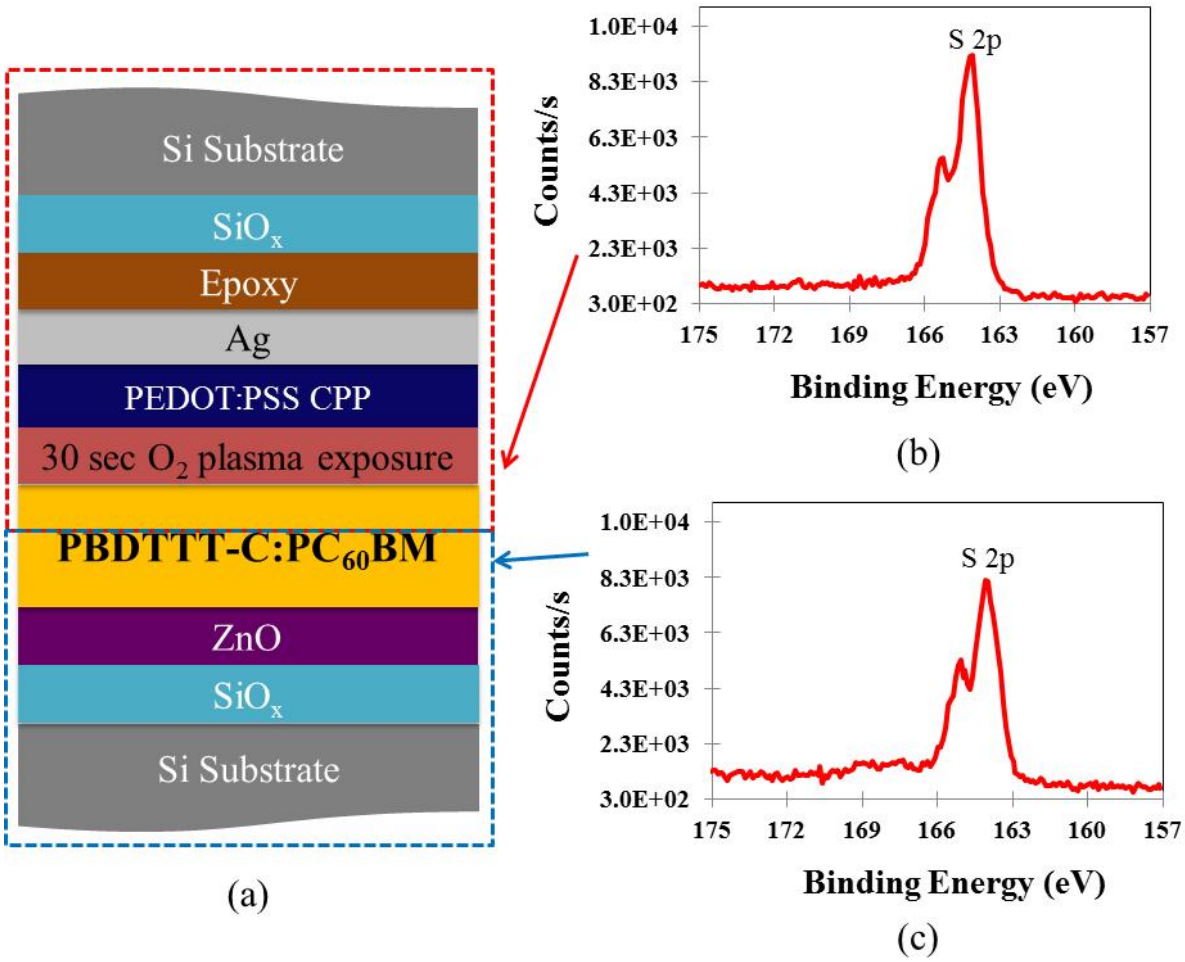

Figure 6.10. (a) A cross sectional image of DCB sample to investigate 30 seconds O_2 plasma treatment effect on the PBDTTT−C: $PC_{60}BM$ BHJ active layer comprised of Si substrate, ZnO, active layer (PBDTTT−C:$PC_{60}BM$), 30 seconds O_2 plasma exposure, PEDOT:PSS, and Ag bonded with another Si wafer using a room temperature curing epoxy (EPO-TEK 301) and (b) and (c) high resolution XPS scans of delaminated surfaces after DCB tests where both delaminates surfaces have a S2p peak at 164 eV indicating the cohesive failure in the PBDTTT−C:$PC_{60}BM$ layer.

6.5. Impact of Modifying the Electron Collecting Contact on Adhesion

In order to modify the electron collecting contact, polyethylenimine (PEIE), which can be used to fabricate air stable low work function electrodes [209], was chosen and tested to determine its impact on the interfacial fracture toughness in the inverted OPV, as shown in Fig. 6.5(c) and (d). For this purpose, two different types of the inverted OPV structure, as summarized in Table 6.1, were fabricated using PEIE as the electron collecting contact (ECC) material. As summarized in Table 6.1, these two different structures consisting of PEDOT:PSS (Fig. 6.5(c)) and MoO_x (Fig. 6.5(d)) as the hole collecting contacts, respectively, with having the same electron collecting contact (PEIE) did not show any different mechanical failure patterns comparing to the inverted OPV structures (Fig. 6.5(a) and (b)). The failure occurred at the interface between PBDTTT−C:$PC_{60}BM$ BHJ active layer and hole collecting contacts (MoO_x and PEDOT:PSS CPP) reporting similar interfacial fracture toughness values with previous data (MoO_x: 0.39 ± 0.11 J/m^2 (Fig. 6.5(a) and PEDOT:PSS CPP: 0.16 ± 0.04 J/m^2 (Fig. 6.5(b)). As a post analysis step, the failure location was also verified using the XPS scans. Since the failure occurred at the interface between the PBDTTT−C:$PC_{60}BM$ active layer and hole collecting contacts (MoO_x and PEDOT:PSS), it is concluded that the polymeric electron collecting contact using PEIE forms a rigid electrostatic interface with the PBDTTT−C:$PC_{60}BM$ BHJ active layer. It is clear that this interface is stronger than even the cohesive strength of the BHJ active layer.

Table 6.1. Impact of Modifying Electrical Contact on Interfacial Fracture Toughness.

Structure	Hole collecting contact	Electron collecting contact	Failure location	G_c [J/m^2]
Inverted (Fig. 6.2(a))	Plexcore Material	ZnO	Between P3HT:PCBM and Plexcore material	0.18±0.15
Inverted (Fig. 6.3(a))	MoO_x	ZnO	Upper part of P3HT:PCBM	0.39±0.09
Inverted (Fig. 6.5(a))	MoO_x	ZnO	Between PBDTTT−C:PCBM and MoO_x	0.42±0.06
Inverted (Fig. 6.5(a))	PEDOT:PSS CPP	ZnO	Between PBDTTT−C:PCBM and PEDOT:PSS CPP	0.13±0.07
Conventional (Fig. 6.6(a))	PDEDOT:PSS CPP	ZnO	In PBDTTT−C:PCBM	0.33±0.12
Inverted (Fig. 6.8)	PDEDOT:PSS CPP on 1s O_2 plasma treated PBDTTT−C:PCBM	ZnO	Between PBDTTT−C:PCBM and PEDOT:PSS CPP	0.14±0.05
Inverted (Fig. 6.10(a))	PDEDOT:PSS CPP on 30s O_2 plasma treated PBDTTT−C:PCBM	ZnO	In PBDTTT−C:PCBM	0.32±0.14
Inverted (Fig. 6.5(d))	MoO_x	PEIE	Between PBDTTT−C:PCBM and MoO_x	0.39±0.11
Inverted (Fig. 6.5(c)))	PEDOT:PSS CPP	PEIE	Between PBDTTT−C:PCBM and PEDOT:PSS CPP	0.16±0.04

6.6. Summary

In this chapter, quantitative adhesive/cohesive strength values (J/m^2) of the weakest interfaces/layers in the inverted OPVs using P3HT:PC_{61}BM and PBDTTT−C:PC_{60}BM BHJ active layers were provided using various types of interface modification materials. In order to determine the interfacial fracture toughness (J/m^2), the double cantilever beam (DCB) technique was utilized as the standard adhesion measurement technique in thin films. Firstly, it was found that the hydrophobic P3HT:PC_{61}BM active layer and negatively charged PEDOT:PSS based Plexcore

materials form the weakest interface [11] for the inverted structure consisting of Si substrate, SiO_x, ZnO, active layer (P3HT:$PC_{61}BM$), Plexcore OC XA-1871™, and Ag, as also recently reported by Dauskardt [11]. As a different structure, the weakest location of the first inverted structure comprised of Si substrate, SiO_x, ZnO, active layer (PBDTTT−C:$PC_{60}BM$), MoO_x, and Ag was the interface between the PBDTTT−C:$PC_{60}BM$ active layer and hole collecting contact (MoO_x) showing the highest interfacial fracture toughness (0.42 ± 0.06 J/m^2) while other structures with different interface modifications show low adhesion strength values, as summarized in Table 6.1. This relatively strong interface amongst other modified structures used in this study was originated from the MoO_x diffusion caused during the thermal vapor deposition process. In addition, we found out that the order of the film deposition in the device fabrication affects the mechanical strength as well as the device operation. For the interface modification method, it is concluded that short O_2 plasma treatments on the PBDTTT−C:$PC_{60}BM$ BHJ active layer is not a promising way to enhance the adhesion strength due to the surface coverage with hydroxyl groups. However, by increasing O_2 plasma treatment time up to 30 seconds, the surface polarity was maximized possibly leading to enhanced adhesion strength by inducing more permanent dipole-dipole intermolecular interactions at the interface between the PBDTTT−C:$PC_{60}BM$ active layer and PEDOT:PSS CPP. In addition, the PEIE polymer contact was found to be quite strong. This is important as the use of PEIE to make a low work function electron selective contact can be combined with a conductive polymer to possibly make an all polymer electrode with strong mechanical adhesion. Overall, this study reports the initial adhesive/cohesive strength values with possible bonding mechanisms at the failure

locations and, helps understanding the adhesive and cohesive failure and reliability of inverted OPV devices.

CHAPTER 7

CONCLUSION AND OUTLOOK

7.1. Conclusion

The research in this dissertation has been conducted to provide the initial quantification of the adhesion strength at typical interface used in operational inverted OPVs and model barrier films, to understand methods that influence the adhesion strength, and to determine the methods to improve the adhesion strength for the long term mechanical reliability of inverted OPV devices.

Important findings of this dissertation are as follows:

- Chapter 4 introduced a currently developed SiN_x–PMMA multilayer barrier films that provide an ultra-low water vapor transmission rate (WVTR $\leq 5\times10^{-5}$ g/m^2/day measured at room temperature conditions). The developed SiN_x and PMMA model structure was used in this dissertation to understand the adhesion mechanisms of organic and inorganic interface in multilayer barrier films.
- A new sample preparation method was developed to allow greater yield for testing the interfacial fracture toughness of four point bend and double cantilever beam specimens.
- Chapter 5 explained demonstrated factors that influence the interfacial fracture toughness of inorganic/organic multilayer barrier films. The first reports of the impact of phosphonic acid surface modifiers on interfacial

adhesion were reported. For secondary bonding conditions, it was found that the interfacial fracture toughness scaled with the polar component of the surface energy while it was assumed that this dominantly affects interfacial fracture toughness by enabling strong permanent dipole-dipole interactions among various factors that can still exist to change the fracture energy. In order to increase the adhesion strength further at the SiN_x−PMMA interface, strong covalent bonds were created using a benzophenone derivative [219] at the model interface which eventually increases the interfacial fracture toughness by five times compared to the initial the SiN_x−PMMA interface. As the last adhesion control method in this dissertation, the plastic zone size of the PMMA film in the SiN_x−PMMA interface was controlled by changing the thickness of the PMMA film which finally increases the interfacial fracture toughness by a factor of three.

- Chapter 6 presented results on the adhesive and cohesive failure of inverted organic photovoltaic devices. First, the weakest interface in P3HT:$PC_{61}BM$ and PBDTTT−C:$PC_{60}BM$ BHJ was determined using model structures. This generally consisted of failures at the interface between the active layer and hole collecting contact interface. For a PBDTTT−C:$PC_{60}BM$ BHJ based organic solar cell, it was found that the highest interfacial fracture toughness (0.42 J/m^2) was achieved when using a MoO_x/Ag hole collecting contact. When the MoO_x was switched to PEDOT:PSS, this value fell to 0.13 J/m^2. The introduction of an oxygen

plasma treatment at this interface, however, was found to increase this strength us to 0.32 J/m^2 with the failure being limited not by the interface, but by the cohesive failure of the active material. These data show that the adhesive and cohesive failure strengths of OPV devices is quite weak and may be ultimately limited by the strength of the BHJ active layers, even when all of the interfacial strength values are appropriately treated to maximize their values.

7.2. Future Work

As pointed out in previous research, the exposure of OPVs and barrier films to typical environmental conditions can induce oxidation and other reactions within the solar cell. While the initial portion of this work focuses on only providing an understanding of the baseline adhesion in OPVs and barriers, the future will focus on the changes in these properties with environmental exposure. Based on previous research, it has been shown that thermal annealing can improve the contact with the electrodes [11, 125]. However, oxidation of the contacts results in loss of electrical contact with the active layer. Thus, as the future work, it will be necessary to explore the impact of the degradation of these contacts based on aging and environmental exposure. Overall, interfacial adhesion strength can degrade due to complex reactions of environmental species with and without photochemical reactions [141, 147, 150-153]. In order to explore these effects, both multilayer barrier films and OPV structures should be exposed to accelerated test conditions in an environmental humidity chamber or weather accelerated tests should be performed at standard damp heat conditions of 85°C and 85%

RH. Additional samples should be exposed to AM 1.5 solar spectrum for 1000h to observe any photochemically induced effects. After environmental testing, FPB and DCB testing should be used to characterize the interfacial fracture toughness.

As an initial study on environmentally induced aging effects, the impact of the exposure of multilayer barrier films (SiN_x/PMMA) exposed outdoor conditions was explored. The model barriers were stored outside for two weeks during June 2012 while temperature (°C) and humidity (%) were monitored as shown in Fig. 7.1. Overall, the FPB tests showed that interfacial adhesion strength of the SiN_x/PMMA interface degraded from 4.85 J/m^2 to 3.30 J/m^2 due to the complex reactions of environmental species. However, this work only provides very limited insight into how much the adhesion strength can be degraded when exposing to the outdoor conditions for two weeks. Thus, further research should be performed to look at more environmentally induced aging effects in detail.

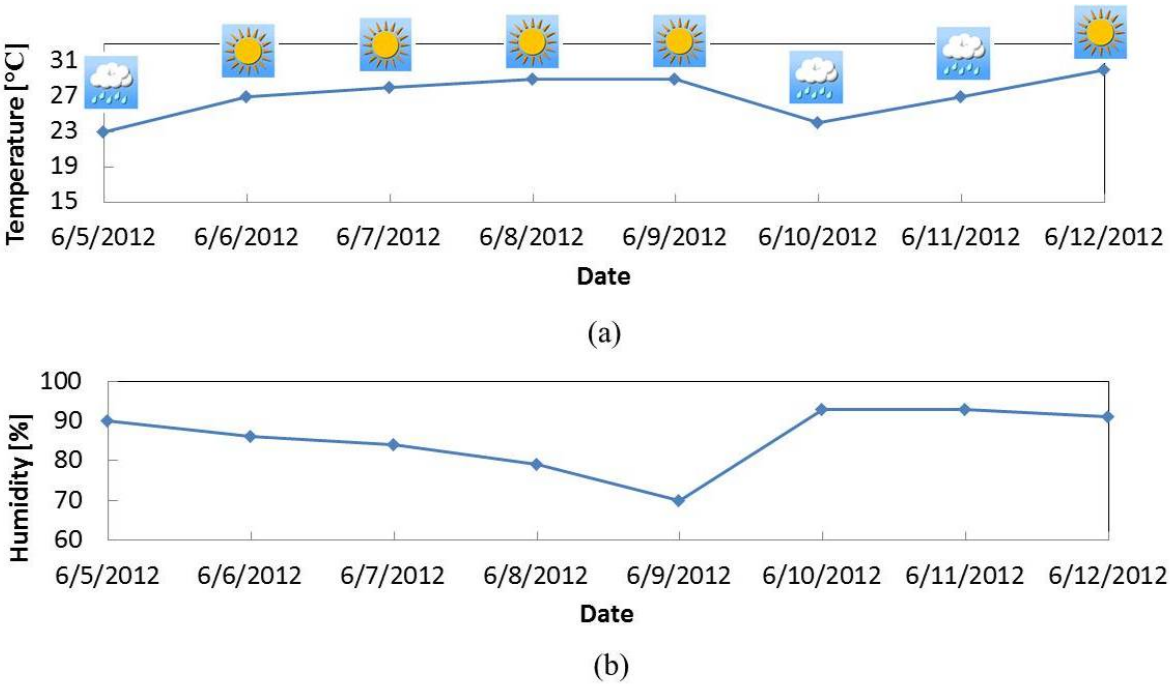

Figure 7.1. Weather monitored during 06/05/2012 ~ 06/12/2012 provided by Weather Underground, Inc.: (a) temperature (°C) and (b) humidity (%).

The stress relaxation technique of the double cantilever beam approach should be used to study crack growth rates (da/dt) vs. the applied strain energy release rate (J/m^2) curve to explore the possibility of progressive and time-depending failure of the interfaces [144, 230, 231]. By developing the crack growth rate (da/dt) vs. strain energy release rate (J/m^2) curve, the threshold (G_{th}) point the effect of surface treatments on subcritical crack growth can also be explored and determined.

For OPV devices, it is not clear if the devices will always be limited by cohesive failure for the two systems chosen in this study lie around 0.35-0.4 J/m^2. A study needs to be performed to see if the cohesive strength in these systems can be increased without greatly impacting the device performance. On the other hand, since the interfacial fracture toughness values are known, an engineering approach can also be taken to limit the stresses that are placed on the interfaces of these active layers. The stresses can arise from coefficient of thermal expansion mismatch as the solar cells heat and cool throughout the day. In addition, environmental loading (wind, rain, etc.) can also induce stresses. The use of design strategies that account for the inherently weak interfaces could be taken on by mechanical engineers to design reliable devices that will not fail readily when exposed to normal operating conditions.

REFERENCES

[1] M. S. Weaver, *et al.*, "Organic light-emitting devices with extended operating lifetimes on plastic substrates," *Applied Physics Letters,* vol. 81, pp. 2929-2931, Oct 14 2002.

[2] G. Gu, *et al.*, "High-external-quantum-efficiency organic light-emitting devices," *Optics Letters,* vol. 22, pp. 396-398, Mar 15 1997.

[3] G. Gu, *et al.*, "Vacuum-deposited, nonpolymeric flexible organic light-emitting devices," *Optics Letters,* vol. 22, pp. 172-174, Feb 1 1997.

[4] M. Jorgensen, *et al.*, "Stability of Polymer Solar Cells," *Advanced Materials,* vol. 24, pp. 580-612, Feb 2 2012.

[5] S. R. Forrest, "The path to ubiquitous and low-cost organic electronic appliances on plastic," *Nature,* vol. 428, pp. 911-918, Apr 29 2004.

[6] S. Logothetidis, "Flexible organic electronic devices: Materials, process and applications," *Materials Science and Engineering B-Advanced Functional Solid-State Materials,* vol. 152, pp. 96-104, Aug 25 2008.

[7] F. C. Krebs, "Degradation and stability of polymer and organic solar cells," *Solar Energy Materials and Solar Cells,* vol. 92, pp. 685-685, Jul 2008.

[8] M. Schaer, *et al.*, "Water vapor and oxygen degradation mechanisms in organic light emitting diodes," *Advanced Functional Materials,* vol. 11, pp. 116-121, Apr 2001.

[9] M. Hermenau, *et al.*, "Water and oxygen induced degradation of small molecule organic solar cells," *Solar Energy Materials and Solar Cells,* vol. 95, pp. 1268-1277, May 2011.

[10] K. Norrman and F. C. Krebs, "Degradation and stability of R2R manufactured polymer solar cells," *Proceedings of the SPIE,* vol. 7416, 2009.

[11] S. R. Dupont, *et al.*, "Interlayer adhesion in roll-to-roll processed flexible inverted polymer solar cells," *Solar Energy Materials and Solar Cells,* vol. 97, pp. 171-175, Feb 2012.

[12] S. K. Hau, *et al.*, "Air-stable inverted flexible polymer solar cells using zinc oxide nanoparticles as an electron selective layer," *Applied Physics Letters,* vol. 92, Jun 23 2008.

[13] "NREL, Best research-cell efficiencies," *USA,* 2011.

[14] T. L. Benanti and D. Venkataraman, "Organic solar cells: An overview focusing on active layer morphology," *Photosynthesis Research,* vol. 87, pp. 73-81, Jan 2006.

[15] J. M. Nunzi, "Organic photovoltaic materials and devices," *Comptes Rendus Physique,* vol. 3, pp. 523-542, May 2002.

[16] B. Kippelen and J. L. Bredas, "Organic photovoltaics," *Energy & Environmental Science,* vol. 2, pp. 251-261, 2009.

[17] C. J. Brabec, "Organic photovoltaics: technology and market," *Solar Energy Materials and Solar Cells,* vol. 83, pp. 273-292, Jun 15 2004.

[18] W. J. Potscavage, "Physics and Engineering of Organic Soalr Cells," *Ph.D. Dissertation at Georgia Institute of Technology,* 2011.

[19] W. Ge, "An overview on P3HT:PCBM, the most efficient organic solar cell material so far.," 2009.

[20] G. Chidichimo and L. Filippelli, "Organic Solar Cells: Problems and Perspectives," *International Journal of Photoenergy,* 2010.

[21] H. Huang and P. G. Pickup, "A donor-accepter conducting copolymer with a very low band gap and high intrinsic conductivity," *Chemistry of Materials,* vol. 10, pp. 2212-2216, Aug 1998.

[22] Y. H. Kim, *et al.*, "Highly Conductive PEDOT:PSS Electrode with Optimized Solvent and Thermal Post-Treatment for ITO-Free Organic Solar Cells," *Advanced Functional Materials,* vol. 21, pp. 1076-1081, Mar 22 2011.

[23] S. Shaheen, *et al.*, "Inverted bulk-heterojunction plastic solar cells," *SPIE,* pp. 1-3, 2007.

[24] S. Cook, *et al.*, "Ultrafast Studies of Charge Generation in PCBM:P3HT Blend Films following Excitation of the Fullerene PCBM," *Journal of Physical Chemistry C,* vol. 113, pp. 2547-2552, Feb 12 2009.

[25] E. K. Chiew, *et al.*, "Electrical Characterization of P3HT/PCBM Bulk Heterojunction Oganic Solar Cell," *International Journal of Computational Materials Science and Engineering,* vol. 1, pp. 12500042-1~12500042-8, 2012.

[26] G. Garcia-Belmonte, *et al.*, "Charge carrier mobility and lifetime of organic bulk heterojunctions analyzed by impedance spectroscopy," *Organic Electronics,* vol. 9, pp. 847-851, Oct 2008.

[27] X. Yang and J. Loos, "Toward high-performance polymer solar cells: The importance of morphology control," *Macromolecules,* vol. 40, pp. 1353-1362, Mar 6 2007.

[28] H. Hoppe and N. S. Sariciftci, "Organic solar cells: An overview," *Journal of Materials Research,* vol. 19, pp. 1924-1945, Jul 2004.

[29] H. Hoppe, *et al.*, "Optical constants of conjugated polymer/fullerene based bulk-heterojunction organic solar cells," *Molecular Crystals and Liquid Crystals,* vol. 385, pp. 233-239, 2002.

[30] J. deBoisblanc, "Synthesis and Characterization of P3HT:PCBM Organic Solar Cells," *Pomona College Department of Physics and Astronomy Senior Theses,* May 4 2010.

[31] Q. L. Huang, *et al.*, "Covalently bound hole-injecting nanostructures. Systematics of molecular architecture, thickness, saturation, and electron-blocking characteristics on organic light-emitting diode luminance, turn-on voltage, and quantum efficiency," *Journal of the American Chemical Society,* vol. 127, pp. 10227-10242, Jul 27 2005.

[32] S. E. Shaheen, *et al.*, "2.5% efficient organic plastic solar cells," *Applied Physics Letters,* vol. 78, pp. 841-843, Feb 5 2001.

[33] M. Girtan and M. Rusu, "Role of ITO and PEDOT:PSS in stability/degradation of polymer: fullerene bulk heterojunctions solar cells," *Solar Energy Materials and Solar Cells,* vol. 94, pp. 446-450, Mar 2010.

[34] M. Jorgensen, *et al.*, "Stability/degradation of polymer solar cells," *Solar Energy Materials and Solar Cells,* vol. 92, pp. 686-714, Jul 2008.

[35] M. T. Lloyd, *et al.*, "Impact of contact evolution on the shelf life of organic solar cells," *Journal of Materials Chemistry,* vol. 19, pp. 7638-7642, 2009.

[36] A. C. Mayer, *et al.*, "Polymer-based solar cells," *Materials Today,* vol. 10, pp. 28-33, Nov 2007.

[37] B. Friedel, *et al.*, "Effects of Layer Thickness and Annealing of PEDOT:PSS Layers in Organic Photodetectors," *Macromolecules,* vol. 42, pp. 6741-6747, Sep 8 2009.

[38] M. O. Reese, *et al.*, "Pathways for the degradation of organic photovoltaic P3HT : PCBM based devices," *Solar Energy Materials and Solar Cells,* vol. 92, pp. 746-752, Jul 2008.

[39] K. Norrman and F. C. Krebs, "Photodegradation of poly(ether sulphone) Part 2. Wavelength and atmosphere dependence," *Surface and Interface Analysis,* vol. 36, pp. 1542-1549, Dec 2004.

[40] J. Alstrup, *et al.*, "Lifetimes of organic photovoltaics: Design and synthesis of single oligomer molecules in order to study chemical degradation mechanisms," *Solar Energy Materials and Solar Cells,* vol. 90, pp. 2777-2792, Nov 6 2006.

[41] K. Norrman and F. C. Krebs, "Lifetimes of organic photovoltaics: Using TOF-SIMS and O-18(2) isotopic labelling to characterise chemical degradation mechanisms," *Solar Energy Materials and Solar Cells,* vol. 90, pp. 213-227, Jan 23 2006.

[42] K. Norrman, *et al.*, "Lifetimes of organic photovoltaics: Combining chemical and physical characterisation techniques to study degradation mechanisms," *Solar Energy Materials and Solar Cells,* vol. 90, pp. 2793-2814, Nov 6 2006.

[43] M. Lira-Cantu, *et al.*, "Oxygen release and exchange in niobium oxide MEHPPV hybrid solar cells," *Chemistry of Materials,* vol. 18, pp. 5684-5690, Nov 28 2006.

[44] F. C. Krebs and K. Norrman, "Analysis of the failure mechanism for a stable organic photovoltaic during 10000 h of testing," *Progress in Photovoltaics,* vol. 15, pp. 697-712, Dec 2007.

[45] K. Norrman, *et al.*, "Three-dimensional chemical and physical analysis of the degradation mechanisms in organic photovoltaics," *Organic Photovoltaics VII,* vol. 6334, pp. U100-U111, 2006.

[46] N. Kawashima, *et al.*, "Organic-inorganic hybrid encapsulation for P3HT field-effect transistors," *Mater. Res. Soc. Symp. Proc.,* vol. 871E, 2005.

[47] N. Kim, *et al.*, "A hybrid encapsulation method for organic electronics," *Applied Physics Letters,* vol. 94, pp. 1-3, Apr 20 2009.

[48] G. L. Graff, *et al.*, "Mechanisms of vapor permeation through multilayer barrier films: Lag time versus equilibrium permeation," *Journal of Applied Physics,* vol. 96, pp. 1840-1849, 2004.

[49] A. A. Dameron, *et al.*, "Gas diffusion barriers on polymers using multilayers fabricated by Al2O3 and rapid SiO2 atomic layer deposition," *Journal of Physical Chemistry C,* vol. 112, pp. 4573-4580, Mar 27 2008.

[50] N. Kim, "Fabrication and characterization of thin-film encapsulation for organic electronics," *Ph.D. Dissertation at Georgia Institute of Technology,* pp. 55-70, 2009.

[51] J. Meyer, *et al.*, "Reliable thin film encapsulation for organic light emitting diodes grown by low-temperature atomic layer deposition," *Applied Physics Letters,* vol. 94, Jun 8 2009.

[52] H. Cheun, *et al.*, "Electrical and Optical Properties of ZnO Processed by Atomic Layer Deposition in Inverted Polymer Solar Cells," *Journal of Physical Chemistry C,* vol. 114, pp. 20713-20718, Dec 9 2010.

[53] M. S. White, *et al.*, "Inverted bulk-heterojunction organic photovoltaic device using a solution-derived ZnO underlayer," *Applied Physics Letters,* vol. 89, Oct 2 2006.

[54] Y. H. Zhou, *et al.*, "Inverted organic solar cells with ITO electrodes modified with an ultrathin Al2O3 buffer layer deposited by atomic layer deposition," *Journal of Materials Chemistry,* vol. 20, pp. 6189-6194, 2010.

[55] H. Cheun, *et al.*, "Inverted polymer solar cells with amorphous indium zinc oxide as the electron-collecting electrode," *Optics Express,* vol. 18, pp. A506-A512, Nov 2010.

[56] P. de Bruyn, *et al.*, "A facile route to inverted polymer solar cells using a precursor based zinc oxide electron transport layer," *Organic Electronics,* vol. 11, pp. 1419-1422, Aug 2010.

[57] G. Li, *et al.*, "Efficient inverted polymer solar cells," *Applied Physics Letters,* vol. 88, Jun 19 2006.

[58] H. M. Zhang and J. Y. Ouyang, "High-performance inverted polymer solar cells with lead monoxide-modified indium tin oxides as the cathode," *Organic Electronics,* vol. 12, pp. 1864-1871, Nov 2011.

[59] Y. H. Zhou, *et al.*, "Optimization of a polymer top electrode for inverted semitransparent organic solar cells," *Organic Electronics,* vol. 12, pp. 827-831, May 2011.

[60] D. W. Zhao, *et al.*, "Optimization of an inverted organic solar cell," *Solar Energy Materials and Solar Cells,* vol. 94, pp. 985-991, Jun 2010.

[61] M. T. Lloyd, *et al.*, "Enhanced Lifetime in Unencapsulated Organic Photovoltaics with Air Stable Electrodes," *35th IEEE Photovoltaic Specialists Conference,* pp. 1060-1063, 2010.

[62] J. Andersons, *et al.*, "Evaluation of toughness by finite fracture mechanics from crack onset strain of brittle coatings on polymers," *Theoretical and Applied Fracture Mechanics,* vol. 49, pp. 151-157, Apr 2008.

[63] Y. Leterrier, "Durability of nanosized oxygen-barrier coatings on polymers," *Progress in Materials Science,* vol. 48, pp. 1-55, 2003.

[64] Y. Leterrier, *et al.*, "Adhesion of silicon oxide layers on poly(ethylene terephthalate) .2. Effect of coating thickness on adhesive and cohesive strengths," *Journal of Polymer Science Part B-Polymer Physics,* vol. 35, pp. 1463-1472, Jul 15 1997.

[65] J. Lewis, "Material challenge for flexible organic devices," *Materials Today,* vol. 9, pp. 38-45, 2006.

[66] J. Lewis, *et al.*, "Mechanical performance of thin films in flexible displays," *Flexible Electronics 2004-Materials and Device Technology,* vol. 814, pp. 189-198, 2004.

[67] V. Brand, *et al.*, "Cohesion and device reliability in organic bulk heterojunction photovoltaic cells," *Solar Energy Materials and Solar Cells,* vol. 99, pp. 182-189, Apr 2012.

[68] J. S. Lewis and M. S. Weaver, "Thin-film permeation-barrier technology for flexible organic light-emitting devices," *IEEE Journal of Selected Topics in Quantum Electronics,* vol. 10, pp. 45-57, Jan-Feb 2004.

[69] C. J. Brabec, *et al.*, "Polymer-Fullerene Bulk-Heterojunction Solar Cells," *Advanced Materials,* vol. 22, pp. 3839-3856, Sep 8 2010.

[70] K. Norrman, *et al.*, "Degradation patterns in water and oxygen of an inverted polymer solar cell," *Journal of the American Chemical Society,* vol. 132, pp. 16883-16892, Dec 1st 2010.

[71] A. Hayakawa, *et al.*, "High performance polythiophene/fullerene bulk-heterojunction solar cell with a TiOx hole blocking layer," *Applied Physics Letters,* vol. 90, Apr 16 2007.

[72] C. Lungenschmied, *et al.*, "Flexible, long-lived, large-area, organic solar cells," *Solar Energy Materials and Solar Cells,* vol. 91, pp. 379-384, Mar 6 2007.

[73] T. Jeranko, *et al.*, "Patterns of efficiency and degradation of composite polymer solar cells," *Solar Energy Materials and Solar Cells,* vol. 83, pp. 247-262, Jun 15 2004.

[74] M. T. Lloyd, *et al.*, "Influence of the hole-transport layer on the initial behavior and lifetime of inverted organic photovoltaics," *Solar Energy Materials and Solar Cells,* vol. 95, pp. 1382-1388, May 2011.

[75] P. E. Burrows, *et al.*, "Ultra barrier flexible substrates for flat panel displays," *Displays,* vol. 22, pp. 65-69, May 2001.

[76] M. T. Lloyd, *et al.*, "Understanding Degradation Pathways in Organic Photovoltaics," *Photovoltaic Module Reliability Workshop at National Renewable Energy Laboratory (NREL),* 2011.

[77] J. A. Hauch, *et al.*, "Flexible organic P3HT : PCBM bulk-heterojunction modules with more than 1 year outdoor lifetime," *Solar Energy Materials and Solar Cells,* vol. 92, pp. 727-731, Jul 2008.

[78] G. Dennler, *et al.*, "A new encapsulation solution for flexible organic solar cells," *Thin Solid Films,* vol. 511, pp. 349-353, Jul 26 2006.

[79] J. Meyer, *et al.*, "Al2O3/ZrO2 Nanolaminates as Ultrahigh Gas-Diffusion Barriers-A Strategy for Reliable Encapsulation of Organic Electronics," *Advanced Materials,* vol. 21, pp. 1845-1849, May 11 2009.

[80] S. Sarkar, *et al.*, "Encapsulation of organic solar cells with ultrathin barrier layers deposited by ozone-based atomic layer deposition," *Organic Electronics,* vol. 11, pp. 1896-1900, Dec 2010.

[81] P. Mandlik, *et al.*, "A single-layer permeation barrier for organic light-emitting displays," *Applied Physics Letters,* vol. 92, Mar 10 2008.

[82] T. B. Harvey, *et al.*, "Passivated Organic Device Having Alternating Layers of Polymer and Dielectric," *U.S. Patent 5757126,* 1998.

[83] Y. J. Kim, *et al.*, "Durable polyisobutylene edge sealants for organic electronics and electrochemical devices," *Solar Energy Materials and Solar Cells,* vol. 100, pp. 120-125, May 2012.

[84] F. C. Krebs, "Roll-to-roll fabrication of monolithic large-area polymer solar cells free from indium-tin-oxide," *Solar Energy Materials and Solar Cells,* vol. 93, pp. 1636-1641, Sep 2009.

[85] F. C. Krebs, *et al.*, "A round robin study of flexible large-area roll-to-roll processed polymer solar cell modules," *Solar Energy Materials and Solar Cells,* vol. 93, pp. 1968-1977, Nov 2009.

[86] S. A. Gevorgyan, *et al.*, "An inter-laboratory stability study of roll-to-roll coated flexible polymer solar modules," *Solar Energy Materials and Solar Cells,* vol. 95, pp. 1398-1416, May 2011.

[87] H. Huang, *et al.*, "Nanostructural Characteristics and Mechanical Properties of Low Temperature Plasma Enhanced Chemical Vapor Deposited Silicon Nitride Thin Films," *Journal of Nanoscience and Nanotechnology,* vol. 9, pp. 3734-3741, Jun 2009.

[88] P. E. Burrows, *et al.*, "Reliability and Degradation of Organic Light-Emitting Devices," *Applied Physics Letters,* vol. 65, pp. 2922-2924, Dec 5 1994.

[89] Y. J. Liao, *et al.*, "Low-cost and reliable thin film encapsulation for organic light emitting diodes using magnesium fluoride and zinc sulfide," *Thin Solid Films,* vol. 519, pp. 2344-2348, Jan 31 2011.

[90] A. J. Medford, *et al.*, "Grid-connected polymer solar panels: initial considerations of cost, lifetime, and practicality," *Optics Express,* vol. 18, pp. A272-A285, Sep 13 2010.

[91] S. Park, *et al.*, "Improved lifetime of highly flexible OLEDs based on multilayered transparent electrodes with enhanced barrier performance," *Journal of the Society for Information Display,* vol. 19, pp. 597-601, 2011.

[92] K. Vasko, *et al.*, "Multilayer coatings for flexible high-barrier materials," *Central European Journal of Physics,* vol. 7, pp. 371-378, Jun 2009.

[93] T.-N. Chen, *et al.*, "High-Performance Transparent Barrier Films of SiO_x/SiN_x Stacks on Flexible Polymer Substrates," *J. Electrochem. Soc.,* vol. 150, 2006.

[94] S. M. George, "Atomic Layer Deposition: An Overview," *Chemical Reviews,* vol. 110, pp. 111-131, Jan 2010.

[95] W. Keuning, *et al.*, "Cathode encapsulation of organic light emitting diodes by atomic layer deposited Al2O3 films and Al2O3/a-SiNx:H stacks," *Journal of Vacuum Science & Technology A,* vol. 30, Jan 2012.

[96] P. F. Carcia, *et al.*, "Ca test of Al2O3 gas diffusion barriers grown by atomic layer deposition on polymers," *Applied Physics Letters,* vol. 89, p. 031915, 2006.

[97] P. F. Carcia, *et al.*, "Permeation measurements and modeling of highly defective Al2O3 thin films grown by atomic layer deposition on polymers," *Applied Physics Letters,* vol. 97, p. 3, Nov 2010.

[98] S. M. George, "Fabrication of Nanolaminates with Ultrathin Nanolayers Using Atomic Layer Deposition: Nucleation and Growth Issues," *Final Technical Report,* 2009.

[99] W. F. A. Besling, *et al.*, "Characterisation of ALCVD Al2O3-ZrO2 nanolaminates, link between electrical and structural properties," *Journal of Non-Crystalline Solids,* vol. 303, pp. 123-133, May 2002.

[100] J. W. Elam and S. M. George, "Growth of ZnO/Al2O3 alloy films using atomic layer deposition techniques," *Chemistry of Materials,* vol. 15, pp. 1020-1028, Feb 25 2003.

[101] J. W. Elam, *et al.*, "ZnO/Al2O3 nanolaminates fabricated by atomic layer deposition: growth and surface roughness measurements," *Thin Solid Films,* vol. 414, pp. 43-55, Jul 1 2002.

[102] S. X. Lao, *et al.*, "Plasma enhanced atomic layer deposition of HfO2 and ZrO2 high-k thin films," *Journal of Vacuum Science & Technology A,* vol. 23, pp. 488-496, May-Jun 2005.

[103] J. W. Pankow, *et al.*, "Moisture barrier," *U.S. Patent 025314,* 2011.

[104] Y. Leterrier, *et al.*, "Mechanical failure analysis of thin film transistor devices on steel and polyimide substrates for flexible display applications," *Engineering Fracture Mechanics,* vol. 77, pp. 660-670, Mar 2010.

[105] S. Grego, *et al.*, "Development and evaluation of bend-testing techniques for flexible-display applications," *Journal of the Society for Information Display,* vol. 13, pp. 575-581, Jul 2005.

[106] Y. Leterrier, *et al.*, "Models for saturation damage state and interfacial shear strengths in multilayer coatings," *Mechanics of Materials,* vol. 42, pp. 326-334, March 2010.

[107] Y. Leterrier, *et al.*, "Mechanical integrity of transparent conductive oxide films for flexible polymer-based displays," *Thin Solid Films,* vol. 460, pp. 156-166, Jul 22 2004.

[108] Y. Leterrier, *et al.*, "Adhesion of silicon oxide layers on poly(ethylene terephthalate) .1. Effect of substrate properties on coating's fragmentation process," *Journal of Polymer Science Part B-Polymer Physics,* vol. 35, pp. 1449-1461, Jul 15 1997.

[109] P. R. Elowe, *et al.*, "Development of Direct Cell Inorganic Barrier Film Technology Providing Exceptional Device Stability for CIGS Solar Cells," *Chemistry of Materials,* vol. 23, pp. 3915-3920, Sep 13 2011.

[110] G. K. Mor, *et al.*, "Use of highly-ordered TiO2 nanotube arrays in dye-sensitized solar cells," *Nano Letters,* vol. 6, pp. 215-218, 2006.

[111] B. A. Gregg, "Excitonic Solar Cells," *Journal of Physical Chemistry B,* vol. 107, pp. 4688-4698, 2003.

[112] S. Na, *et al.*, "Efficient and flexible ITO-free organic solar cells using highly conductive polymer anodes," *Advanced Materials,* vol. 20, pp. 4061-4067, 2008.

[113] S. Marsillac, *et al.*, "High Efficiency Solar Cells Based on Cu(InAl)Se2 Thin Films," *Applied Physics Letters,* vol. 81, p. 1350, 2002.

[114] J. Klaer, *et al.*, "Efficient CuInS2 thin-film solar cells prepared by a sequential process," *Semiconductor Science and Technology,* vol. 13, pp. 1456-1458, 1998.

[115] K. Siemer, *et al.*, "Efficient CuInS2 solar cells from a rapid thermal process (RTP)," *Solar Energy Materials and Solar Cells,* vol. 67, pp. 159-166, 2001.

[116] J. Scofield, *et al.*, "Sputtered Molybdenum Bilayer Back Contact for Copper Indium Diselenide-Based Polycrystalline Thin-Film Solar Cells," *Thin Solid Films,* vol. 260, pp. 26-31, 1995.

[117] X. Wu, "High-Efficiency polycrystalline CdTe thin-film solar cells," *Solar Energy,* vol. 77, pp. 803-814, 2004.

[118] F. Kessler, "Technological aspects of flexible CIGS solar cells and modules," *Solar Energy,* vol. 77, pp. 685-695, D. Rudmann.

[119] F. Kessler, *et al.*, "Approaches to Flexible CIGS Thin-Film Solar Cells," *Thin Solid Films,* vol. 480-481, pp. 491-498, 2005.

[120] S. Hau, *et al.*, "High performance ambient processed inverted polymer solar cells through interfacial modification with a fullerene self-assembled monolayer," *Applied Physics Letters,* vol. 93, p. 233304, 2008.

[121] J. Zou, *et al.*, "Metal grid/conducting polymer hybrid transparent electrode for inverted polymer solar cells," *Applied Physics Letters,* vol. 96, p. 203301, 2010.

[122] A. Kyaw, *et al.*, "An inverted organic solar cell employing a sol-gel derived ZnO electron selectrive layer and thermal evaporated MoO3 hole selective layer," *Applied Physics Letters,* 2008.

[123] L. Blankenburg, *et al.*, "Reel-to-reel wet coating as an efficient up-scaling technique for the production of bulk-heterojunction polymer solar cells," *Solar Energy Materials and Solar Cells,* vol. 93, pp. 476-483, 2009.

[124] F. C. Krebs, *et al.*, "A complete process for production of flexible large area polymer solar cells entirely using screen printing-First public demonstration," *Solar Energy Materials and Solar Cells,* vol. 93, pp. 422-441, 2009.

[125] W. Ma, *et al.*, "Thermally stable, efficient polymer solar cells with nanoscale control of the interpenetrating network morphology," *Advanced Functional Materials,* vol. 15, pp. 1617-1622, 2005.

[126] M. O. Reese, *et al.*, "Photoinduced Degradation of Polymer and Polymer-Fullerene Active Layers: Experiment and Theory," *Advanced Functional Materials,* vol. 20, pp. 3476-3483, Oct 22 2010.

[127] J. Kalowekamo and E. Baker, "Estimating the manufacturing cost of purely organic solar cells," *Solar Energy,* vol. 83, pp. 1224-1231, Aug 2009.

[128] E. Voroshazi, *et al.*, "Long-term operational lifetime and degradation analysis of P3HT: PCBM photovoltaic cells," *Solar Energy Materials and Solar Cells,* vol. 95, pp. 1303-1307, May 2011.

[129] M. Schmidt, *et al.*, "Adhesion and barrier performance of novel barrier adhesives used in multilayered high-barrier laminates," *Journal of Adhesion Science and Technology,* vol. 26, pp. 2405-2436, 2012.

[130] A. A. Griffith, "The phenomena of rupture and flow in solids," *Philosophical Transactions of the Royal Society of London. Series A,* vol. 221, pp. 163-198, 1921.

[131] G. R. Irwin, "Onset of Fast Crack Propagation in High Strength Steel and Aluminum Alloys," *Sagamore Research Conference Proceedings,* vol. 2, 1956.

[132] G. R. Irwin, *et al.*, "Discontinuous Crack Propagation - Further Studies," *Journal of Metals,* vol. 2, pp. 1035-1036, 1950.

[133] G. R. Irwin, "Analysis of Stresses and Strains near the End of a Crack Traversing a Plate," *Journal of Applied Mechanics-Transactions of the Asme,* vol. 24, pp. 361-364, 1957.

[134] M. L. Williams, "On the stress distribution at the base of a stationary crack," *Jornal of Appliced Mechanics,* vol. 25, pp. 109-114, 1957.

[135] N. C. Nguyen, *et al.*, "Reliability of PMMA bone cement fixation: fracture and fatigue crack-growth behaviour," *Journal of Materials Science-Materials in Medicine,* vol. 8, pp. 473-483, Aug 1997.

[136] G. R. Irwin, "Plastic Zone Near a Crack and Fracture Toughness," *Sagamore Research Conference Proceedings,* vol. 4, 1961.

[137] D. S. Dugdale, "Yielding of Steel Sheets Containing Slits," *Journal of the Mechanics and Physics of Solids,* vol. 8, pp. 100-104, 1960.

[138] M. Lane, "Interface fracture," *Annual Review of Materials Research,* vol. 33, pp. 29-54, 2003.

[139] Z. G. Suo and J. W. Hutchinson, "Sandwich Test Specimens for Measuring Interface Crack Toughness," *Materials Science and Engineering a-Structural Materials Properties Microstructure and Processing,* vol. 107, pp. 135-143, Jan 1989.

[140] K. M. Liechti and Y. S. Chai, "Biaxial Loading Experiments for Determining Interfacial Fracture-Toughness," *Journal of Applied Mechanics-Transactions of the Asme,* vol. 58, pp. 680-687, Sep 1991.

[141] J. M. Snodgrass*, et al.*, "Subcritical debonding of polymer/silica interfaces under monotonic and cyclic loading," *Acta Materialia,* vol. 50, pp. 2395-2411, May 24 2002.

[142] J. G. Swadener and K. M. Liechti, "Asymmetric shielding mechanisms in the mixed-mode fracture of a glass/epoxy interface," *Journal of Applied Mechanics-Transactions of the Asme,* vol. 65, pp. 25-29, Mar 1998.

[143] T. L. Anderson, *Fracture mechanics : fundamentals and applications*, 3rd ed. Boca Raton, FL: Taylor & Francis, 2005.

[144] R. Dauskardt*, et al.*, "Adhesion and debonding of multi-layer thin film structures," *Engineering Fracture Mechanics,* vol. 61, pp. 141-162, Aug 1998.

[145] M. L. Jokl*, et al.*, "A Microscopic Theory of Brittle-Fracture in Deformable Solids - a Relation between Ideal Work to Fracture and Plastic Work," *Acta Metallurgica,* vol. 28, pp. 1479-1488, 1980.

[146] A. G. Evans*, et al.*, "The Fracture Energy of Bimaterial Interfaces," *Metallurgical Transactions a-Physical Metallurgy and Materials Science,* vol. 21, pp. 2419-2429, Sep 1990.

[147] M. Lane*, et al.*, "Progressive debonding of multilayer interconnect structures," *Materials Reliability in Microelectronics Vii,* vol. 473, pp. 21-26, 1997.

[148] C. Shet and N. Chandra, "Analysis of energy balance when using cohesive zone models to simulate fracture processes," *Journal of Engineering Materials and Technology-Transactions of the Asme,* vol. 124, pp. 440-450, Oct 2002.

[149] H. Li and N. Chandra, "Analysis of crack growth and crack-tip plasticity in ductile materials using cohesive zone models," *International Journal of Plasticity,* vol. 19, pp. 849-882, 2003.

[150] S. A. Yerby*, et al.*, "The effect of a silane coupling agent on the bond strength of bone cement and cobalt-chrome alloy," *Journal of Biomedical Materials Research,* vol. 49, pp. 127-133, Jan 2000.

[151] K. L. Ohashi and R. H. Dauskardt, "Effects of fatigue loading and PMMA precoating on the adhesion and subcritical debonding of prosthetic-PMMA interfaces," *Journal of Biomedical Materials Research,* vol. 51, pp. 172-183, Aug 2000.

[152] K. L. Ohashi*, et al.*, "Effects of an adhesion promoter on the debond resistance of a metal-polymethylmethacrylate interface," *Journal of Biomedical Materials Research,* vol. 54, pp. 419-427, Mar 5 2001.

[153] S. Y. Kook*, et al.*, "Adhesion and reliability of polymer/inorganic interfaces," *Journal of Electronic Packaging,* vol. 120, pp. 328-335, Dec 1998.

[154] R. H.Dauskardt, "DTS Delaminator operation & maintenance manual by DTS company," 2011.

[155] J. F. Masson and M. A. Lacasse, "A review of adhesion mechanisms at the crack sealant/asphalt concrete interface," *Proceedings of the 3rd International Symposium on Durability of Building and Construction Sealants,* pp. 1-16.

[156] S. Wu, *Polymer interface and adhesion*. New York: M. Dekker in New York, 1982.

[157] B. M. Z. Newby and M. K. Chaudhury, "Friction in adhesion," *Langmuir,* vol. 14, pp. 4865-4872, Aug 18 1998.

[158] F. Kessler and D. Rudmann, "Technological aspects of flexible CIGS solar cells and modules," *Solar Energy,* vol. 77, pp. 685-695, 2004.

[159] J. William D. Callister, "Materials Science and Engineering: An Introduction, Seventh Edition," *John Wiley and Sons,* 2007.

[160] IUPAC, "van der Waals forces," *Compendium of Chemical Terminology,* 1994.

[161] S. S. VoyutskiiI and V. L. Vakula, "The role of diffusion phenomena in polymer-to-polymer adhesion," *Journal of Applied Polymer Science,* vol. 7, pp. 475-491, 1963.

[162] J. A. v. Farunhofer, "Adhesion and Cohesion," *International Journal of Dentistry,* vol. 2012, pp. 1-8, 2011.

[163] M. J. Borrego*, et al.*, "Effect of Silane Functional Group on Adhesion of Selected Epoxies for Microelectronic Packaging," *Journal of Microelectronics and Electronic Packaging,* vol. 5, pp. 8-15, 2007.

[164] J.-P. Griffiths, "Adhesion Promotion on Inorganic and Organic Substrates," *Adhesives & Sealants Industry,* pp. 1-2, 2010.

[165] P. H. Mutin*, et al.*, "Organic-inorganic hybrid materials based on organophosphorus coupling molecules: from metal phosphonates to surface modification of oxides," *Comptes Rendus Chimie,* vol. 6, pp. 1153-1164, Aug-Oct 2003.

[166] P. J. Hotchkiss, "The design, synthesis, and use of phosphonic acids for the surface modification of metal oxides," *Ph.D. Dissertation at Georgia Institute of Technology,* 2008.

[167] P. H. Mutin*, et al.*, "Hybrid materials from organophosphorus coupling molecules," *Journal of Materials Chemistry,* vol. 15, pp. 3761-3768, 2005.

[168] A. Sharma*, et al.*, "Stabilization of the work function of indium tin oxide using organic surface modifiers in organic light-emitting diodes," *Applied Physics Letters,* vol. 93, Oct 20 2008.

[169] P. J. Hotchkiss*, et al.*, "The Modification of Indium Tin Oxide with Phosphonic Acids: Mechanism of Binding, Tuning of Surface Properties, and Potential for Use in Organic Electronic Applications," *Accounts of Chemical Research,* vol. 45, pp. 337-346, Mar 2012.

[170] S. V. Aradhya*, et al.*, "Van der Waals interactions at metal/organic interfaces at the single-molecule level," *Nature Materials,* vol. 11, pp. 872-876, Oct 2012.

[171] S. A. Paniagua*, et al.*, "Phosphonic acid modification of indium-tin oxide electrodes: Combined XPS/UPS/contact angle studies," *Journal of Physical Chemistry C,* vol. 112, pp. 7809-7817, May 29 2008.

[172] K. S. Kim, *et al.*, "Investigation of crystallinity effects on the surface of oxygen plasma treated low density polyethylene using X-ray photoelectron spectroscopy," *Polymer,* vol. 44, pp. 6287-6295, Sep 2003.

[173] E. McCafferty and J. P. Wightman, "Determination of the concentration of surface hydroxyl groups on metal oxide films by a quantitative XPS method," *Surface and Interface Analysis,* vol. 26, pp. 549-564, Jul 1998.

[174] S. Y. Kim, *et al.*, "Effect of N(2), Ar, and O(2) plasma treatments on surface properties of metals," *Journal of Applied Physics,* vol. 103, Apr 1 2008.

[175] M. B. Chan-Park, *et al.*, "Surface characterization of nickel alloy plasma-treated by O-2/CF4 mixture," *Journal of Adhesion Science and Technology,* vol. 17, pp. 1979-2004, 2003.

[176] S. Kitova, *et al.*, "Soft plasma treatment of polymer surfaces," *Journal of Optoelectronics and Advanced Materials,* vol. 7, pp. 249-252, Feb 2005.

[177] J. H. Lee, *et al.*, "Effect of oxygen plasma treatment on adhesion improvement of Au deposited on Pa-c substrates," *Journal of the Korean Physical Society,* vol. 44, pp. 1177-1181, May 2004.

[178] A. Terriza, *et al.*, "Light Induced Hydrophilicity and Osteoblast Adhesion Promotion on Amorphous TiO_2," *Society for Biomaterials,* 2012.

[179] A. A. Volinsky, *et al.*, "Fracture toughness, adhesion and mechanical properties of low-K dielectric thin films measured by nanoindentation," *Thin Solid Films,* vol. 429, pp. 201-210, Apr 1 2003.

[180] L. Szutkowska, *et al.*, "Molecular dynamics of tert-butyl chloride confined to CPG (7.4, 15.6 nm)," *Acta Physica Polonica A,* vol. 108, pp. 357-370, Aug 2005.

[181] G. M. Pharr, "Measurement of mechanical properties by ultra-low load indentation," *Materials Science and Engineering a-Structural Materials Properties Microstructure and Processing,* vol. 253, pp. 151-159, Sep 30 1998.

[182] L. C. Lim and A. Muchtar, "Micro- and macro-indentation fracture toughness of alumina," *Journal of Materials Science Letters,* vol. 21, pp. 1145-1147, Aug 1 2002.

[183] X. D. Li and B. Bhushan, "A review of nanoindentation continuous stiffness measurement technique and its applications," *Materials Characterization,* vol. 48, pp. 11-36, Feb 2002.

[184] G. D. Quinn and R. C. Bradt, "On the Vickers indentation fracture toughness test," *Journal of the American Ceramic Society,* vol. 90, pp. 673-680, Mar 2007.

[185] D. Yang and T. Anderson, "Fracture Toughness of SiC Determined Using Nanoindentation," *Hysitron, Inc.,* pp. 1-2, 2010.

[186] M. D. Thouless and H. M. Jensen, "Elastic Fracture-Mechanics of the Peel-Test Geometry," *Journal of Adhesion,* vol. 38, pp. 185-197, 1992.

[187] O. Jorgensen*, et al.*, "A new procedure for measuring the decohesion energy for thin ductile films on substrates - Comments," *Journal of Materials Research,* vol. 11, pp. 2109-2111, Aug 1996.

[188] H. T. Zheng and S. K. Sitaraman, "Fixtureless superlayer-driven delamination test for nanoscale thin-film interfaces," *Thin Solid Films,* vol. 515, pp. 4709-4716, April 2007.

[189] S. Mahalingam*, et al.*, "Experimental characterization of monotonic and fatigue delamination of novel underfill materials," *Journal of Electronic Packaging,* vol. 128, pp. 405-411, Dec 2006.

[190] J. T. Zheng and S. K. Sitaraman, "In-process measurement of the interfacial fracture toughness for a sub-micron titanium thin film and silicon interface using a single-strip decohesion test," *54th Electronic Components & Technology Conference, Vols 1 and 2, Proceedings,* pp. 134-139, 2004.

[191] H. M. Jensen, "The Blister Test for Interface Toughness Measurement," *Engineering Fracture Mechanics,* vol. 40, pp. 475-486, 1991.

[192] H. M. Jensen and M. D. Thouless, "Effects of Residual-Stresses in the Blister Test," *International Journal of Solids and Structures,* vol. 30, pp. 779-795, 1993.

[193] Z. J. Cui*, et al.*, "A novel sample preparation method of four point bend adhesion test and its application on Cu and low k interfaces," *Advanced Metallization Conference 2004 (Amc 2004),* pp. 651-655, 2004.

[194] Q. Ma, "A four-point bending technique for studying subcritical crack growth in thin films and at interfaces," *Journal of Materials Research,* vol. 12, pp. 840-845, Mar 1997.

[195] P. G. Charalambides*, et al.*, "A test specimen for determining the fracture resistarim of bimaterial interfaces," *Journal of Applied Mechanics-Transactions of the Asme,* vol. 56, pp. 77-82, Mar 1989.

[196] M. D. Drory*, et al.*, "On the Decohesion of Residually Stressed Thin-Films," *Acta Metallurgica,* vol. 36, pp. 2019-2028, Aug 1988.

[197] M. D. Thouless*, et al.*, "The Edge Cracking and Spalling of Brittle Plates," *Acta Metallurgica,* vol. 35, pp. 1333-1341, Jun 1987.

[198] P. G. Charalambides*, et al.*, "Development of a Test Method for Measuring the Mixed-Mode Fracture-Resistance of Bimaterial Interfaces," *Mechanics of Materials,* vol. 8, pp. 269-283, Feb 1990.

[199] Z. Y. Huang*, et al.*, "Initiation and arrest of an interfacial crack in a four-point bend test," *Engineering Fracture Mechanics,* vol. 72, pp. 2584-2601, Nov 2005.

[200] H. C. Cao and A. G. Evans, "An Experimental-Study of the Fracture-Resistance of Bimaterial Interfaces," *Mechanics of Materials,* vol. 7, pp. 295-304, Jun 1989.

[201] G. D. Sim*, et al.*, "Moisture induced interface weakening in ACF package," *Materials Science and Engineering a-Structural Materials Properties Microstructure and Processing,* vol. 528, pp. 698-705, Dec 15 2010.

[202] S. Schmauder and M. Meyer, "Correlation between Dundurs Parameters and Elastic-Constants," *Zeitschrift Fur Metallkunde,* vol. 83, pp. 524-527, Jul 1992.

[203] M. F. Kanninen, "Augmented Double Cantilever Beam Model for Studying Crack-Propagation and Arrest," *International Journal of Fracture,* vol. 9, pp. 83-92, 1973.

[204] S. Y. Kook and R. H. Dauskardt, "Moisture-assisted subcritical debonding of a polymer/metal interface," *Journal of Applied Physics,* vol. 91, pp. 1293-1303, Feb 1 2002.

[205] R. Paetzold*, et al.*, "Permeation rate measurements by electrical analysis of calcium corrosion," *Review of Scientific Instruments,* vol. 74, pp. 5147-5150, Dec 2003.

[206] M. O. Reese, *et al.*, "Quantitative calcium resistivity based method for accurate and scalable water vapor transmission rate measurement," *Review of Scientific Instruments,* vol. 82, Aug 2011.

[207] G. Dennler, *et al.*, "Flexible, conjugated polymer-fullerene-based bulk-heterojunction solar cells: Basics, encapsulation, and integration," *Journal of Materials Research,* vol. 20, pp. 3224-3233, Dec 2005.

[208] M. T. Dang, *et al.*, "P3HT:PCBM, Best Seller in Polymer Photovoltaic Research," *Advanced Materials,* vol. 23, pp. 3597-3602, Aug 16 2011.

[209] Y. H. Zhou, *et al.*, "A universal method to produce low-work function electrodes for organic electronics," *Science,* vol. 336, pp. 327-332, Apr 20 2012.

[210] S. Lee, *et al.*, "Flexible organic solar cells composed of P3HT:PCBM using chemically doped graphene electrodes," *Nanotechnology,* vol. 23, Aug 31 2012.

[211] G. J. Zhao, *et al.*, "6.5% Efficiency of Polymer Solar Cells Based on poly(3-hexylthiophene) and Indene-C-60 Bisadduct by Device Optimization," *Advanced Materials,* vol. 22, pp. 4355-4358, Oct 15 2010.

[212] N. D. Treat, *et al.*, "In situ measurement of power conversion efficiency and molecular ordering during thermal annealing in P3HT:PCBM bulk heterojunction solar cells," *Journal of Materials Chemistry,* vol. 21, pp. 15224-15231, 2011.

[213] J. S. Kim, *et al.*, "Surface energy and polarity of treated indium-tin-oxide anodes for polymer light-emitting diodes studied by contact-angle measurements," *Journal of Applied Physics,* vol. 86, pp. 2774-2778, Sep 1 1999.

[214] J. F. Watts and J. Wolstenholme, "An Introduction to Surface Analyses by XPS and AES," John Wiley & Sons, Inc.: New York, 2003.

[215] R. A. Wind and S. M. George, "Quartz Crystal Microbalance Studies of Al2O3 Atomic Layer Deposition Using Trimethylaluminum and Water at 125 degrees C," *Journal of Physical Chemistry A,* vol. 114, pp. 1281-1289, Jan 28 2010.

[216] J. A. Yanez, *et al.*, "The adsorption of tri alkoxy silane on silicon nitride for colloidal processing," *Journal of the European Ceramic Society,* vol. 18, pp. 1493-1502, 1998.

[217] B. P. Cahill, *et al.*, "Reversible electrowetting on silanized silicon nitride," *Sensors and Actuators B-Chemical,* vol. 144, pp. 380-386, Feb 17 2010.

[218] R. J. Hohlfelder, *et al.*, "Adhesion of benzocyclobutene-passivated silicon in epoxy layered structures," *Journal of Materials Research,* vol. 16, pp. 243-255, Jan 2001.

[219] O. Prucker, *et al.*, "Photochemical attachment of polymer films to solid surfaces via monolayers of benzophenone derivatives," *Journal of the American Chemical Society,* vol. 121, pp. 8766-8770, Sep 29 1999.

[220] C. P. Tripp and M. L. Hair, "Chemical Attachment of Chlorosilanes to Silica - a 2-Step Amine-Promoted Reaction," *Journal of Physical Chemistry,* vol. 97, pp. 5693-5698, May 27 1993.

[221] H. S. Park and M. S. Gong, "Attachment of Humidity-Sensitive Membranes to Electrodes Surface via Photochemical Reaction of Benzophenone Derivatives," *Macromolecular Research,* vol. 18, pp. 596-601, Jun 2010.

[222] D. W. Choi, *et al.*, "A study of thin film encapsulation on polymer substrate using low temperature hybrid ZnO/Al2O3 layers atomic layer deposition," *Current Applied Physics,* vol. 12, pp. S19-S23, Sep 2012.

[223] M. T. Lloyd, *et al.*, "Enhanced Lifetime in Unencapsulated Organic Photovoltaics with Air Stable Electrodes," *35th Ieee Photovoltaic Specialists Conference,* 2010.

[224] H. Yan and H. Okuzaki, "Effect of solvent on PEDOT/PSS nanometer-scaled thin films: XPS and STEM/AFM studies," *Synthetic Metals,* vol. 159, pp. 2225-2228, Nov 2009.

[225] A. Orimo, *et al.*, "Surface segregation at the aluminum interface of poly(3-hexylthiophene)/fullerene solar cells," *Applied Physics Letters,* vol. 96, Jan 25 2010.

[226] K. Demirkan, *et al.*, "Reactivity and morphology of vapor-deposited Al/polymer interfaces for organic semiconductor devices," *Journal of Applied Physics,* vol. 103, Feb 1 2008.

[227] M. Lane, *et al.*, "Effects of interface nonplanarity on the interface fracture energy of the TiN/SiO2 system," *Thin Films Stresses and Mechanical Properties Vii,* vol. 505, pp. 357-362, 1998.

[228] J. S. Kim, *et al.*, "Indium-tin oxide treatments for single- and double-layer polymeric light-emitting diodes: The relation between the anode physical,

chemical, and morphological properties and the device performance," *Journal of Applied Physics,* vol. 84, pp. 6859-6870, Dec 15 1998.

[229] C. C. Wu*, et al.*, "Surface modification of indium tin oxide by plasma treatment: An effective method to improve the efficiency, brightness, and reliability of organic light emitting devices," *Applied Physics Letters,* vol. 70, pp. 1348-1350, Mar 17 1997.

[230] M. W. Lane*, et al.*, "Environmental effects on interfacial adhesion," *Microelectronics Reliability,* vol. 41, pp. 1615-1624, Sep-Oct 2001.

[231] E. P. Guyer and R. H. Dauskardt, "Fracture of nanoporous thin-film glasses," *Nature Materials,* vol. 3, pp. 53-57, Jan 2004.